

Photocopy and Use Authorization

In presenting this dissertation in partial fulfillment of the requirements for an advanced degree at Idaho State University, I agree that the Library shall make it freely available for inspection. I further state that permission for extensive copying of my dissertation for scholarly purposes may be granted by the Dean of the Graduate School, Dean of my academic division, or by the University Librarian. It is understood that any copying or publication of this dissertation for financial gain shall not be allowed without my written permission.

Signature _____

Date _____

Development of a Non-destructive Technique for the Restoration of Defaced Serial Numbers

by

Ikwulono David Unobe

A dissertation

submitted in partial fulfillment

of the requirements for the degree of

Doctor of Philosophy in Engineering and Applied Sciences

Idaho State University

Fall 2018

Committee Approval

To the Graduate Faculty:

The members of the committee appointed to examine the dissertation of IKWULONO DAVID UNOBE find it satisfactory and recommend that it be accepted.

Rene Rodriguez (Ph.D),

Major Advisor

John Kalivas (Ph.D),

Co-advisor

Andrew Sorensen (Ph.D),

Co-advisor

Lisa Goss (Ph.D),

Committee Member

Marco Schoen (Ph.D),

Graduate Faculty Representative

ACKNOWLEDGEMENTS

“He whose kernels have been cracked by benevolent spirits must never forget to be grateful.” It is with a deep sense of gratitude that I reflect on this journey I have undertaken. Many have helped and aided me along the way, and I owe them my immense appreciation.

I must express my deepest thanks to God almighty for limitless grace without which my efforts would have been in vain. I would also like to thank my research committee for the opportunity to work on this project and the dedication they have put into making it a success. I would like to express my sincerest gratitude to Prof. Rene Rodriguez for his endless support and guidance every step of the way. I would also like to express my gratitude to Prof. John Kalivas whose cheerful willingness to impart priceless knowledge helped me at every turn. My heartfelt thanks go to Dr. Andrew Sorensen for his selfless dedication to helping me in all facets of my academic journey. Special thanks also to Dr. Lisa Goss and Dr. Marco Schoen for agreeing to serve on my committee. I would like to thank my friends and colleagues; Lisa Lau who was of immense help with the experiment design and data collection as well as Ben Poulter, Matteo Gonzalez, and Anit Gurung all of whom have been instrumental to my getting this far. I would also like to appreciate the faculty and staff of the College of Science and Engineering for always lending a helping hand when I needed it. I would like to express my deepest gratitude to my family for their unalloyed support and unwavering belief in me through thick and thin.

The financial support of the National Institute of Justice through grant numbers 2013-R2-CX-K012 and 2015-R2-CX-0017 which have made this project possible is also greatly appreciated.

DEDICATION

To my family. You are the reason this little engine could.

TABLE OF CONTENTS

LIST OF TABLES	ix
LIST OF FIGURES	xi
ABSTRACT	xvii
CHAPTER 1	1
1.0. INTRODUCTION	1
1.1. MOTIVATION AND GOALS	7
1.2. DISSERTATION STRUCTURE	8
1.3. SPECIFIC AIMS	8
1.4. DISSERTATION CONTRIBUTIONS	11
1.5. EQUIPMENT USED	11
CHAPTER 2	14
2.0. LITERATURE REVIEW	14
2.1. BACKGROUND	14
2.2. INFRARED THERMAL IMAGING	22
2.2.1. Lock-In Infrared Thermography	27
2.3. MULTIVARIATE IMAGE ANALYSIS	34
2.3.1. Principal Component Analysis	34
2.4. FEATURE EXTRACTION	37
2.4.1. Zernike Moments	39
2.4.2. Pseudo Zernike Moments	43
2.5. SIMILARITY MEASURES	44
2.5.1. Data Fusion	45
2.6. CONFORMAL PREDICTION	46
CHAPTER 3	49
3.0. MATERIALS AND METHODS	49
3.1. SAMPLE ACQUISITION	49
3.1.1. Stainless Steel Plates	49
3.1.2. Gun Barrel	51
3.1.3. Laser Engraved Needle Holder	52
3.1.4. Motorcycle VIN	52
3.2. DATA AQUISITION	53
3.2.1. Surface Preparation	53

3.2.2.	Equipment Setup	54
3.2.3.	Lock-In Infrared Thermography	56
3.3.	MULTIVARIATE IMAGE ANALYSIS	57
3.3.1.	Principal Component Analysis	57
3.4.	NUMBER IDENTIFICATION	59
3.4.1.	Feature Extraction	60
3.4.2.	Similarity Measures	66
3.4.3.	Data Fusion	73
3.5.	CONFORMAL PREDICTION	75
3.5.1.	Nearest Neighbor Procedure	75
3.5.2.	Distance to Average Procedure	77
CHAPTER 4	79
4.0.	DATA COLLECTION AND IMAGE ANALYSIS	79
4.1.	FINITE ELEMENT MODELING	79
4.2.	STAINLESS STEEL PLATE WITH HOLES	81
4.3.	STAINLESS STEEL PLATE WITH NUMBERS	82
4.4.	GUN BARREL	96
4.5.	LASER ENGRAVED NEEDLE HOLDER	106
4.6.	MOTORCYCLE VIN	115
CHAPTER 5	125
5.0.	NUMBER IDENTIFICATION	125
5.1.	ZERNIKE MOMENTS	125
5.2.	PSEUDO ZERNIKE MOMENTS	134
5.3.	CONFORMAL PREDICTION	148
5.3.1.	Identification by Zernike Moments	148
5.3.2.	Identification by Pseudo Zernike Moments	154
CHAPTER 6	157
6.0.	CONCLUSION	157
6.1.	FUTURE WORK	158
REFERENCE	160
Appendix I: Score Images of Defaced Numbers	167
Appendix II: Equipment Used	171
Appendix III: Images of Reference Libraries used	173

Appendix IV: Study of variation in thermal gradient 174

LIST OF TABLES

Table 2.1: Chemical solutions used for chemical etching for different materials.	20
Table 3.1: Similarity measures used.	68
Table 3.2: Fusion rule notation for figures.	74
Table 4.1: Parameters used for simulated plot.....	83
Table 4.2: Percentage of Variance in each PC for defaced numbers on stainless steel sample (shaded boxes represent the PC where the respective numbers where best reproduced).	88
Table 4.3: Percentage of Variance in each PC at each modulation frequency tested for defaced number '1' on gun barrel sample (shaded boxes represent the PC where the respective numbers where best reproduced).	100
Table 4. 4: Percentage of Variance in each PC at each modulation frequency tested for defaced number '2' on gun barrel sample (shaded boxes represent the PC where the respective numbers where best reproduced).	105
Table 4.5: Percentage of Variance in each PC at each modulation frequency tested for defaced number '0' on gun barrel sample (shaded boxes represent the PC where the respective numbers where best reproduced).	110
Table 4.6: Percentage of Variance in each PC at each modulation frequency tested for defaced number '3' on laser engraved needle holder sample (shaded boxes represent the PC where the respective numbers where best reproduced).	114
Table 4.7: Percentage of Variance in each PC for defaced numbers on motorcycle (shaded boxes represent the PC where the respective numbers where best reproduced).	122
Table 5.1: Fonts used in the reference library images.	131
Table 5.2: Fusion of similarity measure values for area around defaced number six.	133
Table 5.3: Fusion of similarity measure values for area around defaced number two.	133
Table 5.4: Fusion of similarity measure values for area around defaced number five.	133
Table 5.5: Fusion of similarity measure values for area around defaced number zero.	133
Table 5.6: Fusion of similarity measure values for area around defaced number six.	139
Table 5.7: Fusion of similarity measure values for area around defaced number two.	139
Table 5.8: Fusion of similarity measure values for area around defaced number five.	139
Table 5.9: Fusion of similarity measure values for area around defaced number zero.	139
Table 5.10: Fusion of similarity measure values for area around defaced number one.	143

Table 5.11: Fusion of similarity measure values for area around defaced number two.	143
Table 5.12: Fusion of similarity measure values for area around defaced number zero.	146
Table 5.13: Fusion of similarity measure values for area around defaced number three.	146
Table 5.14: Fusion of similarity measure values for recovered numbers on motorcycle.	148
Table 5.15: Conformal prediction results using nearest neighbor algorithm for defaced number 6 on stainless steel sample.	149
Table 5.16: Conformal prediction results using nearest neighbor algorithm for defaced number 2 on stainless steel sample.	149
Table 5.17: Conformal prediction results using nearest neighbor algorithm for defaced number 5 on stainless steel sample.	150
Table 5.18: Conformal prediction results using nearest neighbor algorithm for defaced number 0 on stainless steel sample.	150
Table 5.19: Conformal prediction results using distance to average algorithm for defaced number 6 on stainless steel sample.	152
Table 5.20: Conformal prediction results using distance to average algorithm for defaced number 2 on stainless steel sample.	152
Table 5.21: Conformal prediction results using distance to average algorithm for defaced number 5 on stainless steel sample.	153
Table 5.22: Conformal prediction results using distance to average algorithm for defaced number 0 on stainless steel sample.	153
Table 5.23: Conformal Prediction Results for stainless steel sample.	154
Table 5.24: Conformal Prediction Results for the gun barrel sample.	155
Table 5.25: Conformal Prediction Results for the laser engraved needle holder.	155
Table 5.26: Conformal Prediction Results for the motorcycle VIN.	155

LIST OF FIGURES

Figure 2.1 Dislocation movement in a crystal	15
Figure 2.2: Diagrammatic representation of zone of plastic strain [3]	16
Figure 3.1: Stainless steel plate with holes drilled in.....	50
Figure 3.2: Stainless steel sample with stamped numbers.....	50
Figure 3.3: Stainless steel sample with numbers defaced (boxes show areas extracted and individually analyzed for each number).	51
Figure 3.4: Gun barrel with identification marks stamped in.	51
Figure 3.5: Picture of the gun barrel after defacing the 1 and 2 from the label "12 gauge" (The India ink coating has been partially removed from the defaced areas for ease of viewing).....	51
Figure 3.6: Laser engraved needle holder.....	52
Figure 3.7: Defaced and painted needle holder.	52
Figure 3.8: Yamaha motorcycle with defaced VIN.....	53
Figure 3.9: a) Defaced VIN on motorcycle fork, and b) VIN on motorcycle engine with most numbers still intact.....	53
Figure 3.10: Experimental setup.....	55
Figure 3.11: Schematic of unfolding the phase images for PCA.....	58
Figure 3.12: Flowchart showing procedure for identification of recovered numbers.	60
Figure 3.13: Digital images created to use in identifying recovered numbers.	66
Figure 4.1: Meshed FE model with stamped number.....	80
Figure 4.2: Plastic strain distribution on surface of FE model.	80
Figure 4.3: Plastic strain distribution on surface after removing material.....	80
Figure 4.4: Plastic strain distribution after applying thermal energy to surface.....	81
Figure 4.5: Raw thermal image of stainless steel plate with holes drilled in (axes represent the pixel coordinates and the color bar shows the temperature range (°C) of the sample).....	81
Figure 4.6: Phase image of drilled sample (axes represent the pixel coordinates and the color bar shows the degree of phase shift).	82
Figure 4.7: Score Image of drilled sample after PCA (Axes represent the pixel coordinates and the color bar shows the range of score values).	82
Figure 4.8: Stainless steel sample with numbers defaced (boxes show areas extracted and individually analyzed for each number).	83

Figure 4.9: Phase difference plots for each defaced number on stainless steel sample.....	84
Figure 4.10: Mean temperature-time plot across the defaced 6 surface.	85
Figure 4.11: Raw thermal image of a clean surface (axes represent the pixel coordinates and the color bar shows the temperature range (°C) of the sample).....	85
Figure 4.12: Raw thermal images of areas around defaced numbers a) Six b) Two c) Five d) Zero (axes represent the pixel coordinates and color bars show the temperature range (°C) of the sample).....	86
Figure 4. 13: Phase image of a clean surface (axes represent the pixel coordinates and the color bar shows the degree of phase shift).	87
Figure 4. 14: Phase images of areas around defaced numbers a) Six b) Two c) Five d) Zero (axes represent the pixel coordinates and the color bar shows the degree of phase shift).	87
Figure 4.15: Score images for clean surface (Axes represent the pixel coordinates and the color bar shows the range of score values).	90
Figure 4.16: Score images for area around defaced number six (Axes represent the pixel coordinates and the color bar shows the range of score values).	91
Figure 4.17: Score images showing recovered numbers a) Two b) Five c) Zero (Axes represent the pixel coordinates and the color bar shows the range of score values).	93
Figure 4.18: Score images with markers for a) six, b) two, c) five, and d) zero.	94
Figure 4.19: Plots of the phase values across experimentation cycles for areas around defaced numbers a) Six b) Two c) Five and d) Zero.....	94
Figure 4.20: Plots of the filtered phase values across experimental cycles for areas around defaced numbers a) Six b) Two c) Five and d) Zero	95
Figure 4.21: Picture of the gun barrel after defacing the 1 and 2.	96
Figure 4.22: Raw thermal images of area around defaced number ‘1’ at modulation frequencies a) 1 Hz, b) 0.125 Hz, c) 0.05 Hz, and d) 0.03125 Hz.	97
Figure 4.23: Phase images of area around defaced number ‘1’ at modulation frequencies a) 1 Hz, b) 0.125 Hz, c) 0.05 Hz, and d) 0.03125 Hz.	98
Figure 4.24: Filtered phase images of area around defaced number ‘1’ at modulation frequencies a) 1 Hz, b) 0.125 Hz, c) 0.05 Hz, and d) 0.03125 Hz.	99
Figure 4.25: Score Images of a) Clean 1 before defacing, and after defacing at b) 1Hz, c) 0.125Hz, d) 0.05Hz, and e) 0.03125Hz.	101
Figure 4.26: Raw thermal images of area around defaced number ‘2’ at modulation frequencies a) 1 Hz, b) 0.125 Hz, c) 0.05 Hz, and d) 0.03125 Hz.	102
Figure 4. 27: Phase images of area around defaced number ‘2’ at modulation frequencies a) 1 Hz, b) 0.125, Hz c) 0.05 Hz, and d) 0.03125 Hz.	103

Figure 4.28: Filtered phase images of area around defaced number ‘2’ at modulation frequencies a) 1 Hz, b) 0.125 Hz, c) 0.05 Hz, and d) 0.03125 Hz.	104
Figure 4.29: Score Images of a) Clean 2 before defacing, and after defacing at b) 1Hz, c) 0.125Hz, d) 0.05Hz, and e) 0.03125Hz.	106
Figure 4.30: Aesculap needle holder with a) Laser engraved numbers and b) numbers defaced and painted with India ink.....	106
Figure 4.31: Raw thermal images of area around defaced number ‘0’ at modulation frequencies a) 1 Hz, b) 0.125 Hz, c) 0.05 Hz, and d) 0.03125 Hz.	107
Figure 4.32: Phase images of area around defaced number ‘0’ at modulation frequencies a) 1 Hz, b) 0.125 Hz, c) 0.05 Hz, and d) 0.03125 Hz.	108
Figure 4.33: Filtered phase images of area around defaced number ‘0’ at modulation frequencies a) 1 Hz, b) 0.125 Hz, c) 0.05 Hz, and d) 0.03125 Hz.	109
Figure 4.34: Score Images of defaced area around 0 at a) 1Hz, b) 0.125Hz, c) 0.05Hz, and d) 0.03125Hz.	111
Figure 4.35: Raw thermal images of area around defaced number ‘3’ at modulation frequencies a) 1 Hz, b) 0.125 Hz, c) 0.05 Hz, and d) 0.03125 Hz.	111
Figure 4.36: Phase images of area around defaced number ‘3’ at modulation frequencies a) 1 Hz, b) 0.125 Hz, c) 0.05 Hz, and d) 0.03125 Hz.	112
Figure 4.37: Filtered phase images of area around defaced number ‘3’ at modulation frequencies a) 1 Hz, b) 0.125 Hz, c) 0.05 Hz, and d) 0.03125 Hz.	113
Figure 4.38: Score Images of defaced area around number 3 at a) 1Hz, b) 0.125Hz, c) 0.05Hz, and d) 0.03125Hz.....	115
Figure 4.39: Defaced motorcycle fork painted with India ink (white lines show the sections of the area individually imaged and analyzed).	116
Figure 4.40: Score Image of a section of defaced area showing some partially defaced numbers.	117
Figure 4.41: Score Image of a section of defaced area showing a possible number (in white box) and other localized areas (in red boxes).....	117
Figure 4.42: Score Image of a section of defaced area showing a possible number (in white box) and other localized areas (in red boxes).....	118
Figure 4.43: Raw thermal images of area around defaced numbers a) five, b) two, c) five, d) one, e) unknown, f) zero, g) unknown h) four i) one.....	119
Figure 4.44: Phase images of area around defaced numbers a) five, b) two, c) five, d) one, e) unknown f) zero g) unknown h) four, and i) one.	120
Figure 4.45: Filtered phase images of area around defaced numbers a) five, b) two, c) five, d) one, e) unknown f) zero, g) unknown, h) four and i) one.	121

Figure 4.46: Score images showing the recovered VIN numbers a) 5 (0.03125Hz), b) 2 (0.03125Hz), c) 5 (0.03125Hz), d) 1 (0.05Hz), e) unknown (0.05Hz), f) 0 (0.05Hz), g) unknown (0.05Hz), h) 4 (0.05Hz), and i) 1 (0.05Hz).....	123
Figure 5.1: Cumulative mean square error difference for an increasing order of Zernike polynomials shown for two reference library numbers and a recovered number as examples. See text for description of insets.....	126
Figure 5.2: Cumulative mean square error difference for an increasing order of Zernike polynomials shown for four recovered numbers.	127
Figure 5.3: Images of a) original score image, and reconstructed images at Zernike moment orders b) 20, c) 45, d) 50.....	128
Figure 5.4: Similarity merits for all score images of recovered numbers a) six, b) two, c) five, and d) zero.....	130
Figure 5.5: Results of fusion ranking for recovered numbers a) six, b) two, c) five, and d) zero.	131
Figure 5.6: Image of fused merits from all fusion rules for the recovered numbers a) six, b) two, c) five, d) zero.	132
Figure 5.7: Cumulative mean square error difference for an increasing order of pseudo Zernike polynomials shown for two reference library images and recovered number '2'.	134
Figure 5.8: Cumulative mean square error difference for an increasing order of pseudo Zernike polynomials shown for four recovered numbers.	135
Figure 5.9: Similarity merits for all score images of recovered numbers a) six, b) two, c) five, and d) zero.....	137
Figure 5.10: Results of fusion ranking for recovered numbers a) six, b) two, c) five, and d) zero.	138
Figure 5.11: Image of fused merits from all fusion rules for the recovered numbers a) six, b) two, c) five, d) zero.	140
Figure 5.12: Similarity merits for all score images of defaced number '1' using modulation frequency a) 1 Hz, b) 0.125 Hz, c) 0.05 Hz, and d) 0.03125 Hz.	141
Figure 5.13: Similarity merits for all score images of defaced number '2' using modulation frequency a) 1 Hz, b) 0.125 Hz, c) 0.05 Hz, and d) 0.03125 Hz.	142
Figure 5.14: Image of fused merits from all fusion rules for the defaced numbers a) one, and b) two.....	143
Figure 5.15: Similarity merits for all score images of defaced number '0' using modulation frequency a) 1 Hz, b) 0.125 Hz, c) 0.05 Hz, and d) 0.03125 Hz.	144

Figure 5.16: Similarity merits for all score images of defaced number ‘3’ using modulation frequency a) 1 Hz, b) 0.125 Hz, c) 0.05 Hz, and d) 0.03125 Hz.	145
Figure 5.17: Image of fused merits from all fusion rules for the defaced numbers a) zero, and b) three.....	146
Figure 5.18: Similarity merits for all score images of recovered number a) five, b) two, c) five, d) one, e) unknown (presumed to be a 0), f) zero, g) unknown (presumed to be a 7), h) four, and i) one.....	147
Figure A1: Refolded PC score images of the area around the defaced number 2 with PC 11 showing the best representation of the number.....	168
Figure A2: Refolded PC score images of the area around the defaced number 5 with PC 10 showing the best representation of the number.....	169
Figure A3: Refolded PC score images of the area around the defaced number 0 with PC 1 showing the best representation of the number.....	170
Figure A4: FLIR SC6700 infrared camera with sample on a hot plate under observation.	171
Figure A5: Oscilloscope.	171
Figure A6: Uniblitz mechanical shutter.....	172
Figure A7: Mechanical shutter control box (top) and Stanford Research Systems function generator (bottom).	172
Figure A8: Images of digits used from different fonts.	173
Figure A9: Score image reproducing defaced 6 with selected pixels marked.....	175
Figure A10: Plot of difference in standard deviation between defaced areas and clean areas across 15 amplitude images.	175
Figure A11: Score images reproducing defaced numbers using a) all amplitude images, b) amplitude image with lowest standard deviation removed and c) amplitude images with 5 lowest standard deviations removed.....	176
Figure A12: Score image reproducing defaced 2 with selected pixels marked.....	176
Figure A13: Plot of difference in standard deviation between defaced areas and clean areas across 15 amplitude images.	177
Figure A14: Score images reproducing defaced numbers using a) all amplitude images, b) amplitude image with lowest standard deviation removed and c) amplitude images with 5 lowest standard deviations removed.....	178
Figure A15: Score image reproducing defaced 5 with selected pixels marked.....	178
Figure A16: Plot of difference in standard deviation between defaced areas and clean areas across 15 phase images.	179

Figure A17: Score images reproducing defaced numbers using a) all phase images, b) phase image with lowest standard deviation removed and c) phase images with 5 lowest standard deviations removed. 180

Figure A18: Score image reproducing defaced 0 with selected pixels marked. 180

Figure A19: Plot of difference in standard deviation between defaced areas and clean areas across 15 amplitude images. 181

Figure A20: Figure 6: Score images reproducing defaced numbers using a) all amplitude images, b) amplitude image with lowest standard deviation removed and c) amplitude images with 5 lowest standard deviations removed. 182

Development of a Non-destructive Technique for the Restoration of Defaced Serial Numbers

Dissertation Abstract – Idaho State University (2018)

Infrared thermal imaging is an evolving approach useful in nondestructive evaluation of materials for industrial and research purposes. This study investigates the use of this method in combination with multivariate data analysis as an alternative to chemical etching; a destructive method currently used to recover defaced serial numbers stamped in metal. This process involves several unique aspects, each of which works to overcome some pertinent challenges associated with the recovery of defaced serial numbers. Infrared thermal imaging of metal surfaces provides thermal images sensitive to local differences in thermal conductivity of regions of plastic strain created from stamping pressures in mechanically stamped pieces and a heat affected zone in laser engraved samples, both extending to depths below the visible characters. These are exposed to the surface when the serial numbers are removed. These thermal differences are quite small and thus not readily visible from the raw thermal images of an irregular surface created by removing the stamped numbers. As such, further enhancement is usually needed to identify the subtle variations. The multivariate data analysis method, principal component analysis, is used to enhance these subtle variations and aid the recovery of the serial numbers. Multiple similarity measures are utilized to match recovered numbers to several numerical libraries, followed by application of various fusion rules to achieve consensus identification. Confidence indices are applied to the identification results by conformal prediction as a measure of the accuracy of the identification.

Key Words: Serial number restoration, Lock-in infrared thermography, Principal component analysis, Zernike moments, Pseudo Zernike moments, Similarity measure, Conformal Prediction

CHAPTER 1

1.0. INTRODUCTION

Stamp marks provide a means of unique identification for a range of items notably firearms and automobiles. However, these are regularly erased for criminal activities [1]. The Bureau of Alcohol, Tobacco and Firearms (ATF), estimates that between 9 and 20% of the firearms recovered as criminal evidence have had their serial numbers shaved off [2]. Serial numbers are applied in a variety of ways including mechanical stamping (die stamping, pin marking and roll marking), and laser beam engraving [3]. Stamped serial numbers are made by using a die designed to imprint numbers and letters to apply sufficient pressure to impart a permanent impression of the die symbol into the metal. The stamping of a serial number onto metals causes a permanent change in shape (plastic deformation) primarily due to the inability of regions of crystalline arrangement within localized grains to resist the induced stress of stamping. This leads to an alteration of the local crystalline structure and in extension the interlocking grain boundaries. The resulting deformation extends to some depth below the stamped mark and is known as the zone of plastic strain [4]. The depth of this zone is dependent on several factors including metal type, size and shape of the stamp and the force used to produce the marking. Due to the stress induced alterations in its microstructure, the zone of plastic strain has physical and chemical properties differing from those of the original metal [4,5]. These include changes in its hardness, electrical resistivity, ductility, yield stress, magnetic properties, thermal conductivity, electronic work function and chemical potential. Each of these property changes forms the basis for different serial number recovery methods [3].

Different serial number recovery techniques rely on these changes to reveal the hitherto invisible zone of plastic strain. Chemical etching, currently the most popular and widely used technique for recovering defaced serial numbers on firearms and automobiles, utilizes the change in

chemical potential, a measure of the metal's tendency to lose electrons (oxidize) under certain standardized conditions in the cold worked (deformed) area [6–11]. The local change in crystalline structure raises the metal's position in the electromotive series, thus lowering its resistance to oxidation. This change in the reduction potential makes the area more reactive to acids, creating a visible contrast between defaced and clean regions of the surface.

The method involves a highly controlled and destructive recovery process. It usually requires the etchant to be placed carefully on the surface of the metal, removed at intervals and then replenished often in several cycles. Control is especially important as the recovered marks are often very faint and appear and disappear during the etching. This varied and destructive nature of the chemical etching process and the fleeting nature of the recovered marks are reasons for concern in the use of this method for serial number recovery. Another concern is the recovery of laser engraved serial numbers which are increasingly being used in firearms and automobile marking. The laser process unlike stamping removes the metal by vaporizing the metal using the intense heat generated by a focused laser beam. This leaves no cold worked or plastic strain region although there will be change in the hardness of the surface below the heated region. As such, the lack of change in the reduction potential will reduce the effectiveness of the chemical etching recovery technique. Other destructive techniques currently in use to varying degrees of effectiveness include heat treatment, ultrasonic cavitation and electrolytic etching [3,12]. All of these techniques find a commonality in their non-repeatability due to being destructive. They have also proven to generally be less effective than chemical etching.

An alternative to chemical etching that could viably overcome the stated shortcomings is via nondestructive testing. Nondestructive evaluation involves the examination of the properties and integrity of an object without making any permanent changes to it [13]. Employed in a wide

range of fields including aviation, medicine, civil structures, transportation and manufacturing, it is a highly valuable technique to carry out inspections/examinations that would otherwise have proven destructive.

A nondestructive technique that has been tested for use in serial number restoration is magnetic particle inspection. However this technique has some limitations including reduced sensitivity for older stamp marks and being only applicable to magnetic metals, and mechanically stamped serial numbers [3,12].

A non-destructive technique which has proven useful in the detection of subsurface defects in metals and could be used in recovering defaced serial numbers is infrared thermography. This method seeks to locate and characterize flaws by measuring their effect on heat flow through the material under controlled conditions by observation of the propagation of applied thermal energy [14,15]. The process involves applying thermal energy to a material surface to raise its temperature substantially to a non-destructive point. As the thermal energy propagates through the object, infrared images are collected over the time of propagation to capture thermal gradient differences across the surface. These differences will occur within regions of plastic strain due to the local change in thermal conductivity. An infrared camera is used to collect the infrared images that capture the temperature distribution of the surface of interest and study this phenomenon.

Infrared thermography is classified into two main categories based on the method of sample excitation. These methods are passive and active thermography. In passive thermography, the sample is not excited by external thermal energy but the natural radiation from its surface is captured and studied. In the active thermography, the sample is excited by an external thermal energy source to induce noticeable thermal contrasts between defective areas and non-defective

areas. Several modes of active infrared thermography techniques have been tested and put into use for defect detection including pulse phase thermography, lock-in thermography and transient infrared thermography [14,15,24–26,16–23].

It is frequently difficult to identify the difference in temperature gradient from the infrared images. The changes can be very small and captured images could contain unwanted signals including reflections from the environment, surface emissivity variations, non-uniform heating and radiation off the object surface. All of these unwanted signals could lead to reduced visibility of the thermal gradient change across the surface. Lock-in thermography, a method that requires the extraction of the amplitude and phase of a captured signal, has proven to be particularly adept at overcoming some of these challenges such as reflections, emissivity variations and surface radiation. Lock-in thermography (LIT) as described in [21–24] involves inducing sinusoidal energy waves into the surface of a sample at a lock-in frequency, and collecting the infrared thermal images of the sample surface over the entire period of the pulsed wave. Digitally processed according to the lock-in principle, the thermographic image sequence is analyzed and compressed into an amplitude image, and a signal phase image. The developed images have some surface features suppressed making it more robust than regular thermal images for analyzing subsurface features [21–25].

A possible pitfall of using LIT for serial number recovery is the sensitivity of the imaging apparatus to visibly capture what might be infinitesimal changes in temperature gradient across the surface. Another is the capture of other features (such as possible material inhomogeneities) within the thermal depth range besides from the defects [22]. A conceivable way to overcome these challenges is using multivariate image analysis (MIA), a computational process that allows for the examination of collected images to help with detection and analysis of possible variations

within the data. Several MIA techniques have been tested for infrared thermography to reduce noise and isolate the thermal signature of defects including Absolute Thermal Contrast, Differentiated Absolute Contrast, Thermographic Signal Reconstruction and Principal Component Analysis [26,27].

Successfully applied in diverse fields [28,29,38,30–37], principal component analysis (PCA) is a very popular form of MIA. It is a technique used for identifying patterns in data and expressing them in a way that highlights the importance of elements within the data. Relying on the basic assumption of intercorrelation existing within the data, PCA works to develop a new set of uncorrelated and orthogonal descriptors (principal components) to explain a decreasing percentage of variance as more descriptors are included [36]. Effective for identifying patterns in data of high dimensions, Principal Component Analysis (PCA) has proved to be a useful tool in enhancing the contrast in thermographic images [29] by making it possible to isolate the thermal gradient information from the other contrasting signals within the captured infrared images. When used for images, the resulting principal components can be formed into score images, that are of the same spatial dimensions as the original images and provides a visual representation of the information retained in respective principal components. As such, using this method, it is conceivable that the unique thermal gradient of the zone of plastic strain across the phase images will be identified and clustered in a single score image or a subset of score images to possibly reproduce the defaced number.

Furthermore, after developing score images that enhance the visibility of the zone of plastic strain, it is imperative to conclusively identify the number without bias via an automated process. This identification can be achieved by comparing the developed score images to a reference library of unaltered digits to determine the best match using similarity measures, which are

computational methods of quantifying the similarity between objects [39–43]. The smaller the resulting output from the comparison, the closer the corresponding objects within the characteristics captured by the similarity measure. Several similarity measures are used in comparing the developed score images to the reference library, to give a holistic and unbiased comparison. It is possible that each measure used could in principle give differing results with respect to the characteristics captured within them. As such, it is pertinent to combine these individual measures in a way that will establish an objective consensus as to the result of the comparison. Data fusion, a technique used in combining individual sources of information into a single informative output with improved reliability and less ambiguity [39,40,49,50,41–48], is used to achieve this consensus. A high level or decision level fusion approach is used in this study as it involves the fusion of several parameters (similarity merits), each of which can be used to make an independent identification to yield a final inference.

Such comparisons come with a number of challenges including possible differences in size, translation, scale or rotation between the images being compared. These challenges can be overcome by comparing image features extracted via orthogonal moments, in lieu of the actual images. For this study, Zernike moments and pseudo Zernike moments are used to characterize the score images into feature vectors of a predetermined size. Both invariant to rotation, these moments have been proven to outperform other orthogonal moments including general orthogonal moments, Legendre moments and Jacobi Fourier moments as global shape descriptors for object classification and retrieval [51,52,61–65,53–60].

It is also necessary to assign a confidence index to the identification process. This will allow for an ‘easy to understand’ measure of accuracy of the identification made by the similarity measures without investigating each output value individually. A method that is gaining traction

in research fields concerned with the accuracy of the classification of unknown patterns is used in this study. This method, conformal prediction, utilizes the output values from the identification protocol to determine a confidence level for the identification of the particular defaced number [66–70].

This study aims to utilize the methods outlined to reproduce and identify in a non-destructive process, serial numbers on metallic items that have been defaced.

1.1. MOTIVATION AND GOALS

The goals of this study are motivated by the need in forensics for a non-destructive technique for the restoration of defaced serial numbers. Chemical etching, the recovery method currently widely used, is destructive and limited by its irreproducibility.

The overall goal of this project is to develop a holistic technique to restore in a non-destructive and wholly reproducible manner, defaced serial numbers. This is made possible by advances in high speed digital thermal imaging and advanced image analysis techniques. Three goals were identified as important to the completion of this study. These are:

1. To determine a thermal imaging technique best suited for capturing the thermal conductivity differences across the surface of a metal with zones of plastic strain or heat affected zones.
2. To develop image analysis procedures that will enhance these differences and help effect the recovery of stamped serial numbers.
3. To develop an identification protocol that will conclusively identify the numbers using the enhanced images independent of human bias leading to a holistic non-destructive, quick and cost effective method of restoring defaced serial numbers on metal objects.

1.2. DISSERTATION STRUCTURE

This thesis is organized as follows: Chapter 2 outlines a review of relevant literature and background information on the identified goals and associated hypotheses of the research carried out. Chapter 3 describes the research design and methods used in testing the hypothesis for nondestructive recovery of defaced number via infrared thermal imaging and multivariate imaging. Chapter 4 presents the results for the data collection and image analysis used to capture and enhance the thermal signature indicative of the deformed crystalline structure in the zone of plastic strain and heat affected zones. Chapter 5 details results from the identification of the defaced number from score images including a statistical method of attaching confidence levels to the recovered and identified numbers. Chapter 6 outlines the conclusions drawn from the results obtained and suggests future work that could be done to advance the field.

1.3. SPECIFIC AIMS

A methodology for this project was developed around three specific aims identified as being essential to the successful execution of the stated objectives. The specific aims and associated hypotheses are detailed below.

Aim 1: To determine a thermal imaging technique best suited for revealing the thermal conductivity differences across the surface of a metal with cold worked or heat affected zones.

This aim proposed to design and validate a thermal imaging protocol that will adequately capture the thermal conductivity differences across the metal surface due to distortion in the atomic crystalline structure within the defaced regions.

Lock-in infrared thermography (LIT) is utilized to achieve this aim. This technique has shown success in previous work in the detection of subsurface defects in metals and composites [16–

25]. From Fourier's law of conductivity [15], it is understood that a local change in a material property such as thermal conductivity due to distortions in the atomic structure from the force of stamping will result in a local change in the thermal gradient. This change may not be visible in raw thermal images due in part to existential environmental and sample surface conditions as well as possible instrumental noise and will be better defined in amplitude and phase images developed using lock-in analysis, to enhance low level signals hidden deep within the data.

Aim 2: To develop image analysis procedures to analyze the collected thermal images to enhance the thermal signature within the areas exposed by the defacing of the numbers.

Although less noisy and better detailed than the raw thermal images, amplitude and phase images may not be effective enough to clearly reveal enough of the surface temperature changes to identify the numbers removed. As such, some data processing is required to better enhance the images collected to identify the numbers therein. The proposed image analysis procedure tested for use in isolating and enhancing the local changes in thermal gradient is principal component analysis (PCA).

A strength of PCA lies in its ability to identify unique relationships in a dataset, orthogonal to all other relationships and similar across images in the dataset, and project these into a single principal component score/score image. The characteristics of pixels associated with areas of the sample within the regions of plastic strain in the amplitude or phase images should be similar across all the amplitude or phase images developed and uniquely differ from all other pixels within the images. As such, PCA should identify this and capture this region uniquely in a particular score image or a small subset of score images.

Aim 3: To develop a verification process to identify the defaced number within the score images independent of human bias.

It is imperative that the identification of the numbers within the score images developed by PCA be not only by visual inspection as this can be subject to biases. As such, some pattern recognition and statistical methods to identify these numbers, eliminating possible human biases is necessary. A combination of feature extraction methods and similarity measures is proposed for this purpose.

Image moments in general are used in pattern recognition as shape descriptors. Zernike moments and pseudo Zernike moments are particularly robust as shape descriptors because they are both rotation invariant, and allow a normalization procedure to make them scale and translation invariant. Because it is quite difficult to determine exactly the size and rotation of the numbers defaced, these properties will be useful in comparing the score images of recovered numbers to a reference library of unaltered digit images, to identify them.

This identification can be carried out by using similarity measures to identify similarities in magnitude, shape and direction between the score images and reference library images. Using several such measures to compare the shape descriptors of both sets of images, it should be possible to accurately identify the numbers, matching them to their equivalent within the library.

This study aims to develop a holistic methodology from a combination of both experimentation procedures and image analysis to recover and accurately identify serial numbers defaced from metal surfaces. A final step of applying a confidence index to the identification results to give an easy to understand measure of the accuracy of the results is also investigated.

1.4. DISSERTATION CONTRIBUTIONS

This thesis aims at developing a durable and robust non-destructive method for serial number restoration by utilizing infrared thermal imaging and advanced image analysis techniques to capture existing molecular structural deformations. The deformations occurred during application of the serial numbers and these deformations will be used to restore the defaced numbers.

A two stage method is presented in this thesis. The first stage, the thermal imaging and image analysis stage involves employing lock-in thermography and principal component analysis to develop score images that capture the difference in thermal gradient characteristic of areas beneath serial numbers. The second stage, the number identification stage involves the identification of the defaced numbers within the developed score images by extracting invariant feature vectors and comparing these to a reference number library. This approach has the advantages of being non-destructive as well as allowing for the identification of the defaced numbers independent of human bias.

1.5. EQUIPMENT USED

- **Infrared Camera:**

A FLIR 6700S Infrared camera is used for the experiments performed in this study. The specifications for the camera are shown in Table 1.1.

Table 1. 1: Specifications for the infrared camera

Detector Type	FLIR Indium Antimonide (InSb)
Spectral Range	1.0 – 5.0 μ m
Resolution	640 \times 512
Thermal Sensitivity	\sim 0.02 $^{\circ}$ C
Operating Temperature	-40 $^{\circ}$ C to 50 $^{\circ}$ C (-40 $^{\circ}$ F to 122 $^{\circ}$ F)

- **Function Generator:**

A Stanford Research Systems model DS340 15MHz function generator is used for the experiments. The function generator is used to generate sinusoidal frequencies ranging from 0.015 Hz to 1 Hz with corresponding time periods of 64s to 1s. An image of the function generator can be found in the Appendix.

- **Lock-in Modulation Circuit**

A custom lock-in modulation circuit built at Idaho State University is used to synchronize the laser pulsing frequencies with the camera, to ensure a consistent rate of frame capture over each pulsing cycle. This allows for a variable number of pulses to be sent to the camera for each pulse of the laser, with images taken by the camera at intervals set on the circuit. The circuit includes a start switch which allowed for the camera pulses to be synchronized with the pulsing of the laser.

- **Shutter**

A Uniblitz mechanical shutter was used to pulse the laser energy to the sample under study. It was synchronized to the sinusoidal modulation frequency generated by the function generator.

- **Laser**

A 5W Ar-ion cw laser, from Coherent inc., was used as the primary thermal excitation source for all samples tested. The laser was operated in all-lines mode to maximize the amount of power reaching the sample. The laser was generally set to produce 3W of thermal energy, allowing approximately 1.5W of thermal energy to reach the sample after going through the prisms used to direct the beam and the top hat filter which converted the Gaussian profile of the beam to a square profile.

- **Computation System and Software**

A Dell computer with 4 GB RAM, Intel Core i3 2.93GHz processor was the primary computer used for data acquisition. It interfaces with the infrared camera via an Ethernet cable and FLIR ResearchIR software to visualize and save the information captured by the camera. Another Dell computer with 32MB RAM, Intel Xeon 3.60GHz processor was the primary computer used in the analysis of data collected during experimentation. MATLAB 9.2 was used to develop the algorithms used for the image analysis and identification processes.

CHAPTER 2

2.0. LITERATURE REVIEW

This section provides important background information necessary to understand and fulfill the goals of this project and also illuminates the current state of research in the field.

2.1. BACKGROUND

The Gun Control Act of 1968 requires manufacturers of firearms to identify each produced firearm with a serial number. An amendment in 2002 to this Act specified minimal sizes for this serial number of 1/16" in height and 0.003" in depth [71]. The Act makes it illegal to deface a firearm's serial number or even to possess a firearm with its number defaced. Firearm tracing is an integral part of criminal investigations involving the use of a firearm. The Bureau of Alcohol, Tobacco, Firearms and Explosives (ATF) runs a National Tracing Center (NTC) which maintains the capacity to trace registered firearms. The ATF estimates that between 9 and 20 percent of firearms recovered across the United States as evidence from crime scenes have had their serial numbers obliterated [2].

Several methods are used by different manufacturers to apply serial numbers. These include methods that require the application of a mechanical force including die stamping, pin or stylus marking and roll marking, engraving which is a chip cutting operation that grinds off sections of the metal, and laser etching which utilizes an intense laser beam to alter the structure in the material [3].

Most firearms are made of some type of metal that is usually a variation of steel or aluminum [12]. The atomic structure of metals is crystalline, comprised of small units called grains [4]. The arrangement of these grain structures is directly connected to the behavior of the alloy and its thermo-physical properties [7]. The stamping of a serial number onto metals, by the application of a physical force to its surface, causes a permanent deformation, leading to an alteration of the

underlying crystalline structure [5–10]. The grains within the crystalline structure are densely packed together and become elastically strained when the physical force is applied. An increase in force extending beyond the elastic limit of the metal causes a permanent deformation by dislocations through the crystalline structure [4,5]. Figure 2.1 shows an example of the dislocations occurring in the crystalline structure [72].

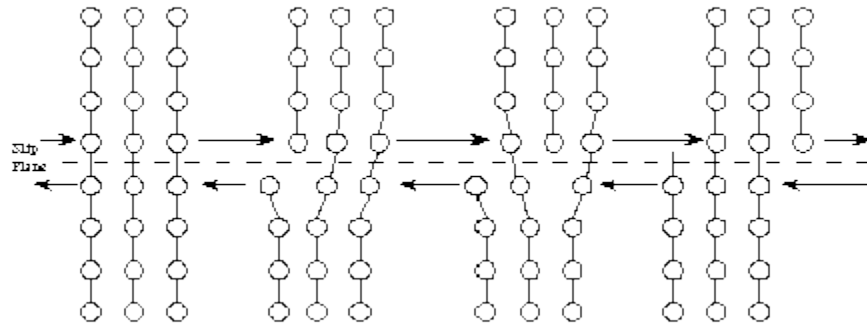


Figure 2.1 Dislocation movement in a crystal

The deformation resulting from a physical force on the metal results in the creation of two zones within the cross section of the metal: the elastic and plastic zones of deformation [3]. This resulting deformation of the plastic zone also known as the cold worked region extends to a depth beyond the stamped mark and is known as the zone of plastic strain [5–10]. Figure 2.2 shows an example of the extension of this region of plastic strain beyond the visible mark from the force of stamping.

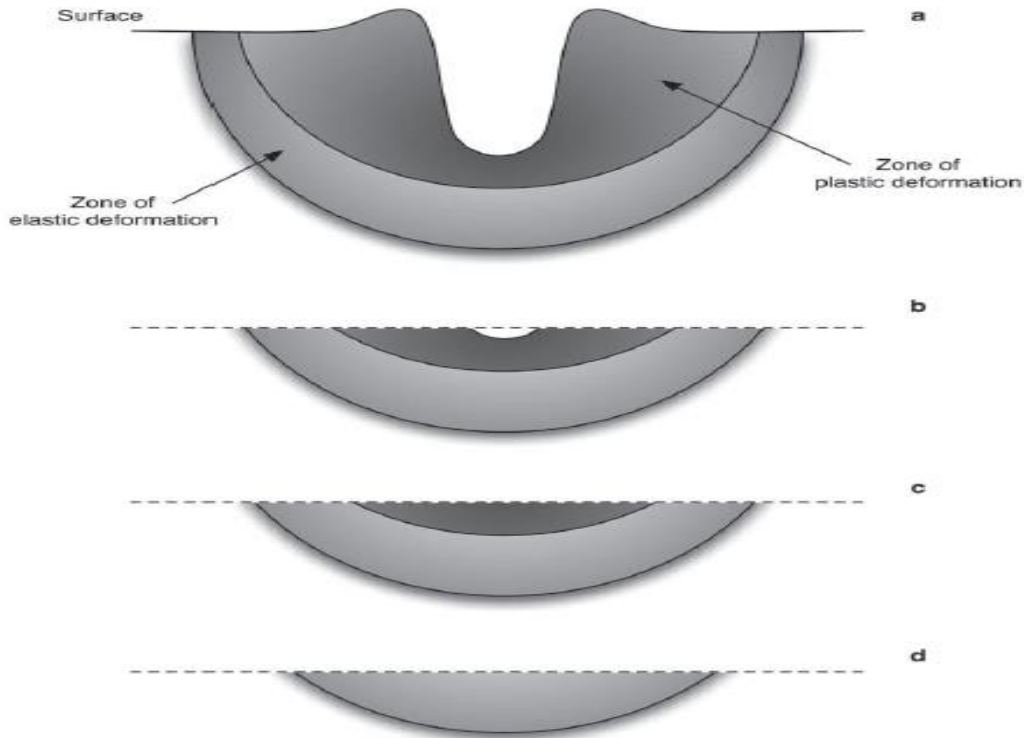


Figure 2.2: Diagrammatic representation of zone of plastic strain [3]

This depth of the zone of plastic strain is important in recovering defaced serial numbers as if material is removed beyond this zone, it becomes impossible to recover the number. As shown in Figure 2.2a, the fully formed zone of plastic strain from a stamp mark extends beyond the visible deformation created by the force of stamping. Figure 2.2b shows the removal of material off the surface resulting in a partial erasure of the stamp mark although enough of it still remains to allow it be discerned by careful polishing and viewing under a high powered microscope. Figure 2.2c shows the removal of enough material to erase any visible traces of the stamp mark. The zone of plastic strain created still exists and the various recovery methods can be used to attempt a recovery of the number. Figure 2.2d shows a scenario in which enough material has been removed to erase even the zone of plastic strain. In such a scenario, recovery of the defaced number will be impossible.

Although the shape of this underlying region (zone of plastic strain) will be complex depending on various factors including angle of the force applied and shape of the die, it can be generalized as a sphere to estimate its depth as a function of the yield stress at the surface of the sphere and the force applied to cause the deformation [11]. The radius of the sphere and by extension, the depth of the zone of plastic strain can be calculated using Equation 2.1 [11].

$$r^2 = \frac{\text{force applied}}{4 * \pi * \text{yield stress}} \quad (2.1)$$

where;

r is the radius of the sphere and correspondingly the depth of the zone of plastic strain,

force applied refers to the force used in making the stamp, and

yield stress is the material property defining plastic behavior.

The change in the crystalline arrangement of this local zone of plastic strain causes localized changes in the physical and chemical properties of the area. Some properties which would experience change with this deformation include hardness, tensile strength, electrical resistance, chemical potential, magnetic retentivity, and thermal conductivity. [12]. These local property changes are the basis for any methods to detect the zones of plastic strain after any visible indicators of these zones have been removed, and they are exposed to the surface following the defacing of the numbers.

A similar situation occurs in laser engraved metals as well. The laser engraving process marks the metal using the intense heat generated by a focused laser beam to alter the structure in the material. The process also liquefies the region below the engraved number and the rapid cooling of the metal may not allow for the reformation of the deformed crystals into the original

arrangement creating what is referred to as a heat affected zone (HAZ)[3]. This will alter the thermo-physical properties of the region as compared to the rest of the untouched metal.

Usually, methods used to remove or deface serial numbers involve processes that will remove enough material from the object until the serial number is no longer visible. These include filing, sanding and scraping with a sharp tool [3,4,12]. Another method in use is over stamping in which another number is stamped over the previous number to change it. Over stamping can result in the creation of new zones of plastic strain that will obscure any left off from the initial stamp and thus inhibit recovery [3,4].

Several methods have been tested for the restoration of serial numbers, leveraging on the local change in physical and chemical properties of the defaced area. These methods include chemical etching using a chemical solution, electrolytic etching by electrolytic process, ultrasonic cavitation, magnetic particle procedure, relief polishing, scanning acoustic microscopy and electronic channeling contrast [3,12].

Of these methods, chemical etching, electrolytic etching, ultrasonic cavitation, magnetic particle procedure and relief polishing are well established and generally used. However chemical etching, electrolytic etching and ultrasonic cavitation are destructive processes which will permanently alter the specimen under observation. As such, great care and some expertise is needed to utilize these methods in practice as their effects are irreversible and would permanently destroy what could be crucial evidence.

The most commonly used method is chemical etching. Researchers observed that it is possible to examine the grain structure of a metal using a controlled corrosion process. This process, when applied across a surface with the grain structure dislocated in some regions, will result in a

difference in the rate of reaction between the deformed and non-deformed sections to the applied etching solution due to the differing chemical potential within these regions. This will lead to a visible contrast between both regions due to a differential reflection from the defaced area to the clean areas. The etching process involves polishing the surface of the metal to a fine finish and then treating it with an appropriate chemical solution depending on the composition of the metal alloy which will preferentially dissolve metal at the point where a dislocation intersects the surface of the sample [7–11,73].

Wilson [7] opined that because the cold worked region is more chemically active than the surrounding areas, it will dissolve in an acid at a more rapid rate resulting in a local change in reflectivity of light, and this can be leveraged upon to reveal obliterated marks. In utilizing this method, the acid is carefully applied to the metal surface often via a cotton-tipped applicator or in some cases immersion. Recovered marks are sometimes very faint and can only be seen at certain angles of illumination. Also, parts of the number will appear and disappear as a function of the number of applications of the etchant. This highly varied and destructive nature of the chemical etching process makes it very important to record the process photographically so as to reconstruct the entire number from piecewise images from the etching process [7–10]. Different acidic solutions are used as etchants, and work best on different metals or alloys. Empirical testing over time has resulted in a list of etching solutions commonly used for some common metals and alloys. Table 2.1 shows a list of these solutions and the materials they are best suited for [3].

Table 2.1: Chemical solutions used for chemical etching for different materials.

Substrate	Solution	Details
Cast-iron and steel	Fry's reagent	90g copper chloride (CuCl_2) 120ml hydrochloric acid (HCl) 100ml water
Stainless steel	Acidified ferric chloride	5g iron chloride (FeCl_3) 50ml hydrochloric acid (HCl) 100ml water
Aluminum alloys	Dilute sodium hydroxide	10g sodium hydroxide (NaOH) 90g water
Brass and copper	Acidified ferric chloride	19g iron chloride (FeCl_3) 6ml hydrochloric acid (HCl) 100ml water

Electrolytic etching involves the application of an electric field to the sample to control the etching process. An external power source is used to facilitate electrolysis of the metal [12]. The metal to be etched is connected as the anode to the power source (DC) and a wire tipped with a cotton swab is used as the cathode. This cotton swab is immersed in the etching solution and used to etch the metal surface while a voltage is applied across the electrodes. There is generally an optimal voltage (depending on the metal alloy) that will give the best results in the electrolytic etching process [3,4,12]. This process is used in some instances to speed up the etching process and by reversing the polarity can also be used to slow the reaction rate [4].

Although chemical etching has proven quite successful at recovering obliterated serial numbers, it is a destructive technique which does not permit reproducibility [19]. This, the time needed for the restoration as well as the fleeting nature of the developed images are reasons for concern in the use of this method for serial number restoration. The total amount of time is variable but may take several hours as evidenced in a particular study to restore stamped marks on aluminum motorcycle frames where it took as long as six hours to cycle through the process and restore the marks on the frames [9].

As such, the development of a non-destructive restoration method remains a desired goal of forensic scientists. Several possible nondestructive restoration techniques have been explored as alternatives with varying degrees of success [19]. Magnetic particle inspection, the most commonly used nondestructive technique, relies upon a difference in magnetic permeability between the zone of plastic strain and the pristine (non-deformed) area to recover the defaced serial numbers [74]. Used by metallurgists to detect subsurface flaws in metals and alloys, this technique involves magnetizing the specimen under observation and then spraying the surface with fine magnetic particles. These magnetic particles will migrate on the surface and settle around areas where a subsurface defect or discontinuity exists, reconstructing the defaced number [3,4,12,74]. The cold working of steel (application of a force to cause plastic strain) changes its magnetization behavior as the defaced regions do not magnetize as readily as the pristine metal. This resistance to magnetization is due to the dislocation of the grain boundaries inhibiting the rearrangement of the ferromagnetic domains existing in a disordered arrangement prior to magnetization of the metal [4].

Various methods have been tested for use in temporarily magnetizing the specimen including using a yoke magnet, inserting into a coil electromagnet, and passing direct current from a

magnetic testing unit through the sample [12]. Each of these methods acts with the same principle of creating a magnetic field within the sample, which is disrupted by the presence of subsurface defects. The magnetic powder sprayed onto the surface will visibly identify these defective areas with lower levels of magnetization as the magnetic particles will be attracted to the boundaries, outlining the defaced area and presumably the number that previously existed [4].

Although proven to be quite effective in the restoration of defaced numbers, the magnetic particle inspection method has some shortcomings. These include only being applicable to ferromagnetic alloys and magnetic metals. Also, this method is limited to cold worked markings (that is mechanically stamped serial numbers) and has only limited applicability to laser engraved serial numbers.

Other nondestructive methods of recovery under investigation include relief polishing, x-ray imaging, electron channeling contrast, and scanning acoustic microscopy. However, these methods are experimental and their effectiveness is yet to be established [73].

2.2. INFRARED THERMAL IMAGING

A non-destructive method that may prove effective for restoring stamped and laser engraved serial numbers is infrared thermal imaging. This method, well established for use in the detection of anomalies in materials, seeks to locate and characterize flaws by capturing their effect on heat flow through the material by observation of the propagation of applied thermal energy [14].

Light is the broad spectrum of continuous energy called the electromagnetic spectrum. This electromagnetic spectrum consists of several regions including gamma rays, x-rays, ultraviolet rays, visible, infrared, microwave and radio waves [75]. These regions or bands, grouped based on frequency are distinguished by the methods used to produce and detect the radiation. These

frequencies are defined in terms of patterns of photon movement or waves, with each wave characterized by its amplitude and wavelength [76]. Radiation in the bands are governed by the same physical properties and only differ in amplitude, frequency and wavelength.

The infrared region of the spectrum lies between 0.7micrometers and 500 micrometers. It is further divided into three sub regions namely near infrared region (NIR) between 0.7 and 2.5 micrometers, middle infrared region (MIR) between 2.5 and 20 micrometers and the far infrared region (FIR) between 20 and 500 micrometers [76].

The interaction of thermal energy with an object occurs in three ways. These are conduction, convection and radiation. Infrared thermography takes advantage of the infrared radiation associated with the heating of an object. The intensity of the infrared radiation emitted by an object is mainly a function of its temperature, increasing with an increase in temperature. Infrared thermography (IRT) is based on the infrared spectral band, and involves collecting and processing thermal information from objects using non-contact methods [77]. With several advantages including collecting data in real time, being non-contact and non-invasive and providing two dimensional thermal images, IRT is the nondestructive evaluation method of choice for many applications in varying fields including medicine, non-destructive testing, maintenance, and process monitoring [77].

Two primary approaches are used in IRT; passive and active thermography. Utilizing the same principles of capturing thermal radiation off the surface of an object under investigation, these two methods differ primarily in the method of thermal excitation used. In passive IRT, no external thermal excitation is applied to the object and thus its natural ambient temperature is the focus of investigation. Active IRT on the other hand requires the use of external thermal stimulation to induce thermal contrasts between regions of interest, with the propagation of the

thermal energy through the object captured and used to investigate material behavior[14,15,24–26,77,16–23].

Active infrared thermography is made up of four primary components which are [13]:

1. Controlled application of thermal energy into the object under observation,
2. Propagation of the thermal energy through the object,
3. Capturing the surface temperature across the surface in real time, and
4. Interpretation of the spatial and temporal features of the temperature distribution across the surface.

These four components are integral to employing active infrared thermography in non-destructive testing, to capture and discretize differences in the propagation of thermal energy in areas with subsurface defects and areas without defects.

The theories that help guide this method are based on a heat conduction model which describes the temperature distribution in a heated material as obeying the general one dimensional heat transfer equation [15,17] as shown in Equation 2.2. This model, based on Fourier’s law of conduction, relates the amount of heat transfer in a material to three factors namely temperature gradient, cross sectional area and thermal conductivity [15,17].

$$\frac{d^2T}{dx^2} - (\rho c/k) \frac{dT}{dt} = 0 \quad (2.2)$$

where:

T is the surface temperature,

x is the perpendicular distance from the surface of the heated sample,

t is the time,

ρ is the material density,

c is the heat capacity and,

k is the thermal conductivity.

One of the basic modes of thermal transport, the electron transport mechanism, assumes that the heat is transported by free electrons that move through the lattice. As such, in a perfect crystalline lattice, this will be fairly linear but in materials with imperfections such as surface or subsurface defects, changes in the crystalline structure will lead to changes in the thermal conductivity. The thermal conductivity is a physical property that defines the material's ability to conduct heat and local changes to it will cause a disruption to the heat flow, resulting in a local change in thermal gradient [17].

When there are defects in the material, the propagation of the thermal wave in the defective regions will differ from that of the rest of the bulk material and thus, there will be multiple local conduction equations governing the heat flow in each area as seen in Equations 2.3 and 2.4 [17].

$$\frac{d^2T_0}{dx^2} - (\rho_0 c_0 / k_0) \frac{dT_0}{dt} = 0 \quad (2.3)$$

$$\frac{d^2T_1}{dx^2} - (\rho_1 c_1 / k_1) \frac{dT_1}{dt} = 0 \quad (2.4)$$

where:

0 represents the non-defective region, and

1 represents the deformed areas.

At the boundaries connecting these two regions, the temperatures are the same and the boundary conditions are written as shown in Equations 2.5 and 2.6.

$$T_0(x, t) = T_1(x, t) \quad (2.5)$$

$$-k_0 dT_0/dx = -k_1 dT_1/dx \quad (2.6)$$

These equations suggest a possible way of utilizing the change in thermal conductivity to identify defective regions and restore defaced serial numbers. From equations 2.5 and 2.6, even though the instantaneous initial temperature of the plastic region and non-deformed regions are the same, the temperature gradients will be different since the thermal conductivity and perhaps the density and heat capacities of the two regions will be dissimilar. Thus, if the amount of thermal energy transferred into the material is held constant, changes in the thermal conductivity or cross sectional area will directly affect the temperature gradient within the material. Consequently, by monitoring the temperature gradient in a material due to a thermal wave passing through it, the deformed regions should be detectable. The process of observing this phenomenon involves the use of an infrared camera and heating apparatus to capture the flow of thermal energy through an object to detect inconsistencies in the thermal flow.

Killey and Sargent [14] in a series of experiments to determine the best experimental conditions for infrared thermal imaging, came to some conclusions for obtaining maximum contrast between areas with subsurface defects and those without defects by utilizing numerical models. These conclusions include heat sinking the back wall of the sample to reduce lateral heat flow, and application of a profiled heat flux. As such, an ideal thermographic technique to locate these zones of plastic strain in a stamped metal piece to recover the defaced serial number will need to include these conditions to improve workability.

Several experimental configurations for infrared thermal imaging research are currently being investigated for adaptation to real world applications [14,17,19,20,25,26]. These are based on

different methods of thermal excitation. Generally, the methods can be divided into conventional (transient) thermography, pulsed thermography and lock-in thermography [26,77].

Conventional thermography also referred to as step heating or transient thermography involves the application of thermal energy to an object and then observing the subsequent thermal decay of the energy flux through the object [77,78]. In this approach, the change in surface temperature is monitored as a function of time and will differ between areas with subsurface defects and those without any defects due to the change in local thermal conductivity. As such, hot or cold spots will appear at certain points in time indicating local regions with distinct thermal conductivities and possibly subsurface defects [77,78].

Pulsed thermography involves introducing a short energy pulse from a heating source into an object and then recording the temperature decay curve [26,77]. This short pulse could last anywhere from a few milliseconds to a few seconds, subject to the requirements of the experiment. Over time, the thermal wave will propagate through the object and the temperature of the surface will decrease uniformly except in areas over subsurface defects. These defects will act as resistance to heat flow, producing abnormal temperature patterns on the surface above them that can be captured by an IR camera [79]. Although fast and easy to deploy, pulsed thermography images are affected by a number of challenges including possible non-uniform heating, emissivity variations and surface radiation [26,80]. One method which has proven effective in overcoming some of these issues is lock-in infrared thermography technique (LIT) [16,21–25].

2.2.1. Lock-In Infrared Thermography

Lock-in Infrared Thermography (LIT) involves inducing sinusoidal energy waves at a lock-in (modulation) frequency into the surface of an object under observation. The heat flow as the

thermal wave propagates through the object will be affected by thermal conductivity differences across the observed surface, so changes in the phase of the wave are experienced. The temperature changes are observed at the frequency of the input pulse (the modulation frequency) using thermographic images collected over the entire period of the pulsed wave. These images reveal information about changes in the thermal conductivity of the object across the surface under observation [25]. Digitally processed according to the lock-in principle, the thermographic image sequence is analyzed and compressed into an amplitude image and a signal phase image which display the local variation in phase or amplitude between defective and non-defective areas. [21–23]. These developed images have some surface features suppressed making them less sensitive to uneven heating and local emissivity variations which are concerns in using other thermal imaging techniques. This is an advantage of LIT over other thermography techniques as it results in images with better surface temperature signals, which are more robust than thermal images for analyzing subsurface features [21–24]. Bai and Wong [24] showed that LIT is particularly useful for detecting near surface defects because of its sensitivity to interfaces between materials as is created with a local change in thermal conductivity in defective areas.

The principle of LIT is described in [21]. A sinusoidal energy wave is induced into the surface of a sample and an infrared camera is used to collect thermal images of the sample surface over the entire period of the pulsed wave. A 2 channel image correlation procedure involving multiplying each collected image by two sets of weighting factors, and then summing together all the results is used to develop one in-phase image (0°) and a quadrature (-90°) image as shown in Equations 2.7 and 2.8.

$$S^{0^\circ} = \frac{1}{n} \sum_{k=1}^n \sin(t) * F_k(t) \quad (2.7)$$

$$S^{-90^\circ} = \frac{1}{n} \sum_{k=1}^n -\cos(t) * F_k(t) \quad (2.8)$$

where:

n is the number of frames per lock-in period,

F_k is the image collected,

t is the time,

$\sin(t)$ and $\cos(t)$ are weighing factors.

A phase independent amplitude image A, and a signal phase image ϕ are then generated using Equations 2.9 and 2.10.

$$A = \sqrt{(S^{0^\circ})^2 + (S^{-90^\circ})^2} \quad (2.9)$$

$$\phi = \tan^{-1} \left(\frac{S^{-90^\circ}}{S^{0^\circ}} \right) \quad (2.10)$$

Another possible image that could be used to visualize dissimilar thermal gradients is the inverse phase image. This image is formed by dividing the in phase signal (S^{0°) by the out of phase signal (S^{-90°) as shown in Equation 2.11. Researchers in earlier studies[23,81] opined that this image is superior to the regular phase images as it gives better spatial resolution while still damping out effects of emissivity.

$$S^{0/90} = \frac{S^{0^\circ}}{S^{-90^\circ}} \quad (2.11)$$

As in cases like this study when it is suspected that the thermal gradient differences are very small, using this inverse phase image might improve contrast helping to recover the number. As such, this method is used in this study to develop the phase images. Also, to improve contrast in

the amplitude images, the fourth power is used instead of the square of the in-phase and quadrature signals. This reduces the effects of the emissivity multiplier for each signal and improves the output image.

A major drawback of LIT is blind frequencies i.e. pulsing frequencies at which the contrast between clean areas and defective areas is minimal. Defect detection in phase images developed at these frequencies is usually difficult and thus, such frequencies need to be avoided. This shortcoming is addressed by calculating phase images over several thermal input frequencies and determining the phase differences between defaced and non-defaced areas. The frequencies at which these differences are maximized are selected to be used for the experimentation[16,24,25]. Equation 2.12 shows the computation of the phase difference.

$$\Delta\phi(x, y) = \phi_d(x, y) - \phi_s(x, y) \quad (2.12)$$

where:

$\Delta\phi(x,y)$ is the phase difference of the pixel (x,y),

$\phi_d(x,y)$ is the phase of a pixel in the defect area and,

$\phi_s(x,y)$ is the phase of a pixel in a sound area.

The modulation frequency used in LIT experiment is important as it affects the depth to which defects in an object can be observed as shown in Equation 2.13. This relationship indicates the depth of penetration (μ) for flaw characterization in a material to be inversely proportional to the modulation frequency [25].

$$\mu = \sqrt{\frac{k}{\pi f \rho c}} \quad (2.13)$$

where:

μ is the thermal diffusion length,

k is the heat conductivity,

f is the modulation frequency,

ρ is the density, and

c is the heat capacity.

There will be an optimal frequency for observation of the defects induced by the metal stamping which will depend both on the physical characteristics of the sample such as the overall and local thermal conductivities as well as the depth and thicknesses of the defects. There will also exist as observed in [16], blind frequencies at which the phase shift between the defective areas and the background will be minimal, making the defects difficult to distinguish in phase images at these frequencies. Decrease in size or increase in depth of the defects from the surface leads to a reduction in the range of frequencies at which the defects can be adequately captured, and also an attendant increase in the range of blind frequencies [25].

With defaced serial numbers, the defects are exposed to the surface and extend to some depth below it with respect to stamping pressure and the amount of surface material removed during defacing. As a result, it is necessary to inspect both the amplitude images which capture surface and near surface information as well as phase images which capture deeper lying information in a bid to recover the defaced numbers.

In previous studies, researchers [24] developed a numerical model to predict the phase values of a sample under observation at different pulsing frequencies. This model, designed to be used for a clean sample (as a single layer sample) as well as a defective one (multilayer sample), utilizes the thermo-physical properties of the material to predict heat flow through the sample and determine phase values at the surface due to the heat flow. Equations 2.14 and 2.15 show the model for a single layer. For a multilayer sample as is the case with defective samples, the thermo-physical properties of each layer are considered in the model and a system of equations developed to show the relationship. An example of the matrix of equations can be found in [24].

$$T_a(0) = \frac{Q_0}{2} * \frac{(h_r+k\sigma) \exp(2\sigma L)-(h_f+k\sigma)}{(h_f+k\sigma)(h_r+k\sigma) \exp(2\sigma L)-(h_f+k\sigma)(h_r+k\sigma)} \quad (2.14)$$

$$\sigma = (1 + j) \left(\frac{\omega}{2\alpha} \right)^{1/2} \quad (2.15)$$

where:

$T_a(0)$ is the ac component of temperature at the surface of the sample,

Q_0 is the intensity of the heat source,

h_r is the heat transfer coefficient of the rear surface,

h_f is the heat transfer coefficient of the front surface,

k is the thermal conductivity of the sample,

ω is the angular modulation frequency,

α is thermal diffusivity = $k/\rho c$

ρ is the density of material,

c is the specific heat of material,

L is the thickness of sample.

This model allows for the estimation of the phase values over the surface of a sample with subsurface defects from an input thermal energy flux. Comparing the values from an area over a defect to those from areas without defects, it is possible to develop phase difference plots showing the phase differences at different modulation frequencies. These plots help to determine the blind frequencies for a specific set of experiments.

A study using infrared thermography to recover paint covered and abraded marks [82], tested several active thermography techniques including pulse thermography, step heating thermography and lock-in thermography. The study showed these methods held some promise for wider use although the study was limited to recovering slightly abraded numbers and non-defaced numbers painted over.

Although infrared thermal imaging, being sensitive to local variations in thermal conductivity can be utilized to recover defaced serial numbers, this technique does have its possible shortcomings. One particular concern although partly mitigated by LIT is the sensitivity of the imaging apparatus to visibly capture what might be infinitesimal changes in temperature gradient across the surface. Another is the capture of other features including possible material inhomogeneities within the thermal depth range besides from the defects [22]. These could have a negative impact on the testing procedure and by extension the resulting images [18]. Various post processing methods tested to eliminate these effects and improve the contrast in thermal images include absolute thermal contrast, differential absolute contrast and thermosonic reconstruction method. However, these methods do have some drawbacks including the need to

specify sound and defaced areas in absolute thermal contrast [27], the need for operator interference in calculating slopes at each spatial point (differential absolute contrast) [26,27,83] and the possible removal of subtle defects from output images due to the low pass filtering (thermosonic reconstruction) [27,84,85]. A conceivable way to overcome these challenges is by multivariate image analysis.

2.3. MULTIVARIATE IMAGE ANALYSIS

Multivariate image analysis (MIA) involves the use of computational approaches in the examination of collected images to help with detection and analysis of possible variations within the data. Applied successfully in several fields of study including quality control in pharmaceuticals and food processing, remote sensing, chemometrics and evaluation of artwork [29–35], MIA has proven useful in such diverse applications particularly because of its capacity to perform fast and non-invasive analysis on products and processes [38]. The process of utilizing MIA on a sequence of images requires collecting the images and arranging them into a three dimensional dataset. Two dimensions of this dataset are the spatial dimensions of the images and the third, a variable connecting these images (time for thermal images). Multiple thermal images can be collected thus into a single dataset and the variation in the images over time analyzed. Multivariate image analysis can take several forms. A very popular one is principal component analysis (PCA).

2.3.1. Principal Component Analysis

This is a technique that transforms a collection of possibly correlated data into a new set of uncorrelated variables with given statistical properties that highlight the importance of elements within the data [28,29,38,30–37]. Commonly used in finding patterns in data of high dimensions, this technique relies on the basic assumption that inter-correlated descriptors exist within data to be analyzed. The technique develops a new set of uncorrelated descriptors for the dataset, each

of which is a suitable linear combination of all the original descriptors and are orthogonal to each other [36]. As such, PCA offers a method of constructing an adaptive representation of data to exploit its underlying distribution [37]. This representation is via principal component vectors, which are uncorrelated linear combinations of the input variables and are ordered by the amount of variation captured from within the data. When used for images, the images are unfolded into a vector and concatenated into a single input matrix on which PCA can be applied. Each of the vectors (variables) in the resulting principal component (PC) matrix can be folded into a two dimensional image (score image), which is of the same spatial dimensions as the original images and gives a visual representation of the information retained in that principal component. A well-used technique for performing PCA is singular value decomposition (SVD), which is the factorization of a dataset into the product of three matrices as shown in Equations 2.16 and 2.17 [28]. A particular advantage of SVD is that it can be defined for all matrices irrespective of shape (rectangular or square).

$$\mathbf{X} = \mathbf{U}\mathbf{\Sigma}\mathbf{W}^T \quad (2.16)$$

$$\mathbf{T} = \mathbf{U}\mathbf{\Sigma}\mathbf{W}^T\mathbf{W} = \mathbf{U}\mathbf{\Sigma} \quad (2.17)$$

where:

\mathbf{X} is the image matrix (collection of unfolded images into vectors),

\mathbf{W} is the loading matrix = eigenvectors of matrix $\mathbf{X}^T\mathbf{X}$,

\mathbf{T} is the principal component (scores) matrix,

\mathbf{U} is the eigenvectors of matrix $\mathbf{X}\mathbf{X}^T$, and

$\mathbf{\Sigma}$ is a diagonal matrix of singular values.

From the equations, PCA is performed to determine the principal component (scores) matrix (\mathbf{T}) from a matrix of unfolded images (\mathbf{X}). This principal component matrix is made up of score vectors each of which is associated with certain features from the original dataset and are orthogonal to each other. The first vector in the matrix (PC1) accounts for the largest possible variance in the original dataset and the next (PC2) for most of the remaining. Accordingly, higher principal component vectors account for a successively reducing amount of information from the data under observation. This makes PCA a useful data reduction technique as it can be used to identify redundant data and these can be removed by retaining only a certain number of principal component vectors [36]. However, in some cases, the information being sought does not represent a significantly large feature in the dataset and as such, could be contained in one of the higher PC's with lower variances. In such scenarios, it is necessary to retain all the vectors in the principal component matrix and scrutinize each individually to determine its importance or otherwise [86]. Each of these principal component vectors can be folded into a two dimensional image (score image), which is of the same spatial dimensions as the original images in the dataset. These images give a visual representation of the information retained in that principal component [28].

Several researchers have utilized the orthogonality and discretization properties of PCA in thermographic image analysis to improve defect detection and characterize flaw depth [29] as well as defect classification [87–89]. These studies have focused using PCA to improve contrast of thermal images obtained from transient thermography and pulsed thermography. However, the presence of some undesired features earlier alluded to in the thermal images might reduce the performance of PCA in characterizing very subtle thermal signatures. As such, implementing

PCA on amplitude and phase images which eliminate these features should improve the distinct characterization of these subtle thermal signatures in the PC scores.

After capturing and enhancing the thermal signatures representative of the zone of plastic strain in a score image, it is desirable to conclusively identify the number without bias via an automated process. This identification can be achieved by comparing the score images of the defaced area to a library of unaltered digits to determine the best match using similarity measures [39–43]. Ideally the images should be distinct enough that they can be correctly matched in the library without any confusions and robust enough that they can overcome external factors particularly differences in image sizes, translation, scale or rotation. These challenges can be overcome by comparing image features extracted via orthogonal moments, in lieu of the actual images.

2.4. FEATURE EXTRACTION

An important aspect of any pattern recognition system is the automatic recognition of an object irrespective of its size or location within a captured image [52]. To achieve this, several methods have been tested, all of which involve transforming an image into a set of unique descriptive features that are representative of the image as a whole [51,59]. Some approaches to carrying out this include methods that extract statistical features such as zoning, methods that yield global descriptors such as moments, and methods that exploit geometrical and topological features such as strokes and chain codes [51,52,59]. Ghorbel et al [60] noted that that the most important properties for a good feature extraction technique include invariance against some geometric transformations (scale, translation and rotation), stability to noise, blur and small local deformations as well as completeness in describing the shape of an object. A method which has proven to be very robust in meeting these attributes is moment invariants.

Moments are scalar quantities used to characterize a function and capture its significant features. In image processing, they are measurable quantities which are insensitive to particular deformations and provide enough discrimination power to distinguish among objects belonging to different classes [54]. Also, moments with orthogonal basis functions, represent an image with a set of mutually independent descriptors, thus minimizing redundancy [61].

Regular or geometric moments which form the basis for most moment based feature extraction techniques are defined by Equation 2.18 [52].

$$m_{pq} = \int_{-\infty}^{\infty} \int_{-\infty}^{\infty} x^p y^q f(x, y) dx dy \quad (2.18)$$

where:

p and q are non-negative integers,

m_{pq} is the (p+q)th order moment of the continuous function $f(x, y)$.

For digital images with discrete pixel locations, the integrals are estimated with summations. These essentially define moments by projecting a function onto a monomial basis set $x^p y^q$. However this basis set is not orthogonal and as such, there is some redundancy in the information content of the moments developed [52].

To counter this shortcoming, various types of orthogonal moments have been developed and used in image recognition processes to varying degrees of successes [54,58–60,62]. Two classes of orthogonal moment invariants which have proven to extract robust invariant features for the classification of images, are Zernike moments and pseudo Zernike moments [52–58].

2.4.1. Zernike Moments

Researchers [54] proposed the use of Zernike moments based on orthogonal polynomials first proposed by Zernike (hence the name), for use in characterizing images. The polynomial set first proposed by Zernike form a complete orthogonal set over the interior of a unit circle and are of the form shown in Equation 2.19 [52].

$$V_{nm}(x, y) = V_{nm}(\rho, \theta) = R_{nm}(\rho) \exp(jm\theta) \quad (2.19)$$

where:

n is a number of basis polynomials that define the order of Zernike moments,

m is a positive or negative integer bound by the constraints $n - |m| = \text{even}$ and $|m| \leq n$,

V_{nm} is the Zernike polynomial,

R_{nm} is the real valued radial polynomial,

ρ is the length of the vector from origin to the (x, y) pixel, and

θ is the angle between the vector ρ and the x axis in counterclockwise direction.

Zernike moments are rotation invariant and images could be preprocessed to make them scale and translation invariant, thus removing these variables from the image classification problem [52,55–58]. Such preprocessing is achieved using affine transformations to map variables (pixel intensity values at a location in the case of images) into new variables (new locations for images) by applying a linear combination of translation and scaling operations [90].

With the rotation invariance of Zernike moments, the rotation of an image does not change the magnitude of its Zernike moments. Another useful property of Zernike moments is the orthogonality of the orders of basis polynomials. This orthogonality property makes it possible to

determine the quality of features extracted at each order of basis polynomials by reconstructing the images at the particular order [52]. These properties (orthogonality of orders and rotation invariance) make Zernike moments more suitable as a global shape descriptor for object classification than other moment based shape descriptors including general orthogonal moments, Legendre moments and Jacobi Fourier moments [52–58].

Zernike moments employ complex Zernike polynomials as the basis sets. The process of extracting the moments of an image requires the definition of a finite order of basis polynomials (n). As feature vectors can be constructed to an arbitrarily high number of Zernike polynomial orders, it is pertinent to determine the number of orders that capture enough features in an image to adequately classify it. Zernike moments due to their orthogonality property, capture unique features at different orders, minimizing information redundancy. Increasing orders of Zernike moments capture increasingly finer details of an image. However, higher order Zernike moments are very sensitive to noise and can become quite unstable, making it imperative to determine an optimal range of orders at which the features in an image of interest are best captured [58]. A good way of estimating this is by the reconstruction error at a particular order [52,55]. This requires the comparison of the original input image to its reconstructed version from a set of Zernike moments at a specified Zernike polynomial order. The lower the reconstruction error, the better the order is at capturing the features in the image. The mean square reconstruction error (ε) between the original image and its reconstructed versions at increasing orders can be used as a comparative measure to determine this difference as shown in Equation 2.20.

$$\varepsilon = \frac{\sum_{i=1}^N \sum_{j=1}^N (f(x_i, y_j) - \hat{f}(x_i, y_j))^2}{\sum_{i=1}^N \sum_{j=1}^N (f(x_i, y_j))^2} \quad (2.20)$$

where:

$\hat{f}(x, y)$ is a reconstructed pixel using the extracted feature vector,

$f(x, y)$ is the corresponding pixel from the original image,

ε is the image reconstruction error, and

N is the number of pixels in the x and y directions.

This reconstruction error corresponding to a set of Zernike moments at a defined order can be used as a measure of the validity of the order as representative of the features of the original image. To determine the appropriate order, the contribution of each respective order moments to the reconstruction process is measured by the difference in its reconstruction error from the next order (n) and this difference $C(n)$ is computed as shown in Equation 2.21 [52,54]:

$$C(n) = \varepsilon_{n-1} - \varepsilon_n \quad (2.21)$$

where:

n is the order of Zernike polynomials, and

ε is the mean square error of reconstruction at a particular order.

A positive value of this difference indicates that the particular order (n) captures pertinent information necessary to reconstruct the original image and a negative value indicates that the captured features in the corresponding order are of less importance to the entire image than those captured at the prior order. These difference values can be used for preselecting orders to use during the classification of images. They can also be used as a weighing mechanism to weigh moments of different orders in the classification scheme with respect to their importance to reconstructing the original image as described in [52].

Preselecting the polynomial orders to use during classification is done by selecting only moments at orders with values of $C(n)$ greater than zero to use in the classification of the images. Moments at orders with a negative difference in reconstruction error are eliminated assuming they do not contribute any important information from the original image not captured in another order and thus do not need to be used in classification. Weighting the moments during classification will mean that the moments at orders determined to carry more pertinent features are weighed higher in the classification scheme than those at orders deemed less important with respect to the value of the difference in reconstruction error. The weights for each order are determined as shown in Equation 2.22 [52].

$$w_i = \frac{C(i)}{\sum_{j=1}^s C(j)} \quad (2.22)$$

where:

s is the number of orders with positive values in C ,

C is the vector of all positive values of the difference in reconstruction errors calculated in Equation 2.20.

Larger weight values indicate that the corresponding order captures much more information than the prior and vice versa. These weights are ranked from 1 through the highest number of orders not weighed zero with higher ranks corresponding to higher weights for orders deemed to capture more features than others.

A downside to Zernike moments is the excessive amount of computation power needed to compute the moments. To circumvent this, Deng et al [59] proposed using only the non-negative repetitions of the Zernike polynomial orders as the repetitions are symmetrical about the zeroth

order. This will reduce the number of moments in the Zernike moments vector from containing $\frac{1}{2}(n + 1)(n + 2)$ to the values shown in Equation 2.23.

$$\begin{cases} \frac{(n+2)^2}{4} & \text{for even } n \\ \frac{(n+1)(n+3)}{4} & \text{for odd } n \end{cases} \quad (2.23)$$

With the reduced number of moments, the computation time for calculating the moments is also reduced increasing the viability of using Zernike moments for feature extraction in a classification scheme.

2.4.2. Pseudo Zernike Moments

Constraints on the repetitions of the order of Zernike polynomials limiting Zernike moments to containing $\frac{1}{2}(n + 1)(n + 2)$ linearly independent descriptors, reduce the image representation performance of Zernike moments [63]. An improved basis polynomial set (pseudo Zernike polynomials) eliminates this constraint, increasing the number of independent descriptors to $(n + 1)^2$, thus enhancing the feature representation performance of the computed moments [63,64]. Besides from this redefinition of the basis polynomials, the process for developing pseudo Zernike moments stays the same as that for regular Zernike moments.

Several researchers [52,53,63–65,55–62] have used feature vectors from different iterations of Zernike and pseudo Zernike moments to successfully classify a wide range of images including faces, digits and other objects. This classification requires the use of similarity measures to determine the similarity or dissimilarity between the feature vectors and reference libraries.

2.5. SIMILARITY MEASURES

Classification in image analysis is the process of assigning a new item to its proper place within an established set of categories [47]. This assignment is done using some mathematical formulations (similarity measures) to determine to which categories the item belong.

Similarity measures are computational methods of quantifying the similarity between objects, measuring the differences between them in space with a numeral value (similarity coefficient) indicating the degree to which the two objects are alike. This similarity coefficient, resulting from the measurement algorithm (similarity measure) indicates the strength of the relationship between two datasets.

Similarity measures uniquely determine any possible resemblance between different sets of data by measuring certain relationships between the datasets. These relationships could be a measure of the strength of the linear relationship between the datasets (such as Euclidean distance), the angle between them ($\cos \theta$) or the distance in space between them (such as determinant). Another method of comparison between datasets used is transformation merits (Procrustes analysis) [41]. These involve the determination of a transformation coefficient necessary to make one vector similar to another [41]. These similarity measures utilize different characteristics of vectors including shape and magnitude to make comparisons between them eventually resulting in a similarity value that defines how similar or dissimilar the vectors are within the characteristics captured by the measure.

The classification of a vector using a similarity measure may be complicated by imperfect class definitions, overlapping categories, and random variations in the data [47]. As such, employing several of these measures to compare vectors ensures that different defining characteristics are captured and used to give a holistic comparison between the vectors compared.

Utilizing several similarity measures to classify data will result in several results with each measure independently making a classification. It thus becomes pertinent to combine these individual measures in an unbiased way to determine a consensus for classification. Data fusion is a well-developed method used to establish such a consensus.

2.5.1. Data Fusion

Wald [48] defined data fusion as a formal framework in which are expressed means and tools for the alliance of data originating from different sources. The primary aim of data fusion is combining these otherwise independent data derived from different sources into a single informative output that improves the quality of the information [49]. Data fusion has become a widely used technique across several disciplines to combine data to enhance the information that could be gleaned across the data [48,50].

There are generally three levels of fusion that can be considered: low, mid, and high [45–47]. Each level of fusion combines data at different levels of processing. Low level fusion involves combining raw data from different sources or observed under different conditions. Mid-level fusion requires some preliminary analysis to be carried out on the data to extract some relevant features before combining. High level fusion utilizes processed data that could each be used in making a final decision into a single consensus output [45–47]. A large number of fusion algorithms have been proposed in literature, each primarily designed to effectively combine the data depending on its type [45,47]. These include simple mathematical formulations like sum and mean across the data to more complex formulations like principal component analysis and discrete wavelet transforms for fusing images from different sources.

As an important part of this study involves the use of multiple similarity measures in identifying the recovered numbers, it is possible that each measure used could in principle give differing

results with respect to the characteristics captured within them. As such, it is pertinent to combine these individual measures in a way that will establish an objective consensus as to the result of the comparison. A high level or decision level fusion approach is used in this study as it involves the fusion of several parameters (similarity merits), each of which can be used to make an independent identification [45–47], to yield a final inference.

To confidently apply this recovery and identification process, it is necessary to determine a confidence index for the identification. This confidence index will give an easy to understand measure of accuracy of the results from the classification. Several methods have been used to determine confidence levels for statistical analysis. A particular method used to assign confidence indices to the classification of unknown patterns is conformal prediction.

2.6. CONFORMAL PREDICTION

Conventional classification approaches as used in this study generally output a predicted label for unknown data but does not give any information as to the reliability of the prediction [66]. Information on the reliability is important in deciding how well informed an identification is and how much credence can be given to it. Conformal Prediction is a recently developed framework for complementing the predictions of machine learning algorithms with reliable measures of confidence, quantifying the uncertainty in the predictions made. This process gives confidence indices to the matching of unknown patterns to labels from known patterns. The methods developed based on this framework produce well-calibrated confidence measures for individual samples without assuming anything more than the data are generated independently by the same probability distribution [67,68]. As such, it doesn't necessarily determine the accuracy of the classifier in use but rather the precision of the label output from the classifier. Utilizing the algorithmic theory of randomness, it also gives control over error rates [67]. The confidence

levels produced by conformal prediction, allow for an easy to understand measure of reliability as it yields confidence on a scale of 0%-100% [69].

The main principles of conformal prediction require the definition of a nonconformity measure. Analogous to similarity measures, this measure is a real valued function that is used to measure how unusual an object looks in relation to other objects of its class compared to the other classes [67]. Using this function, the nonconformity algorithm will produce prediction regions for a probability of error. The size of this probability of error for a prediction region to contain only the one label assigned from the similarity measure determines the confidence level that can be placed on the prediction.

The nonconformity measure assigns a nonconformity score α , a numerical value indicating how unusual a sample is to each unknown sample with respect to other samples in a class. To determine how different each unknown sample x_n is from the known samples x_j in a class, its nonconformity score α_n is compared to the nonconformity scores of the known samples in the class α_j . This comparison is made by computing the percentage of nonconformity scores in a class greater than or equal to the nonconformity score for the unknown sample as shown in Equation 2.24.

$$p_n = |\{j = 1, \dots, n: \alpha_j \geq \alpha_n\}|/n \quad (2.24)$$

where:

p_n is the p-value for a particular sample,

α_j is the nonconformity score of a known sample compared to others in its class,

α_n is the nonconformity score of the unknown sample compared to others in the class,

n is the number of samples in the class.

This p-value (p_n) is an indicator of the ‘conformity’ of the particular sample to the class. If p is small (minimum of $1/n$), then the sample is considered nonconforming or very different from the other samples in the class and if p is large (maximum of 1), then the sample is considered to be conforming or very likely to belong to the class. The confidence is measured as one minus the second highest p-value and indicates the likelihood of the predicted classification to all other possible classifications. This value in percentage, gives a measure of how much trust can be put into the predicted classification.

Another index obtained from the conformal prediction algorithm is the credibility index. This is defined by the largest p-value, an indication of the fit of a particular sample to its assigned class. This value, also in percentage helps measure how different or alike the tested sample is from the reference samples [68], and in doing so establishes the suitability of the nonconformity measure used to make the comparison for the dataset under investigation. As such, the confidence defines how likely the predicted classification is compared to other possible classes and the credibility defines how suitable the nonconformity measure is for determining this confidence index.

CHAPTER 3

3.0. MATERIALS AND METHODS

The methodology designed for this study was formulated to overcome the identified challenges with non-destructive recovery of defaced serial numbers. Several samples simulating the applicable conditions were acquired for testing. The designed methodology used for testing the hypothesis is in several stages as outlined below:

1. Acquisition of samples
2. Data Acquisition
3. Image analysis
4. Number identification
5. Conformal prediction

3.1. SAMPLE ACQUISITION

Several samples were used in this study to develop the process of recovering and identifying defaced serial numbers. These samples included simulated test pieces of various types and a test case involving a stolen and retrieved motorcycle.

3.1.1. Stainless Steel Plates

To determine the validity of the lock-in thermography (LIT) experimentation setup, a sample and subsequently an experiment was designed to identify subsurface defects in a material. This experiment is similar to thermography experiments that have been successful in identifying these defects in different materials [16,24]. Three holes of 6mm diameter were drilled into a stainless steel plate (of dimensions 72mm x 25mm x 6.35mm) to depths of 5.3mm, 4mm and 1.8mm respectively. This was done to simulate subsurface defects and the LIT process was employed to identify these holes from the top surface of the plate. Figure 3.1 shows the holes drilled into the plate to different depths.

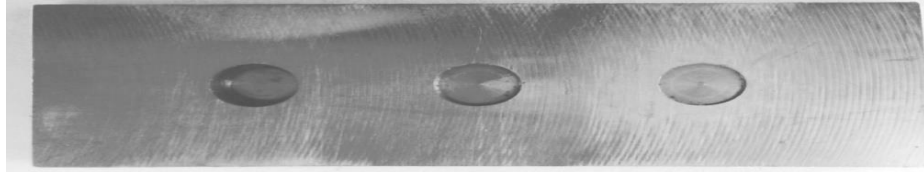


Figure 3.1: Stainless steel plate with holes drilled in.

The experimental process was mostly developed by testing on a stainless steel plate (72mm x 25mm) stamped with several numbers. This sample obtained as a test piece from Precision Forensic Testing [91], was stamped using an open back inclinable (OBI) press. The numbers were stamped to depths of approximately 0.17mm, 0.15mm, 0.15mm, 0.16mm and 0.18mm for the 2,6,2,5 and 0 respectively as measured using a profilometer. Originally 6.35 mm thick, the stamped numbers were defaced in a controlled manner. A uniform thickness of 0.16mm was mechanically shaved off the top surface, leaving the numbers barely visible. Each number except the first was then progressively shaved off to a depth 0.03 mm beyond the previous. The first number on the plate is left visible to serve as a control, ensuring consistent knowledge of the positions of the defaced numbers. Figure 3.2 shows the original sample. After the defacing, it is impossible to visually identify some of the numbers present before the material was removed. The sample was sanded using a 600 grit sand paper to polish off the surface and thoroughly cleaned with ethanol to remove any residue from the sanding process, ensuring a clean and smooth surface. Figure 3.3 shows this sanded and cleaned sample. The boxes show the areas around each defaced number isolated and individually analyzed.

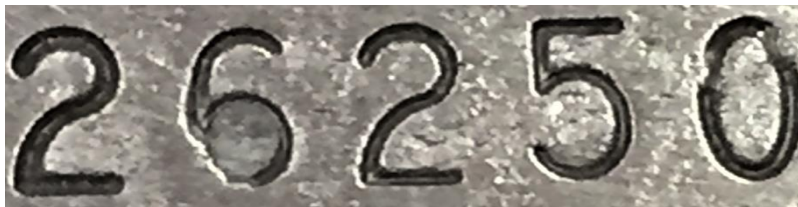


Figure 3.2: Stainless steel sample with stamped numbers.

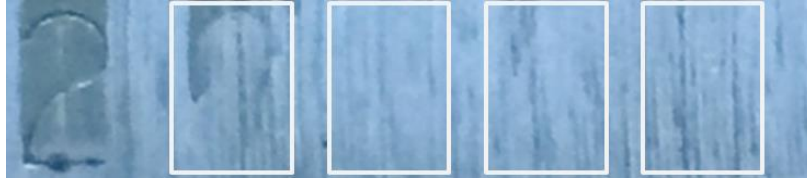


Figure 3.3: Stainless steel sample with numbers defaced (boxes show areas extracted and individually analyzed for each number).

3.1.2. Gun Barrel

Another sample acquired and defaced is a gun barrel for a Stevens Model 95 12 gauge shotgun. The shotgun had no serial number and so some numbers stamped on the barrel were defaced using a file to simulate the serial number defacing. Two numbers were defaced on the barrel surface and used to test the recovery process. Figures 3.4 and 3.5 show images of the barrel before and after defacing with the white box indicating the numbers removed.

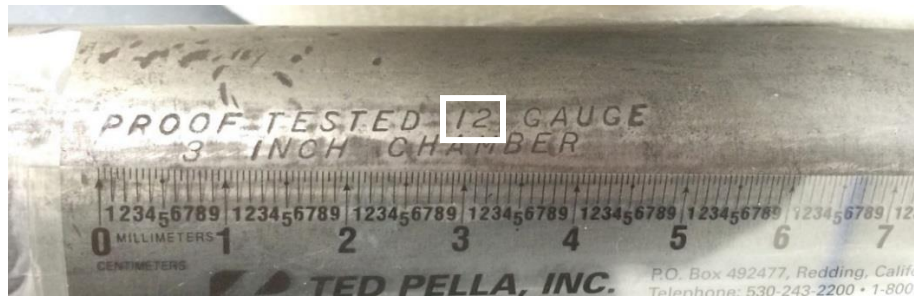


Figure 3.4: Gun barrel with identification marks stamped in.



Figure 3.5: Picture of the gun barrel after defacing the 1 and 2 from the label "12 gauge" (The India ink coating has been partially removed from the defaced areas for ease of viewing).

3.1.3. Laser Engraved Needle Holder

To test the efficacy of the method on laser etched samples, a laser engraved Aesculap surgical needle holder (Model BM034R) was obtained. Two of the laser engraved numbers were filed to simulate defacing serial numbers. Figures 3.6 and 3.7 show the needle holder before and after the numbers were defaced.



Figure 3.6: Laser engraved needle holder.



Figure 3.7: Defaced and painted needle holder.

3.1.4. Motorcycle VIN

A Yamaha model TY175 motorcycle with the vehicle inspection number (VIN) on its fork defaced likely using a Dremel tool ostensibly to prevent identification was obtained from the Idaho Power County Sheriff's Office and used to test the recovery process. The motorcycle is presented in Figures 3.8. The motorcycle's defaced VIN on the fork and engine block is presented in Figure 3.9. This specimen had the VIN completely removed on the fork (Figure 3.9a) but the VIN stamped into the engine block (Figure 3.9b) only had a few of the numbers defaced and was used to confirm the numbers recovered on the fork.



Figure 3.8: Yamaha motorcycle with defaced VIN.

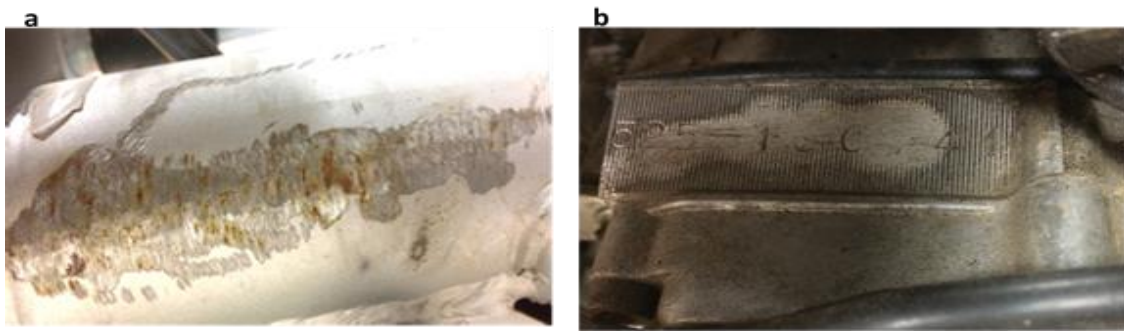


Figure 3.9: a) Defaced VIN on motorcycle fork, and b) VIN on motorcycle engine with most numbers still intact.

3.2. DATA ACQUISITION

3.2.1. Surface Preparation

The surface areas around the defaced numbers on all the acquired samples were sanded with a 600 grit sand paper to ensure a smooth surface. This is done to reduce any possible uneven distribution of thermal energy that might occur from an uneven surface which could impede the capture of the thermal gradient on the surface. The sanded surfaces were then thoroughly cleaned with ethanol to remove any extraneous material from the sanding process. The cleaned surfaces were then covered with a light coat of India ink (approximately 30 nanometers) to reduce the possible adverse effects from surface emissivity on the quality of the captured images.

3.2.2. Equipment Setup

The overall setup for the LIT studies involving directing the heating source pulsed via a pulse generator on the sample and collecting the infrared light emitted from the sample surface as it returns to equilibrium over time after the heating pulse. The experimentation system used consists of an infrared camera, a function generator and thermal energy source as shown in Figure 3.10. The primary thermal energy source, a 5W Ar-ion cw laser, operating in all-lines mode, is chopped with a Uniblitz mechanical shutter to apply pulsed energy to the samples. The laser was setup to put out 3W of thermal energy. However, losses through the top-hat filter which transforms the Gaussian shape into square-wave profile to ensure that the intensity profile of the beam is constant across surface area under observation, and the prisms account for about half of the power allowing approximately 1.5W to the sample. This power level gave a good tradeoff between inducing a temperature swing in the sample over the pulsing cycle, while avoiding overheating the sample and thus losing the ability to capture the small thermal gradients characteristic of the zone of plastic strain. A Stanford Research Systems model DS340 15MHz function generator synched with the camera is used alongside a shutter to control the pulse rate of energy from the laser, ensuring that the laser thermal energy is delivered to the sample in a sinusoidal pattern over a consistent period. A FLIR SC6700 infrared camera is used to collect thermal images of the sample surface as the pulsed thermal energy propagates through the sample. A synchronizing circuit is used to synchronize the laser pulses with the camera's imaging apparatus ensuring that a consistent rate of capturing images over an entire pulse irrespective of the cycle time/frequency used in pulsing the thermal energy could be achieved. A digital hot plate is used to heat up the samples (stainless steel plate, gun barrel and needle holder) to an initial temperature of approximately 73°C as measured by a digital thermometer. This initial heating is done to ensure that the sample is at an even initial temperature and to enhance

the contrast of the thermal gradient across the surface as recommended [14] to improve contrast. However, due to size and shape constraints, it was not possible to use this setup for the motorcycle fork and so heating tape was wrapped around the fork and used to raise the temperature of the area to approximately 70°C which proved adequate although not very even over the entire area. The temperature distribution on the heated surface is monitored using the infrared camera to collect images over the pulsing cycle.

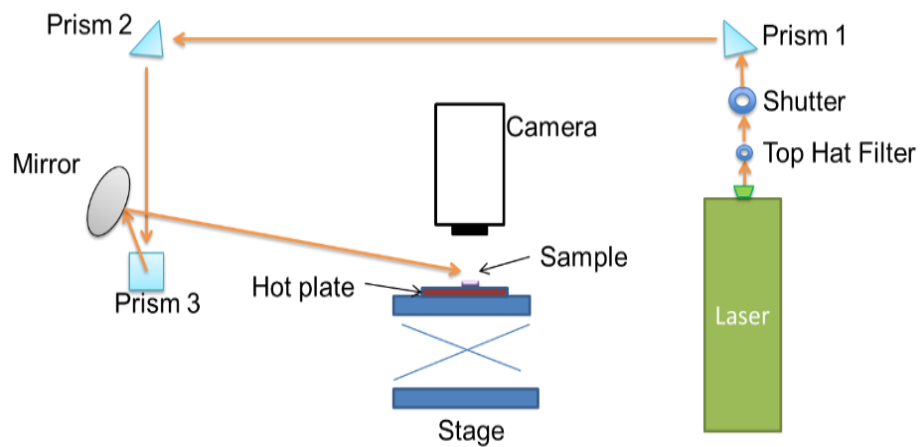


Figure 3.10: Experimental setup.

For the sample plate with holes drilled into the bottom, the sample is centered under the camera such that the field of view of the camera covers the area over all three holes at once. However for the samples with defaced numbers, the setup is adjusted with the camera field of view narrowed to capture areas over two of the removed numbers. This is done both to enhance the detail captured with more pixels per millimeter, as well as to ensure an even spread of the pulsed thermal energy from the laser beam to avoid possible lateral thermal gradients. The captured images are then digitally split to have datasets that are focused on the areas around each removed number. For the motorcycle, the initial location of the numbers was unknown and so the entire

defaced area was divided into three sections and the experimental process carried out on each independently.

During the experiments, thermal energy is pulsed into the surface of the sample under observation using the laser at a defined modulated (lock-in) frequency. Data was collected at several frequencies independently and used to generate phase difference plots as in [16,22] for each of the defaced numbers on the stainless steel plate. This was used to determine a range of modulation frequencies that could adequately characterize the change in thermal gradient within the defaced areas and as such could be used to reproduce the numbers.

3.2.3. Lock-In Infrared Thermography

The overall setup for the LIT studies involving directing the heating source pulsed via a pulse generator on the sample and collecting the infrared light emitted from the sample surface as it returns to equilibrium over time after the heating pulse is as shown in Figure 3.10. During the experiments, thermal energy is pulsed into the defaced surface under observation using the laser. The all-lines output of the laser beam is directed into a top hat filter and then through the shutter. The purpose of the top hat filter is to take the normally Gaussian intensity profile of the laser beam and convert it to square-wave profile to ensure that the intensity profile of the beam is constant across surface area under observation. Images are simultaneously collected at a rate which is selectable using the lock in thermography electronic box.

The temperature distribution on the heated surface is monitored using the infrared camera to collect images at a frame rate of 32 frames per laser pulse cycle over several laser pulse cycles to continuously capture the irregular heat propagation through the zone of plastic strain. The irregular propagation becomes more evident with the inclusion of more pulses as any noise in the thermal images associated propagation of the thermal energy is averaged out. For the

experiments with the stainless steel plates, images are collected over 15 pulse cycles and an extra cycle (making 16 cycles) is used with the other samples. Using several cycles ensures that the signal to noise ratio which is very vital for thermal images especially in conditions like that for this study where the thermal gradient differences are expected to be small is reduced.

The basic idea of this technique is that as the temperature modulation propagates from the surface into an object, it undergoes reflections at boundaries and places where the thermo-physical properties of the material are not homogenous in relation to the surrounding material. Thus it becomes phase shifted. This phase shifting can be better detected with a sinusoidal energy input. As such the function generator is used to provide a modulated sinusoidal control for the shutter and by extension the laser beam with the lock-in modulation circuit providing synchrony between the different parts ensuring the camera captures images at a consistent rate with respect to the defined cycle time for each energy pulse.

3.3. MULTIVARIATE IMAGE ANALYSIS

The image analysis section developed for this study involves employing multivariate image techniques on the set of phase or amplitude images developed for each pulsing cycle. Principal component analysis (PCA), the primary technique used, was carried out using MATLAB®.

3.3.1. Principal Component Analysis

Prior to carrying out principal component analysis on the developed phase or amplitude images, the images are filtered using a moving average filter. This is done to enhance the contrast between pixels within the defaced areas and pixels over clean areas in an image. This filtering is carried out by averaging the value of pixels in a rectangle of specified length and width (12 pixels by 12 pixels for this study) around a particular pixel and replacing its intensity value with the average. The window size for this study was chosen as it represents about half the pixel number that spans the width of a number stamp cut for the resolution used in this study. For the

edges of the images, the window is taken with the entire length and/or width of the rectangle on the inward side. This window increases as the number of pixels closest to the edge increases until the full length can be used on all sides. The filtering process was tested on the raw thermal images before developing phase and amplitude images but the resulting score images were of a lower visual quality than using the filtering on the phase and amplitude images. This is due to the filtering enhancing some of the unwanted surface features present in the thermal images that are suppressed in the phase and amplitude images. PCA is then carried out on an input matrix of filtered images in the steps outlined below.

- Each image is unfolded (row-wise or column-wise) and concatenated as a single column of a new representative matrix \mathbf{X} as shown in Figure 3.12.
- The covariance matrix \mathbf{C} is determined for the matrix.
- The eigenvectors (\mathbf{V}) and their corresponding eigenvalues ($\mathbf{\Sigma}$) are determined for the covariance matrix.
- Each eigenvector (\mathbf{v}) multiplies the representative matrix \mathbf{X} to develop a score vector which captures a percentage of the variance within the original images given in its corresponding eigenvalue.

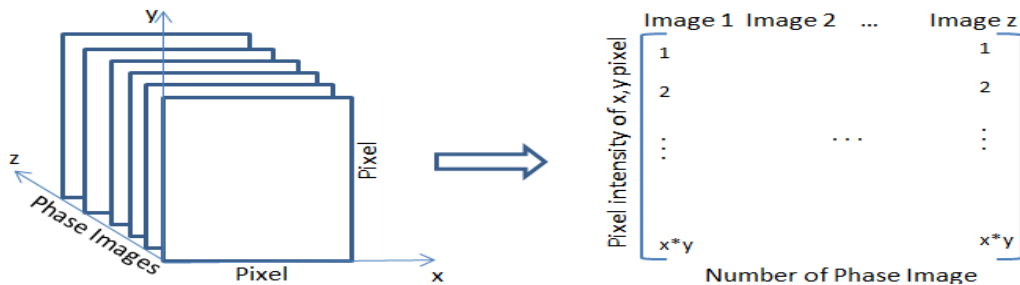


Figure 3.11: Schematic of unfolding the phase images for PCA.

- Each principal component score is then folded into a score image, to visualize the information captured as a linear combination across the images.

PCA is carried out separately on the matrix of phase images and those of amplitude images separately. These principal components account for the variability in the data in decreasing order with the first accounting for most of the variability and as such has the largest eigenvalue associated with it. PCA identifies features common across all input images and yet orthogonal to other features, grouping them into a single principal component.

As such, PCA of the amplitude and phase images from the different cycles will leverage on the anomalous heat propagation within the zone of plastic strain to capture the thermal gradient differences as an independent component of the images orthogonal to other features and isolate this variation into a single score image or a subset of score images.

After image analysis to characterize the local change in thermal gradient within the zone of plastic strain, the next stage is to identify the defaced numbers independent of human bias via the extraction of features and matching these features to those from a reference numbers library.

3.4. NUMBER IDENTIFICATION

The flowchart for the process of identification of the recovered numbers is laid out in Figure 3.12.

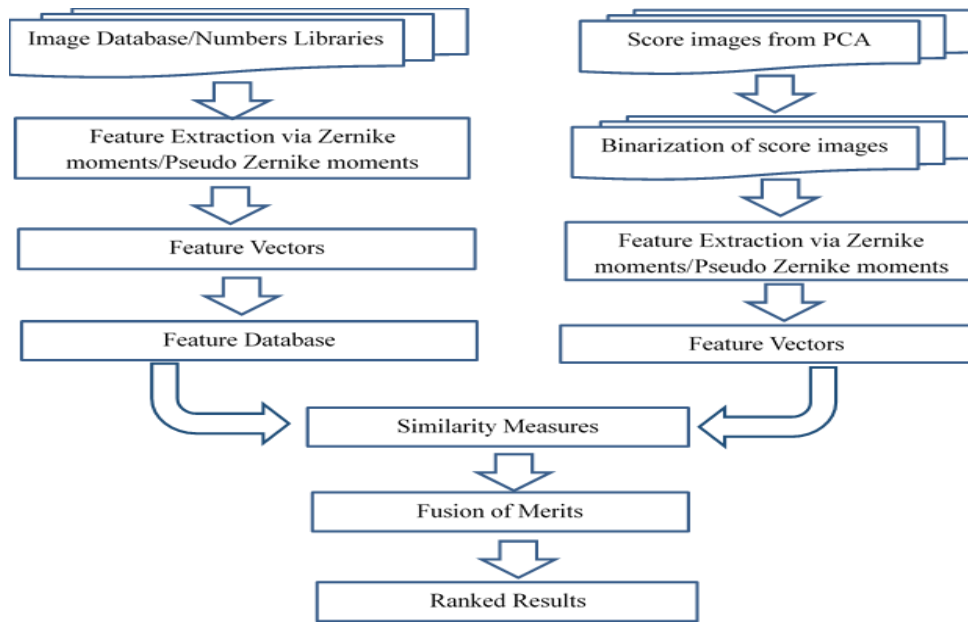


Figure 3.12: Flowchart showing procedure for identification of recovered numbers.

There are three main parts in the system. The first is an offline stage involving feature extraction from images of reference library numbers developed from Microsoft font images of numbers. It is referred to as an offline stage as these features need be extracted only once and then can be continually used to identify numbers from score images as they are retrieved from the image analysis process. The second stage is an online stage involving feature extraction from score images of areas around defaced serial numbers. Both stages lead to a third stage which involves using similarity measures to compare these features, and then fusion rules to determine a ranked result of matches for the recovered numbers across all possible 10 digits.

3.4.1. Feature Extraction

The PCA score images are initially preprocessed into binary black and white images to ensure uniformity of type with the reference library images. The binarization process requires the selection of an optimal threshold of pixel intensities to best separate background from object pixels. This threshold is selected for each individual image iteratively by using an initial assumption of the four pixel mean intensity from each corner of the image. The mean value of all

pixels in the image above this initial threshold (assumed to represent objects within the image) and those equal to or below the threshold (assumed to be represent the background) are separately calculated and then averaged together. This average value is used as a new threshold. This iterative process continues until there is no change in the determined threshold. The corresponding score image is then binarized with respect to the threshold, with 1 for above the threshold as white and 0 for below being black.

The reference library images were created by first typing out the numbers in Microsoft Word to ten different fonts used. These were then expanded so each number occupied an entire page (11.5 x 8.5 in.). The MS Word document was then converted to individual bitmap images and imported into MATLAB to create digital image libraries. Prior to extracting features, each image is preprocessed to make it scale and translation invariant. This involves normalizing the image using its regular moments as described in [58]. Scale invariance is achieved by altering the object size such that its area (pixel count for binary images) is set to a predetermined value (β). This value (β) resizes the object in the image, either increasing its size or reducing it with respect to its original area and needs to be determined empirically to ensure that the entire object still lies within the image and is large enough to be discernable. For all image objects in this study (score and numerical library pixels set to 1 by the binarization process), the β value is set to 5000 pixels. Scale invariance is achieved by Equations 3.01 and 3.02.

$$g(x, y) = f\left(\frac{x}{a}, \frac{y}{a}\right) \quad (3.01)$$

$$a = \sqrt{\frac{\beta}{m_{00}}} \quad (3.02)$$

where:

(x, y) are the pixel coordinates of each pixel in the image,

m_{00} is the area (pixel count for binary image), and

$g(x, y)$ is the invariant image pixel coordinates.

Translation involves moving the center of mass of the object in the image to the center of the image. This is achieved as shown in Equation 3.03.

$$h(x, y) = g(x + \bar{x}, y + \bar{y}) \quad (3.03)$$

where:

$h(x, y)$ is the translation invariant image pixel coordinates, and

(\bar{x}, \bar{y}) is the centroid of the object (corresponding to all pixels with intensity value of 1) in the binary image.

Two methods were evaluated for extracting feature vectors from images. These methods, based on the same underlying principles, were independently assessed to determine their suitability for this process. Both of the methods, Zernike moments and pseudo Zernike moments are moment based global shape descriptors which compute features by considering the entire image as a whole and represent the global aspects of the image.

3.4.1.1. Zernike Moments

Zernike basis functions and consequently Zernike moments are developed from these normalized images. Computing the Zernike basis function and subsequent Zernike moments for an image requires mapping the image to reside in a unit circle with the origin at the center of the image. Pixels outside a unit circle are not used in computing the moments. Thus, to ensure that all score and library image pixels are captured within the unit circle, each binary image is resized into a larger square image of dimensions calculated as shown in Equation 3.04.

$$N_x = N_y = 2(n_x^2 + n_y^2)^{1/2} \quad (3.04)$$

where:

n_x and n_y are respectively one half of the number of x and y pixels in the image, and

N_x and N_y are the new dimensions of the resized image.

Each binary image is padded on all sides with pixels of intensity 0 for black to create a new image of the larger dimensions calculated in Equation 3.04. The polar value ρ and corresponding polar angle θ for any pixel (x, y) in polar coordinates is calculated using equations 3.05 and 3.06 [52].

$$\rho = \sqrt{\left(\frac{x-\bar{x}}{d}\right)^2 + \left(\frac{y-\bar{y}}{d}\right)^2} \quad (3.05)$$

$$\theta = \tan^{-1}\left(\frac{x-\bar{x}}{y-\bar{y}}\right) \quad (3.06)$$

where:

(x, y) is the pixel coordinates of each pixel,

(\bar{x}, \bar{y}) is the pixel coordinates of the center of the image, and

d is half the dimension of the image.

Equations 3.05 and 3.06 map each pixel coordinates to the unit circle in polar. The radial polynomials ($R_{nm}(\rho)$) necessary for the determination of the Zernike basis polynomials is calculated using the polar value ρ and defined order n as shown in Equation 3.07.

$$R_{nm}(\rho) = \sum_{s=0}^{n-m/2} (-1)^s * \frac{(n-s)!}{s! \left(\frac{n+|m|}{2}-s\right)! \left(\frac{n+|m|}{2}-s\right)!} * \rho^{n-2s} \quad (3.07)$$

where:

n is a number of basis polynomials that define the order of Zernike moments, and

m is a positive or negative integer bound by the constraints $n - |m| = \text{even}$ and $|m| \leq n$.

The Zernike basis functions (polynomials) and the corresponding moments are determined from these real valued polynomials and the input images using Equations 3.08 and 3.09.

$$V_{nm}(x, y) = V_{nm}(\rho, \theta) = R_{nm}(\rho) \exp(jm\theta) \quad (3.08)$$

$$A_{nm} = \frac{n+1}{\pi} \sum_{x=1}^N \sum_{y=1}^N f(x, y) V_{nm}^*(\rho, \theta), \quad x^2 + y^2 \leq 1 \quad (3.09)$$

where:

V_{nm} is the Zernike polynomial,

A_{nm} is the Zernike moment, and

$f(x, y)$ is the intensity value of an image pixel with coordinates x, y .

The Zernike moment feature vectors are developed by concatenating the Zernike moments (A_{nm}) at each order into a single vector. An image pixel can be recreated using the Zernike basis polynomial and the Zernike moments up to a defined order as shown in Equation 3.10.

$$\hat{f}(x, y) = \sum_{n=0}^n \sum_{m=0}^n A_{nm} V_{nm}(\rho, \theta) \quad (3.10)$$

where:

$\hat{f}(x, y)$ is a reconstructed pixel in the translated (centered) representation.

The pixels added previously to ensure the original image is inscribed in a unit circle are removed leaving the reconstructed image of the same size as the original image.

The Zernike moment vectors are developed from the PCA score images as well as the reference library images using the process enunciated above. To estimate the order at which these moments will be extracted, the reconstruction error at several orders is tested by comparing the original input image to its reconstructed version from a set of Zernike moments at a specified order. The lower the reconstruction error, the better the order is at capturing the features in the image. The difference between the reconstruction errors at successive orders is computed, and the cumulative sum of these differences is determined. A plot of the cumulative sum can be used to determine a range of orders at which the reconstruction error is minimized, as there will be minimal change in the slope of the plot at those orders. A sudden increase at higher orders is indicative of instability, and do not contain pertinent detail necessary for recreating the image.

3.4.1.2. *Pseudo Zernike Moments*

A similar process is used to determine the pseudo Zernike moments for each image. The only difference lies in the determination of the real valued polynomial with removal of the constraint of keeping the difference in an order and its repetitions even. This leads to a redefinition of the basis polynomials as shown in Equation 3.11 [58].

$$R_{nm}(\rho) = \sum_{s=0}^{n-m} (-1)^s * \frac{(2n+1-s)!}{s!(n-|m|-s)!(n+|m|+1-s)!} * \rho^{n-s} \quad (3.11)$$

where:

$n - |m|$ is only subject to the constraint $|m| \leq n$

Several orders of moments are used in both methods to ensure that both the gross details of the images and the finer details captured in lower and higher order moments respectively are utilized in identifying the images. The orders selected were 15 through 50 in steps of 5 for Zernike moments and 4 through 20 in steps of 2 for pseudo Zernike moments.

3.4.2. Similarity Measures

Several similarity measures are used in this study to compare the Zernike moments of the score images to those for 10 datasets (libraries) made up of unaltered numbers. These number libraries were developed by converting MS Word number characters into digital images of numbers for 10 different Microsoft fonts namely Times New Roman, Times New Roman italics, Tempus Sans, Segoe Print, Gung Suh, Gung Suh italics, Arial Rounded MT, Arial Rounded MT italics, Arial Black, and Arial Black italics. Figure 3.13 shows an example of the numbers for the Times New Roman font. Images for the other fonts used can be found in the Appendix.



Figure 3.13: Digital images created to use in identifying recovered numbers.

Several comparisons are made between feature vectors from the reference library and score images, using each similarity measure, at each selected order of basis polynomials. In detailing the similarity measures and how they are used in this section, the nomenclature \mathbf{x}_l and \mathbf{x}_s are used in the mathematical formulations to describe feature vectors from reference library images and score images respectively.

A total of 15 similarity measures are used in this project to compare respective feature vectors, each designed to define a perfect match between the two vectors as zero and increasing in value with a decrease in similarity. Some of the similarity measures used require matrices for comparison. For these measures, the outer products of both sets of feature vectors was determined as shown in Equations 3.12 and 3.13 and used for comparison.

$$\mathbf{X}_1 = \mathbf{x}_1 \mathbf{x}_1^T \quad (3.12)$$

$$\mathbf{X}_s = \mathbf{x}_s \mathbf{x}_s^T \quad (3.13)$$

Also, some of the measures require the calculation of singular value decompositions (SVD) as shown in Equation 3.14.

$$\mathbf{X} = \mathbf{U} \mathbf{\Sigma} \mathbf{V}^T \quad (3.14)$$

where:

\mathbf{X} is a generic input matrix (the outer product of one of the feature vectors in this study),

\mathbf{U} and \mathbf{V} are the eigenvectors of the matrix \mathbf{X} , and

$\mathbf{\Sigma}$ is the diagonal matrix of singular values.

A summary of the mathematical equations for the measures used is shown in Table 3.1 and a description given below.

Table 3.1: Similarity measures used.

Similarity Measure ^a	Equation ^b
Correlation Coefficient (2)	$CC = \frac{S_{I_s}}{S_I S_s}$
Euclidean Distance (2)	$ED = \sqrt{(\mathbf{x}_I - \mathbf{x}_s)(\mathbf{x}_I - \mathbf{x}_s)^T}$
Angle (2)	$\cos \theta = 1 - \frac{ \mathbf{x}_I^T \mathbf{x}_s }{\ \mathbf{x}_I\ \ \mathbf{x}_s\ }$
Determinant (1)	$Det = \left \begin{pmatrix} \mathbf{x}_I^T \\ \mathbf{x}_s^T \end{pmatrix} (\mathbf{x}_I \ \mathbf{x}_s) \right = (\ \mathbf{x}_I\ \ \mathbf{x}_s\ \sin \theta)^2$
Procrustes Analysis (PA) (4)	$F = \ \mathbf{F}_{sI} - \mathbf{F}_{ss}\ _F$
Constrained PA (2)	$H = \ \mathbf{H}_{sI} - \mathbf{H}_{ss}\ _F$
Mahalanobis Distance (2)	$MD = \sqrt{(\mathbf{x}_s - \mathbf{x}_I)^T \mathbf{C}_s^+ (\mathbf{x}_s - \mathbf{x}_I)}$

^a Values in parenthesis indicate the number of variations.

^b See respective descriptions for definitions of equations.

\mathbf{x}_I = feature vector of reference library image

\mathbf{x}_s = feature vector of score image

i. Correlation Coefficient:

a. Pearson Correlation

This is a measure of the linear relationship between two vectors. A perfect value of 1 means that both vectors have a perfect correlation between them and 0 means there is no correlation between them. In keeping with the convention adopted for this study, the correlation coefficient is subtracted from 1 so that a smaller value will indicate a higher correlation between the vectors.

$$CC = 1 - \frac{S_{1s}}{S_1 S_s} = 1 - \frac{\sum_{i=1}^n (x_{si} - \bar{x}_s)(x_{1i} - \bar{x}_1)}{\sqrt{\sum_{i=1}^n (x_{si} - \bar{x}_s)^2} \sqrt{\sum_{i=1}^n (x_{1i} - \bar{x}_1)^2}} \quad (3.15)$$

b. Spearman Correlation Coefficient

For the Spearman correlation, the values within each vector are first ranked before the correlation is calculated as above.

ii. **Euclidean Distance:**

a. Vector to vector Euclidean distance

The Euclidean distance is a measure of the distance in space between two vectors. This is determined as the square root of the square of the difference between corresponding points in both vectors being compared. The smaller the value of the resulting merit, the higher the degree of similarity between them.

$$ED = \sqrt{(\mathbf{x}_1 - \mathbf{x}_s)(\mathbf{x}_1 - \mathbf{x}_s)^T} \quad (3.16)$$

b. Vector Outer Product Euclidean Distance

This is similar to Euclidean distance except the outer vector products are used for the comparison ($\mathbf{X}_1 = \mathbf{x}_1 \mathbf{x}_1^T$ and $\mathbf{X}_s = \mathbf{x}_s \mathbf{x}_s^T$). The outer products are unfolded to form a vector and Equation 3.16 is used.

iii. **Angle between vectors:**

This similarity measure is determined as the cosine of the angle between two vectors for a shape comparison. The value is subtracted from 1 for a smaller value indicating a higher degree of similarity between vectors.

$$\cos \theta = 1 - \frac{|\mathbf{x}_1^T \mathbf{x}_s|}{\|\mathbf{x}_1\| \|\mathbf{x}_s\|} \quad (3.17)$$

iv. **Square of the angle:**

This measure involves taking the square of the value for the angle between the vectors and then subtracting from 1 for a smaller value for a higher degree of similarity.

v. Determinant:

This similarity measure is a measure of the space size formed by two vectors and calculated by Equation 3.18. The smaller the resulting value, the smaller space and hence, the more similar the vectors.

$$\text{Det} = \left| \begin{pmatrix} \mathbf{x}_1^T \\ \mathbf{x}_s^T \end{pmatrix} (\mathbf{x}_1 \quad \mathbf{x}_s) \right| = (\|\mathbf{x}_1\| \|\mathbf{x}_s\| \sin\theta)^2 \quad (3.18)$$

vi. Unconstrained Procrustes Analysis:

This measure is a transformation process that as used in this study, determines how much transformation is required to make the matrix formed by one outer vector product similar to another outer vector product. Transformation occurs in the form of rotation, dilation, and translation of each vector to make them match. A Frobenius norm (F) of the matrix difference between the transformation matrices for the two vectors is used as a final measure of the similarity between them. This value represents the matrix from the difference between the transformation matrices as a scalar with a smaller value indicating a higher degree of similarity.

$$\mathbf{X}_1 = \mathbf{X}_s \mathbf{F}_{s1} \quad (3.19)$$

$$\mathbf{F}_{s1} = \mathbf{X}_s^+ \mathbf{X}_1 \quad (3.20)$$

$$\mathbf{X}_s^+ = \frac{\mathbf{X}_s}{\|\mathbf{x}_s\|^4} \quad (3.21)$$

$$\mathbf{F}_{ss} = \mathbf{X}_s^+ \mathbf{X}_s \quad (3.22)$$

$$\mathbf{F} = \|\mathbf{F}_{s1} - \mathbf{F}_{ss}\|_F \quad (3.23)$$

where:

\mathbf{F} is a transformation matrix necessary to make \mathbf{x}_s most similar to \mathbf{x}_1

$\|\mathbf{F}_{s1} - \mathbf{F}_{ss}\|_F$ is the Frobenius norm for the matrix difference between the two transformation matrices \mathbf{F}_{s1} and \mathbf{F}_{ss} calculated as the square root of the sum of squares of each value in the difference matrix.

Four similarity merits are obtained using Procrustes analysis in this study. Two by using the mean centered outer products of each of the vectors (\mathbf{X}_1 and \mathbf{X}_s) being compared to define the transformation matrix and another two by not mean centering the outer product matrices before determining the transformation matrices. With mean centering, translation correction is included and without mean centering, only rotation and dilation are evaluated.

vii. Constrained Procrustes Analysis

This transformation measure defines individually the degrees of dilation and rotation required after translation to make the two vectors similar. As with unconstrained Procrustes analysis, the Frobenius norm is used to determine a final scalar similarity merit, a smaller value indicating a higher degree of similarity.

$$\mathbf{X}_{s1} = \mathbf{X}_s^T \mathbf{X}_1 = \mathbf{U}_{s1} \Sigma_{s1} \mathbf{V}_{s1}^T \quad (3.24)$$

$$\mathbf{H}_{s1} = \mathbf{u}_{s1} \mathbf{v}_{s1}^T \quad (3.25)$$

$$\mathbf{X}_{ss} = \mathbf{X}_s^T \mathbf{X}_s = \mathbf{U}_{ss} \Sigma_{ss} \mathbf{V}_{ss}^T \quad (3.26)$$

$$\mathbf{H}_{ss} = \mathbf{u}_{ss} \mathbf{v}_{ss}^T \quad (3.27)$$

$$H = \|\mathbf{H}_{s1} - \mathbf{H}_{ss}\|_F \quad (3.28)$$

where:

\mathbf{U} = eigenvectors of matrix $\mathbf{X}\mathbf{X}^T$

\mathbf{u} = first eigenvector in \mathbf{U}

Σ = diagonal matrix of singular values

\mathbf{V} = loading matrix = eigenvectors of matrix $\mathbf{X}^T\mathbf{X}$

\mathbf{v} = first eigenvector in \mathbf{V}

Two possible sets of similarity merits are obtained, with one set involving mean centered outer product arrays (translation is included) and the other set without mean centering (only rotation and dilation).

viii. Mahalanobis Distance:

This is a distance measure that determines the distance of a vector from a space formed by an array of vectors. To use this measure as a distance measure between two vectors, the pseudoinverse of the outer product of one of the vectors is taken as the usual covariance matrix used in the Mahalanobis distance estimation. A smaller merit value in this measure indicates a smaller distance in space, and hence a higher degree of similarity between the vectors.

$$MD = \sqrt{(\mathbf{x}_s - \mathbf{x}_l)^T \mathbf{X}_s^+ (\mathbf{x}_s - \mathbf{x}_l)} \quad (3.29)$$

A second similarity merit is obtained using the Mahalanobis distance measure defined in Equation 3.29 by exchanging the outer vector product matrix \mathbf{X}_s for \mathbf{X}_l .

All score images developed for a defaced number are evaluated irrespective of whether or not a recovered number can visually be recognized in it. Using all score images avoids the necessity of preselecting score images to compare and ensures that parts of a defaced number that may be partially reproduced in a range of score images are utilized in making the identification. Resulting from this are similarity values for each iteration of the process. These values need to be combined together to form a consensus as to the classification of the recovered number from the 10 possible classes, one for each digit. Data fusion is a beneficial way of computing the

consensus, as the different formulations take advantage of the data characteristics to extract a common consent value representative of the dataset.

3.4.3. Data Fusion

With each score image being compared to each digit across 10 numeric libraries using 15 similarity measures, there is a need to determine a consensus across the resulting similarity measures obtained. To achieve consensus, a high level data fusion approach is applied. Multiple fusion rules are also used where each rule is applied to extract a consensus value from all similarity values relative to each number identification possibility. These rules are sum, geometric mean, harmonic mean, median, L2 norm, L1 norm, truncated geometric mean, and truncated harmonic mean. Most rules are applied twice, once to raw values and another time to rank values except the truncated rules which are only applied to the raw values. The mathematical formulations of the rules are given in Table 3.2.

A matrix of all the similarity values obtained is first assembled, each row corresponding to similarity values comparing the feature vector of a score image at a particular order (15 through 50 in steps of 5 for Zernike moments and 4 through 20 in steps of 2 for pseudo Zernike moments) to a particular font in the reference library using a similarity measure. Each row of this matrix is normalized to unit length to remove any possible effects of magnitude of similarity merits on the final fusion results.

The matrix of similarity values obtained using Zernike moment feature vectors is used in obtaining a consensus from the fusion process. Each fusion rule is applied to the columns of this matrix as well as to the matrix after transformation to rank values. The smaller the fusion rule value for a particular column, the more similar the defaced number is to the corresponding target library number. By using both normalized raw and rank values, there are 14 fusion rules.

However, for the matrix of similarity merits obtained using the pseudo Zernike moments feature vectors, a thresholding operation is initially performed. First, only rows having the ratio of the two lowest similarity values equal to a defined threshold are selected and the fusion process is applied to this matrix. This process is repeated for successively increasing values of the threshold (between 0.1 and 1 in steps of 0.05 for this study). The resulting fusion values for all the thresholds set are then concatenated into a single 10 column matrix and the fusion rules applied again. This thresholding was carried out to help improve the consistency in identification across all the different fusion rules used and thus reduce inaccuracies.

Table 3.2: Fusion rule notation for figures.

Rule	Normalized raw values notation	Rank values notation	Equations
Sum	S	SR	$\sum_{i=1}^n S_i$
Median	M	MR	$\text{med}\{S_1 \dots S_n\}$
L-2 norm	L2	L2R	$\sqrt{\sum_{i=1}^n S_i^2}$
L-1 norm	L1	L1R	$\sum_{i=1}^n S_i $
Geometric mean	GM	GMR	$\sqrt[n]{S_1 * S_2 * \dots * S_n}$
Truncated Geometric mean	TrGM	-	
Harmonic mean	HM	HMR	$\left(\frac{1}{n} \sum_{i=1}^n S_i^{-1}\right)^{-1}$
Truncated Harmonic mean	TrHM	-	

S_i = the similarity value for the i th measurement (the value form a similarity measure for a particular score image to a particular number and font in the reference library at a particular order)

The truncated rules, TrGM and TrHM, are only used on the raw normalized values and utilize a defined percentage of the lowest values (75% in this study) to determine the geometric mean and harmonic mean respectively instead of all the values.

The defaced number is matched to the target number that is most consistently (eight of the fourteen rules i.e. majority vote) ranked lowest across the fusion rules and whose sum across the ranked fusion rules is lowest.

3.5. CONFORMAL PREDICTION

To determine the confidence levels to be placed on classifications using conformal prediction, it is necessary to define nonconformity measures to analyze the results obtained from the classification process. These nonconformity measures will essentially appraise how different (nonconforming) each value in a class to which an unknown sample is categorized into, is from the other values within the class. This difference is compared to the value's difference from the values in all other classes and a percentage confidence level is calculated for the fit. A class is defined for this study as a single number digit, resulting in 10 possible classes (0-9). The values in each class are all the fusion values computed for the similarity merits comparing the score images to all reference library images of the particular number digit. Several nonconformity measures have been proposed in literature for different types of data and analyses. Two of these measures which have proven quite robust for classification are employed in this study. These are the nearest neighbor and distance to average methods.

3.5.1. Nearest Neighbor Procedure

This involves measuring the 'nonconformity' of each fusion rule value by comparing its distance from other fusion values within the same class to its distance from fusion values in other classes. The following steps are used to determine a confidence index using the nearest neighbor procedure.

- The 8 raw fusion values (sum, median, geometric mean, harmonic mean, L2 norm, L1 norm, truncated geometric mean, and truncated harmonic mean) in each class (0-9) are row concatenated into an 8 x10 matrix.
- Each fusion value from within the class the defaced number is identified to belong in from the identification scheme, is reassigned to one of the nine classes (0-9) as an unknown sample.
- The nearest neighbor algorithm as shown in Equation 3.30 is used to determine nonconformity scores for each of the fusion values in the class including the newly assigned unknown.

$$\alpha_i = \frac{\min\{|x_j - x_i| : 0 \leq j \leq 9 \ \& \ j \neq i \ \& \ y_j = y_i\}}{\min\{|x_j - x_i| : 0 \leq j \leq 9 \ \& \ j \neq i \ \& \ y_j \neq y_i\}}$$

$$= \frac{\text{distance of value } x_i \text{ to others in its class}}{\text{distance of value } x_i \text{ to values in a different class}} \quad (3.30)$$

- The p-value which delineates the suitability of the unknown sample to the class is determined by computing the percentage of the class members with nonconformity scores greater than the nonconformity score of the unknown sample.

$$p_y = \frac{\#\{i=1, \dots, n \mid \alpha_i \geq \alpha_n\}}{n} \quad (3.31)$$

where:

x_i is the sample (fusion value) being tested for non-conformity to a class,

y_i is the class label for sample x_i ,

x_j is a sample (fusion value) different from that under consideration,

y_j is the class label of class j ,

α_i is the nonconformity score of each sample (fusion rule value) x_i in class j .

n is the number of samples in a class including the unknown sample,

α_n is the nonconformity score of unknown sample.

- This is repeated with each fusion value in the class the score images were classified into, tested across all available classes.
- The average of the p-values for each class is used as a representative p-value defining the conformity of the unknown value to a class.
- The highest resulting p-value indicates the class to which fusion values are a best match for. This value is used as a measure of the credibility of the nonconformity measure used. The confidence level for this identification is determined by subtracting the second highest p-value from one.
- Ideally, the second highest p-value should be close to zero indicating that the fusion rules do not fit into any other class but the one they were originally grouped into in the identification process.

3.5.2. Distance to Average Procedure

This measure utilizes the difference in the distance of a value to the average value of a class to define a confidence level for the classification. The nonconformity score is defined for each fusion value (unknown sample), within the predicted class of the score images in the identification scheme, as the distance of the value to the class average of fusion values in each of the nine classes. It is determined as shown in Equation 3.32.

$$\alpha_i = X_{av} - x_i \quad (3.32)$$

where:

α_i is nonconformity score of each sample (fusion rule value) x_i in class i

X_{av} = average of each class after assigning fusion value to the class.

The determination of the p-value and subsequently the confidence index using the distance to average as the nonconformity measure is similar to the procedure used for the nearest neighbor method.

The methodology outlined in this chapter was applied to all the acquired samples to develop and test a holistic non-destructive process for recovering defaced serial numbers.

CHAPTER 4

4.0. DATA COLLECTION AND IMAGE ANALYSIS

Several steps within the methodology are devoted to developing a process to collect thermal images that capture the unique thermal gradient in defaced areas and enhance the images to aid the recovery of defaced serial numbers. The results from these processes are detailed below, including a finite element analysis of the research problem initially carried out to determine the viability of the proposed procedure.

4.1. FINITE ELEMENT MODELING

The finite element (FE) method is a numerical technique for finding approximate solutions to partial differential equations (PDE) and their systems. In this study, it was used to simulate the plastic deformation occurring in the atomic structure of a metal plate due to the force of stamping and its effect on the thermal conductivity of the distorted region. The general purpose program ANSYS is used to carry out the ensuing analysis. Carrying out a finite element analysis in ANSYS involves several steps including modeling the system under investigation, meshing it, applying loads and appropriate boundary conditions and solving.

The finite element model designed for this study assumed three dimensional heat transfer conditions within a homogenous stainless steel plate. The thermal and geometric parameters were defined for this model to emulate those of stainless steel (AISI 304). Boundary conditions were defined to include heat transfer by conduction.

The finite element model developed is shown in Figure 4.1. This is a 6mm thick stainless steel plate with a static force applied to simulate stamping pressures used to impress a number. Figure 4.2 shows the plastic strain distribution around the number stamped into a plate. This strain is resultant from the distorted crystalline structure of the material due to the force of stamping and is concentrated around the area of the stamped number.

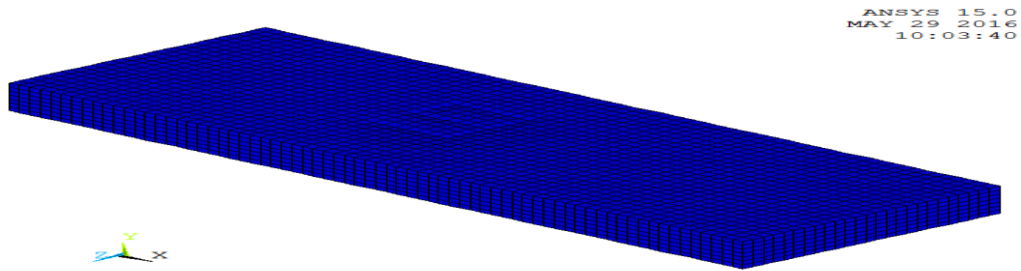


Figure 4.1: Meshed FE model with stamped number.

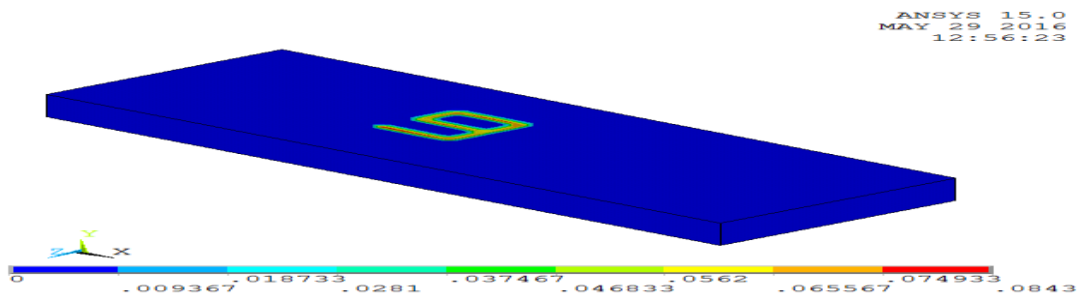


Figure 4.2: Plastic strain distribution on surface of FE model.

Figure 4.3 shows the plastic strain distribution on the plate after 3 mm of material was removed from the surface, replicating the defacing of serial numbers process. The plastic strain at this depth is more widely distributed and the number can no longer be uniquely identified at room temperature.

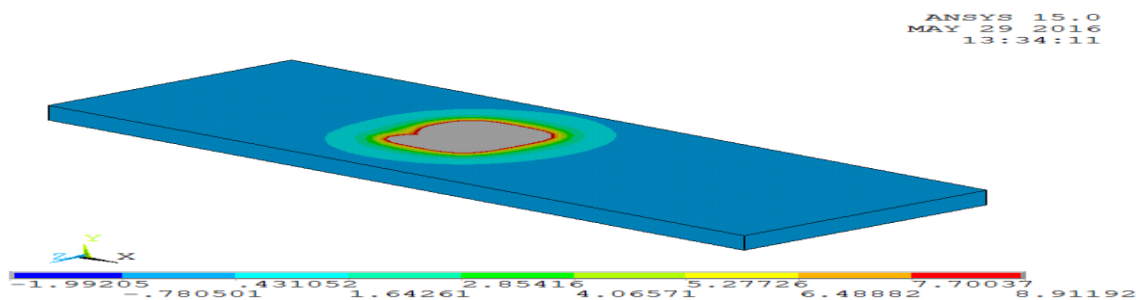


Figure 4.3: Plastic strain distribution on surface after removing material.

Figure 4.4 shows the plastic strain distribution after the application of a heat flux to the surface. The thermal conductivity is uneven across the surface due to the plastic strain around the

removed number, leading to uneven conduction of heat. This leads to the development of hot spots (with higher temperatures) at areas where with reduced thermal conductivity, allowing for identification of the number that was removed from the region. This corroborates the posited material behavior under thermal energy.

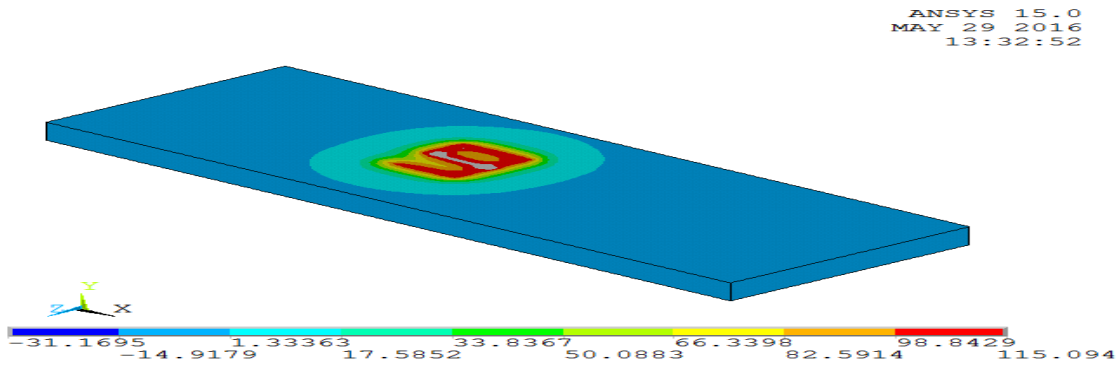


Figure 4.4: Plastic strain distribution after applying thermal energy to surface.

4.2. STAINLESS STEEL PLATE WITH HOLES

A lock-in frequency of 0.125 Hz was used in pulsing the thermal energy through the sample to visualize the subsurface holes from the surface of the plate. Figure 4.5 shows the average of 32 infrared thermal images, captured over a single pulsing cycle of thermal energy into the surface of the stainless steel plate. From this image it is impossible to identify the thermal gradient differences characteristic of the areas above the subsurface holes, highlighting the necessity of further processing the thermal images.

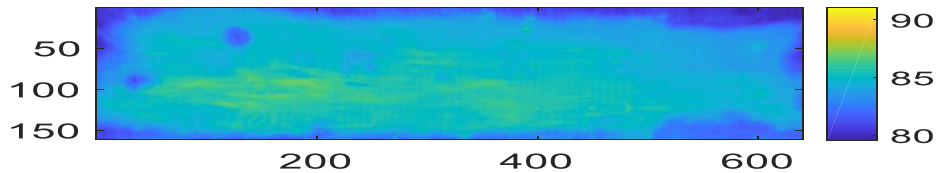


Figure 4.5: Raw thermal image of stainless steel plate with holes drilled in (axes represent the pixel coordinates and the color bar shows the temperature range ($^{\circ}\text{C}$) of the sample).

Figure 4.6 shows a phase image developed from the 32 infrared thermal images captured over one lock-in pulsing cycle. White boxes indicate the areas over the underlying holes in the sample. This phase image clearly identifies the defect (hole) closest to the surface. As the hole increases in surface distance (left to right), the outline clarity reduces.

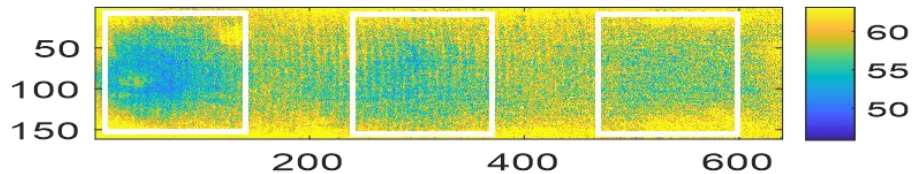


Figure 4.6: Phase image of drilled sample (axes represent the pixel coordinates and the color bar shows the degree of phase shift).

Figure 4.7 shows the PC score image (PC1) developed from the 15 phase images. This score image explains 99.8% of the variance across the phase images and best captured the contrast between the areas over the holes and the background areas. The score image can be seen to have improved the visibility of the deeper subsurface holes (blue in white boxes) making them more identifiable. This helps to validate the capacity of PCA to better distinguish the thermal gradient differences from the zone of plastic strain in a sample under observation.

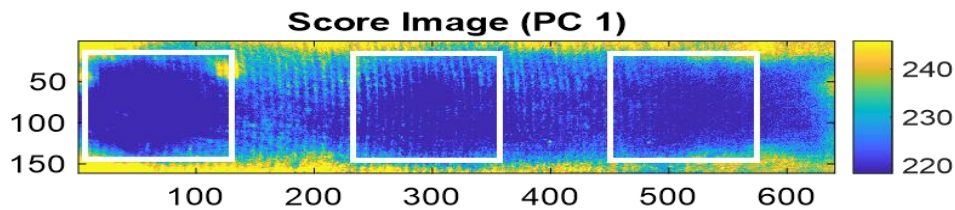


Figure 4.7: Score Image of drilled sample after PCA (Axes represent the pixel coordinates and the color bar shows the range of score values).

4.3. STAINLESS STEEL PLATE WITH NUMBERS

Figure 4.8 shows the defaced stainless steel plates with the stamped in number removed. The area around each of the defaced numbers are identified by white boxes in the image. These areas were isolated and individually analyzed to recover the numbers.



Figure 4.8: Stainless steel sample with numbers defaced (boxes show areas extracted and individually analyzed for each number).

A lock-in frequency of 0.05 Hz was selected to be used in pulsing the thermal energy through the sample. This lock-in frequency was selected using phase difference plots developed for differences in the phase in areas previously stamped with numbers and average phase values of clean unstamped areas for various lock-in modulation frequencies. Figure 4.9 shows the phase difference plots for the measured defaced areas as well as a simulated phase difference plot created using the model developed by [24] and discussed in Chapter 2. This simulated plot was made using the numerical model of a multilayer sample to predict the phase values at different modulation frequencies, using parameters for a stainless steel specimen. Some of the parameters were selected to simulate the conditions of the stamped stainless steel plate and are shown in Table 4.1.

Table 4.1: Parameters used for simulated plot

Parameters	Layers		
	Paint ¹	Defaced layer	Clean layer
Thermal conductivity (W/m K)	1.38	10	16.2
Specific heat capacity (J/Kg ^K)	5184	502.42	502.42
Thickness (m)	3.0E-10	8.70E-04	5.30E-03

¹The parameters for the paint layer are obtained from [92]

These plots show that a similar trend in both the simulated model and actual sample, with a consistent increase in the phase difference between 0.125Hz and 0.0156Hz, suggesting that shorter modulation frequencies better delineate this difference in phase between defaced and sound areas.

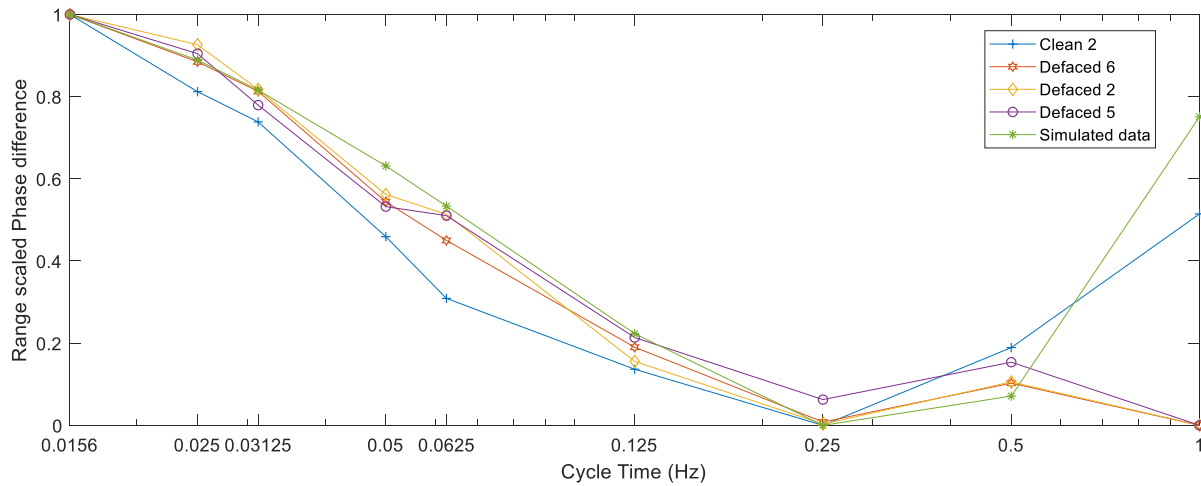


Figure 4.9: Phase difference plots for each defaced number on stainless steel sample.

Images are simultaneously collected at a frame rate of 32 frames per pulse cycle. This process is carried out for several cycles. If the heat propagates irregularly through the plastic deformation areas below the stamped or engraved numbers, whereas propagation of the heat through non-deformed areas is more uniform, the amplitude and phase images should capture this phenomenon. The white noise in the thermal images associated with the regular propagation is essentially averaged out by including more pulses, and 15 pulse cycles were used for this experiment. PCA on these amplitude and phase images should capture this local variation and reproduce it into a single score image orthogonal to other variations in the images. Figure 4.10 is a mean temperature-time plot across all pixels of the defaced area showing the pulsing of thermal energy through the sample over time. The values over each peak show the maximum temperature value in that cycle. Control of the heating is difficult and slight variations in the maximum temperature over the course of the 15 cycles is a typical occurrence.

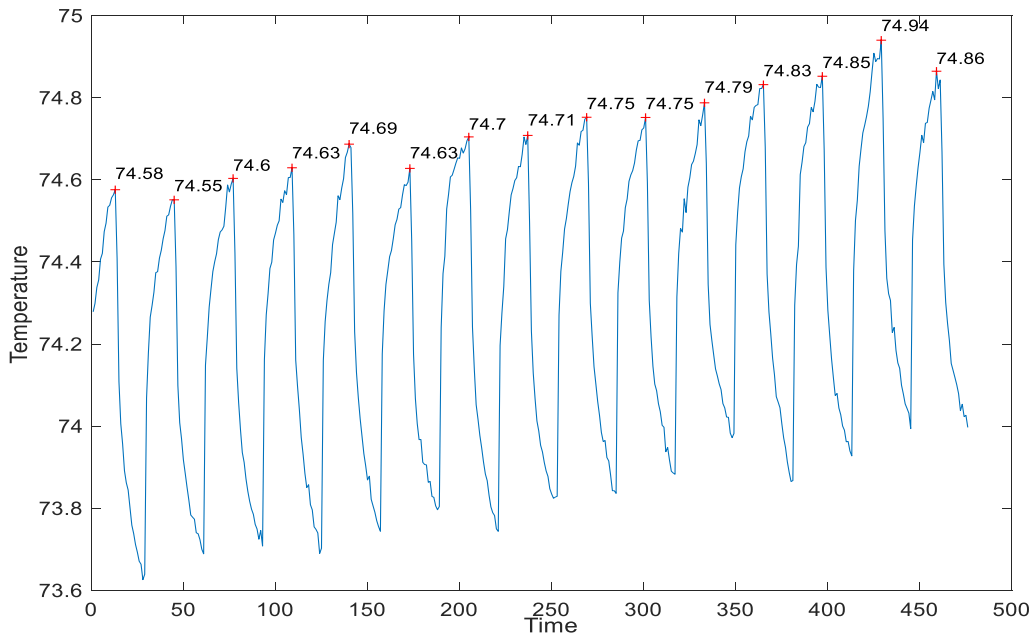


Figure 4.10: Mean temperature-time plot across the defaced 6 surface.

Figure 4.11 shows the mean infrared thermal image for one pulse cycle (modulation frequency of 0.05Hz) of a clean stainless steel surface left intact with no number stamped into it. The image is comparable to those shown in Figure 4.12 for the areas around the defaced numbers (the boxed in areas in Figure 4.08). As with the sample at room temperature, the numbers removed cannot be uniquely distinguished from a clean surface in the infrared thermal images.

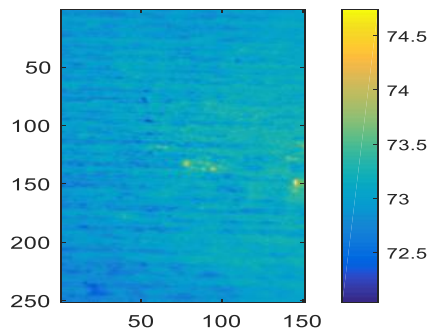


Figure 4.11: Raw thermal image of a clean surface (axes represent the pixel coordinates and the color bar shows the temperature range (°C) of the sample).

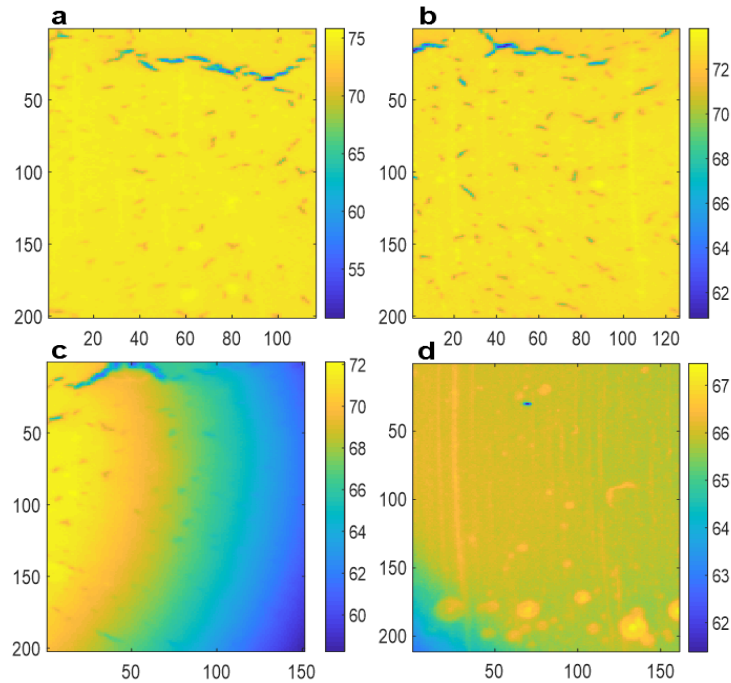


Figure 4.12: Raw thermal images of areas around defaced numbers a) Six b) Two c) Five d) Zero (axes represent the pixel coordinates and color bars show the temperature range ($^{\circ}\text{C}$) of the sample).

The input images for the area around the defaced 0 were further preprocessed using standard normal variate [93] to remove some light scatter effects that were observed on visual inspection of the input images. This was not done for the images for the other defaced numbers as there was no observed scatter in their input images. Each pulse cycle is used to develop one amplitude and one phase image in which the contrast change across the surface due to the thermal gradient change from the defects is improved. Fifteen of these images are developed, one from each pulse cycle from the input energy pulse. PCA is carried out independently on the matrix of the phase images and that of the amplitude images. Figures 4.13 and 4.14 show phase images over a single pulse cycle for the clean region and defaced numbers respectively. Although the phase images have effectively removed such unwanted features such as inhomogeneous illumination as well as surface radiation and local emissivity variations from the images, it is still impossible to identify the serial numbers in Figure 4.14.

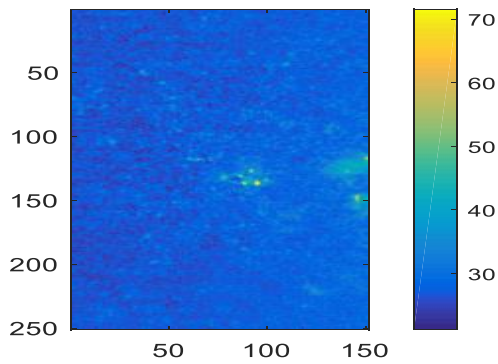


Figure 4. 13: Phase image of a clean surface (axes represent the pixel coordinates and the color bar shows the degree of phase shift).

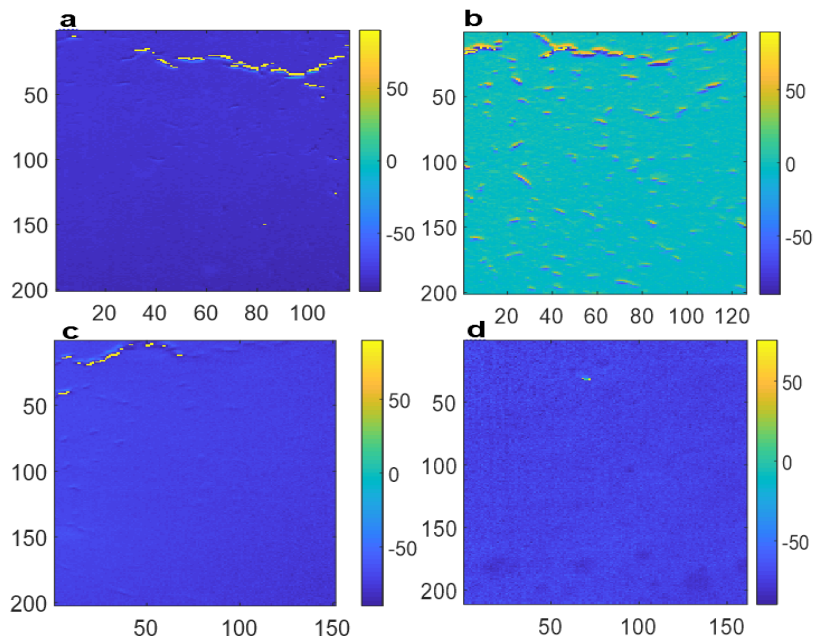


Figure 4. 14: Phase images of areas around defaced numbers a) Six b) Two c) Five d) Zero (axes represent the pixel coordinates and the color bar shows the degree of phase shift).

Respective score images are visually inspected to determine if phase or amplitude score images best captured the variation in thermal gradient indicative of the defaced number. This proved to be the amplitude images for the defaced 6, 2 and 0 and the phase images for the defaced 5. PCA was tested using both phase and amplitude images but the resulting score images were not as clearly defined as those reported here of carrying out PCA on each set separately.

Table 4.2 shows the percent variance of information explained in each PC. As by convention, PC1 explains the most amount of variance and the other PC's explain some of the remaining variance present in decreasing order. The shaded cells indicate the PC where the defaced number was best reproduced for each dataset.

Table 4.2: Percentage of Variance in each PC for defaced numbers on stainless steel sample (shaded boxes represent the PC where the respective numbers where best reproduced).

PC	Percent Variance (%)				
	<i>Clean area</i>	<i>Six</i>	<i>Two</i>	<i>Five</i>	<i>Zero</i>
1	99.0328	98.5497	82.2910	99.8550	48.6725
2	0.5639	1.0724	16.8583	0.0820	8.9673
3	0.2580	0.2219	0.7022	0.0375	5.5631
4	0.1152	0.0993	0.0624	0.0125	5.4441
5	0.0108	0.0312	0.0283	0.0060	4.7530
6	0.0064	0.0142	0.0162	0.0017	4.4526
7	0.0027	0.0052	0.0127	0.0013	3.7963
8	0.0023	0.0027	0.0074	0.0010	3.6741
9	0.0019	0.0010	0.0055	0.0008	3.2420
10	0.0014	0.0009	0.0046	0.0006	2.8108
11	0.0012	0.0006	0.0034	0.0004	2.5601
12	0.0009	0.0004	0.0029	0.0004	2.2362
13	0.0008	0.0003	0.0021	0.0003	1.9693
14	0.0007	0.0002	0.0016	0.0002	1.1534
15	0.0006	0.0002	0.0016	0.0002	0.7053

Figure 4.15 presents the score images from the clean undefaced region. PC1 is responsible for 99% of the variance within the images. PC 2 through PC 15 is responsible for the remaining 1% of the variance. The score images show no identifiable structure although with some random high intensity areas due to surface roughness of the sample. This is expected, as no crystalline deformation exists within the sample in this region.

Figure 4.16 shows the score images from the amplitude images of the area around the number “6”. The first principal component PC1 is responsible for 98% of the variance and PC 2 through

PC 15 for the remaining 2%. However, unlike for the clean area, one of the score images (PC13) shows defined intensity contrast localized around the section where the number previously existed. This PC accounts for only 0.0003% of the variance across the amplitude images. This can be attributed to how relatively small the phase shift due to thermal gradient differences in the zone of plastic strain is compared to other sample features within the thermal depth range, highlighting, the robustness of PCA in recognizing and characterizing such small variances across the pixels.

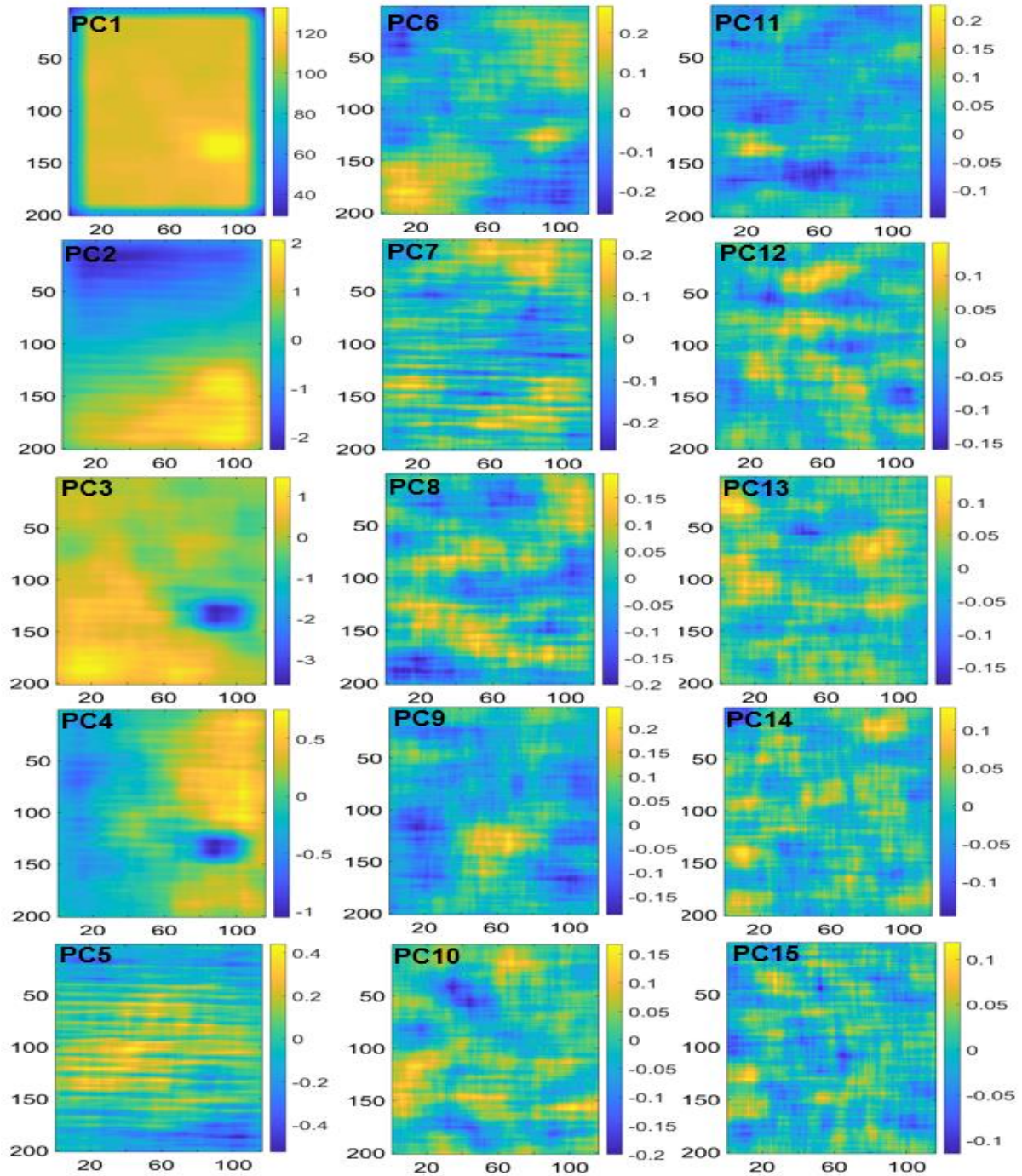


Figure 4.15: Score images for clean surface (Axes represent the pixel coordinates and the color bar shows the range of score values).

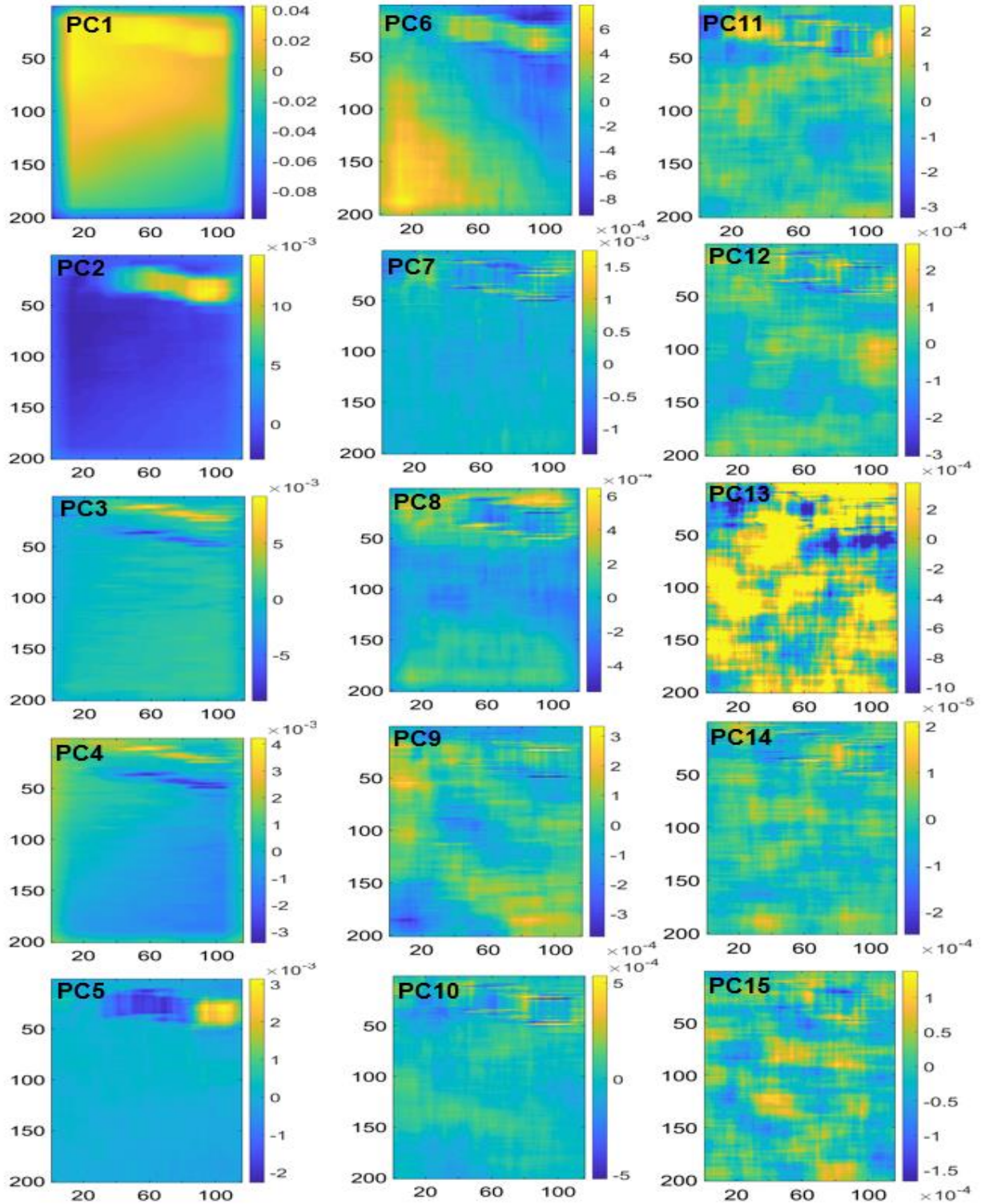


Figure 4.16: Score images for area around defaced number six (Axes represent the pixel coordinates and the color bar shows the range of score values).

Figure 4.17 similarly shows the refolded score images (contrast adjusted) from principal component analysis of the regions around the numbers “2”, “5” and “0”. PC 11 presented in Figure 4.17a shows some contrast in the region where the number existed. This PC accounts for only 0.003% of the variance. Likewise, for the defaced 5, PC 10 shown in Figure 4.17b shows some contrast in intensity allowing for possible identification of the number that was defaced.

PC 1 accounting for 49% of the variance shows intensity contrast to possibly identify the number 0 that was defaced. This can be seen in Figure 4.17c. The relatively larger value in the variance accounted for in the PC that reproduces this number is due to the fact that the number was initially stamped deeper than the others and so had a more extensive zone of plastic strain. This allowed for the thermal gradient difference in this region to account for a larger percentage of the variance in the thermal depth range.

Also, the difference in the PC best identifying the thermal gradient variation can be attributed to discrepancies in the surface conditions around each number from the machining process used in defacing them as well as some variation in the depth of stamped marks and consequently the depth of the zone of plastic strain.

Although hard to visually observe, PCA in projecting the amplitude and phase images into different orthogonal directions captures the variation in degree of phase shift between the amplitude or phase images independent of other linear variations in a single score.

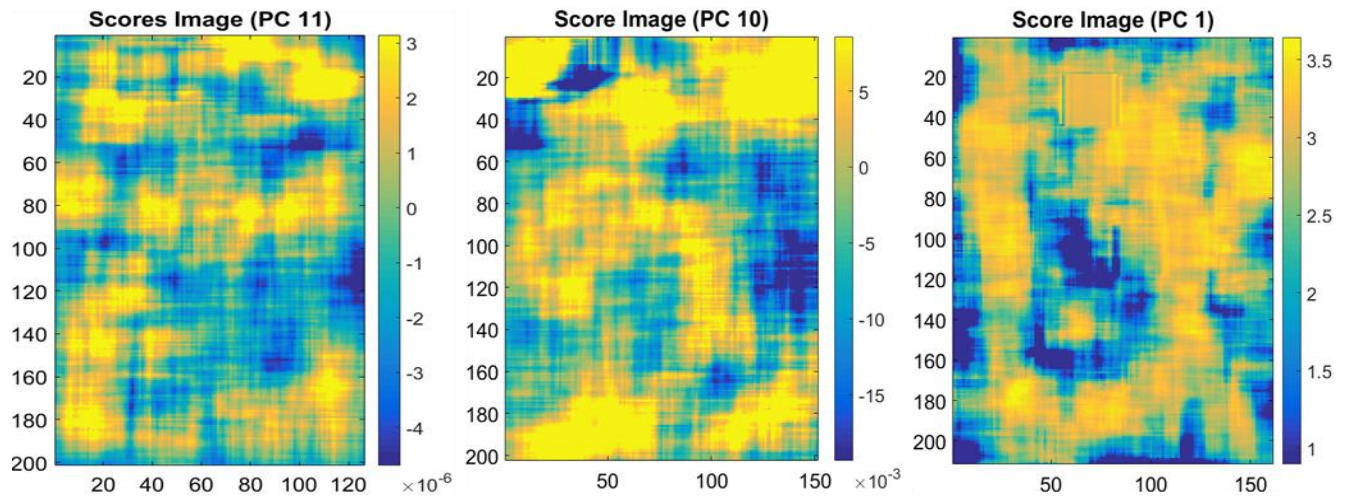


Figure 4.17: Score images showing recovered numbers a) Two b) Five c) Zero (Axes represent the pixel coordinates and the color bar shows the range of score values).

Figure 4.18 shows the score images with the recovered numbers for each of the defaced numbers with some pixels over number areas and some pixels over background areas highlighted. Figure 4.19 shows a plot of the phase value pixels within the area captured in the thermal images over each cycle. Highlighted on these plots are the same pixels highlighted in Figure 4.18 to represent some pixels within the zone of plastic strain (thick red lines) and clean areas (thick black lines). The red lines are individual pixels within the zone of plastic strain to represent the defaced regions and the black lines are pixels from clean areas to represent the background.

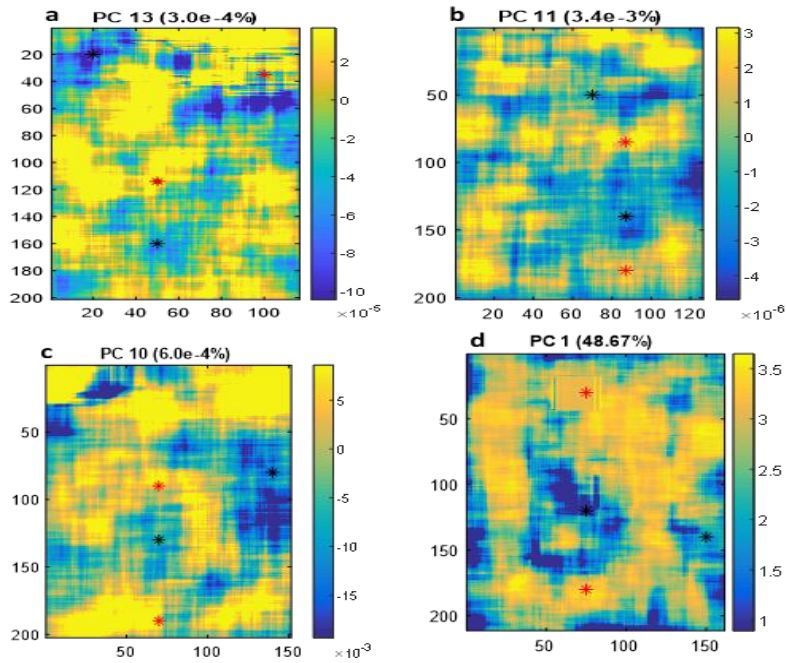


Figure 4.18: Score images with markers for a) six, b) two, c) five, and d) zero.

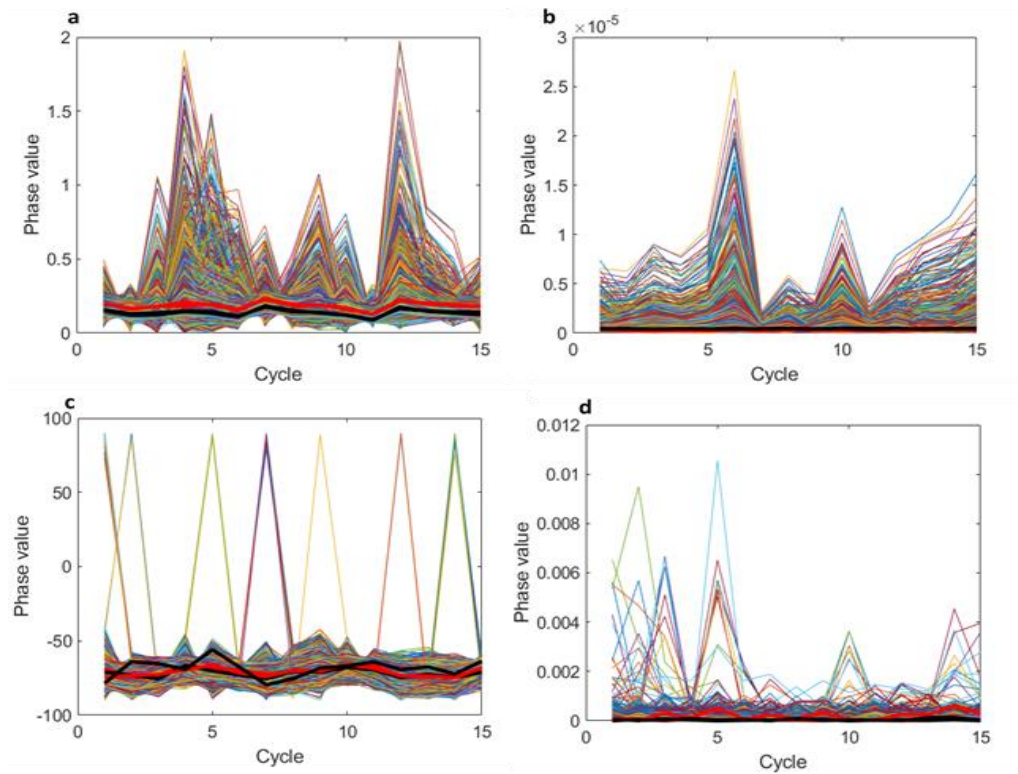


Figure 4.19: Plots of the phase values across experimentation cycles for areas around defaced numbers a) Six b) Two c) Five and d) Zero

From the plots, it can be observed that there is no clear delineation between the phase values within defaced regions and background regions across the cycles. This affirms the need for further processing of the phase or amplitude images to accentuate these differences and recover the defaced numbers.

Figures 4.20a to 4.20d show the plots of the same pixels over the cycles albeit after application of the moving average filter.

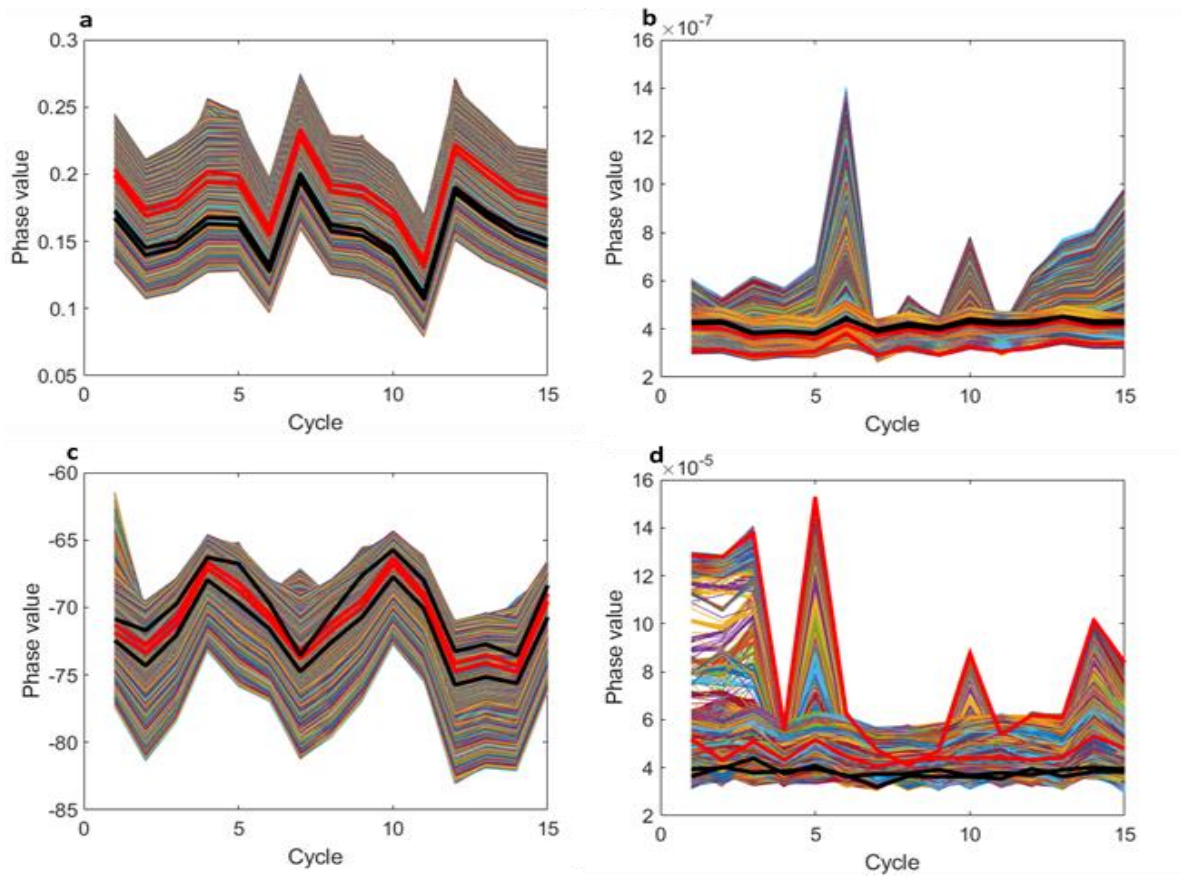


Figure 4.20: Plots of the filtered phase values across experimental cycles for areas around defaced numbers a) Six b) Two c) Five and d) Zero

From the plots, there is some separation in the phase values for the selected pixels albeit not enough to clearly isolate both regions. This indicates that variation in thermal gradient within the zone of plastic strain and the clean areas across pulsing cycles is not very conspicuous. As such,

exploring the relationships between the images in other orthogonal directions not immediately discernible is necessary to isolate these local changes in thermal gradient. This underlines the usefulness of PCA to this process as in projecting the images into different orthogonal directions, other relationships not immediately visible between pixels across images can be examined. A study of how PCA captures the variation in thermal gradient within the zone of plastic strain is shown in Appendix IV.

4.4. GUN BARREL

Figure 4.21 shows the image of the gun barrel after defacing two of the numbers off its surface. The defaced numbers (a '1' and a '2') were completely and the area prepared by cleaning and painting over with black India ink as per the methodology used for the stainless steel plate.



Figure 4.21: Picture of the gun barrel after defacing the 1 and 2.

From the phase difference plot in Figure 4.10, it was observed that other modulation frequencies could prove equally as good as 0.05Hz in capturing the defects within the zone of plastic strain and reproduce the defaced number. The optimal frequency as previously noted is dependent on the depth of the zone of plastic strain and as such on the depth of defacing or amount of material removed from the surface. This may not always be a known factor when handling actual specimens. To avoid the necessity of having to determine an optimal modulation frequency at which to collect the thermal images, testing was extended to four modulation frequencies for each sample to determine their effectiveness in capturing the change in thermal gradient

necessary for recovering the defaced numbers. These frequencies are 1Hz, 0.125Hz, 0.05Hz, and 0.03125Hz corresponding to 1 second, 8 seconds, 20 seconds, and 32 second pulse cycle times respectively. Figures 4.22a to 4.22d show the mean of raw thermal images of the defaced areas around the defaced number 1 on the gun barrel at each of the pulsing frequencies tested. Similar to the stainless steel sample, the stamped number which was completely defaced, is not visible within the thermal images at any of the modulation frequencies.

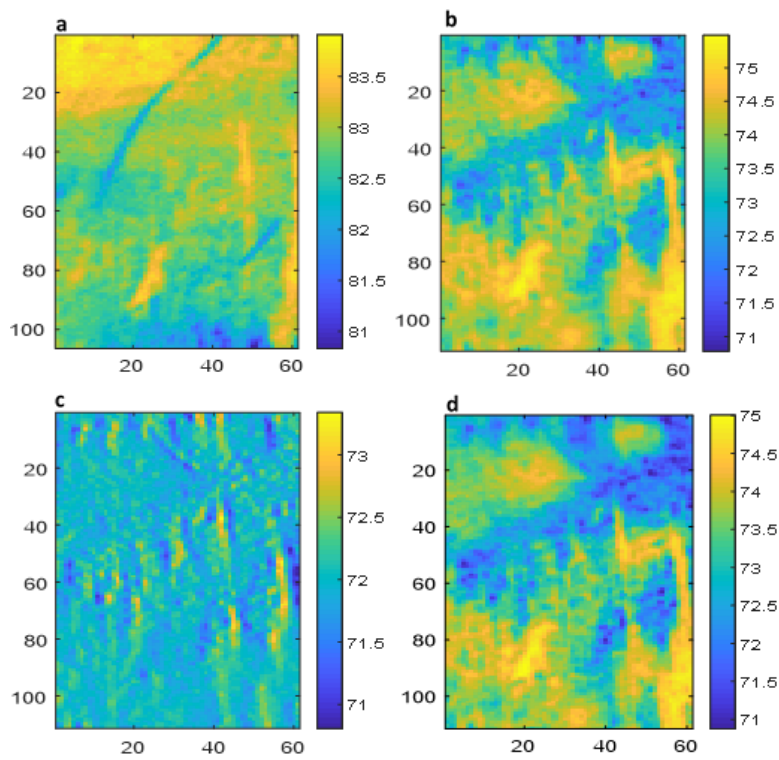


Figure 4.22: Raw thermal images of area around defaced number ‘1’ at modulation frequencies a) 1 Hz, b) 0.125 Hz, c) 0.05 Hz, and d) 0.03125 Hz.

Figures 4.23a to 4.23d show a phase image for each of the tested frequencies. From these images, it is still impossible to visually recognize the number that was removed at any of the test frequencies.

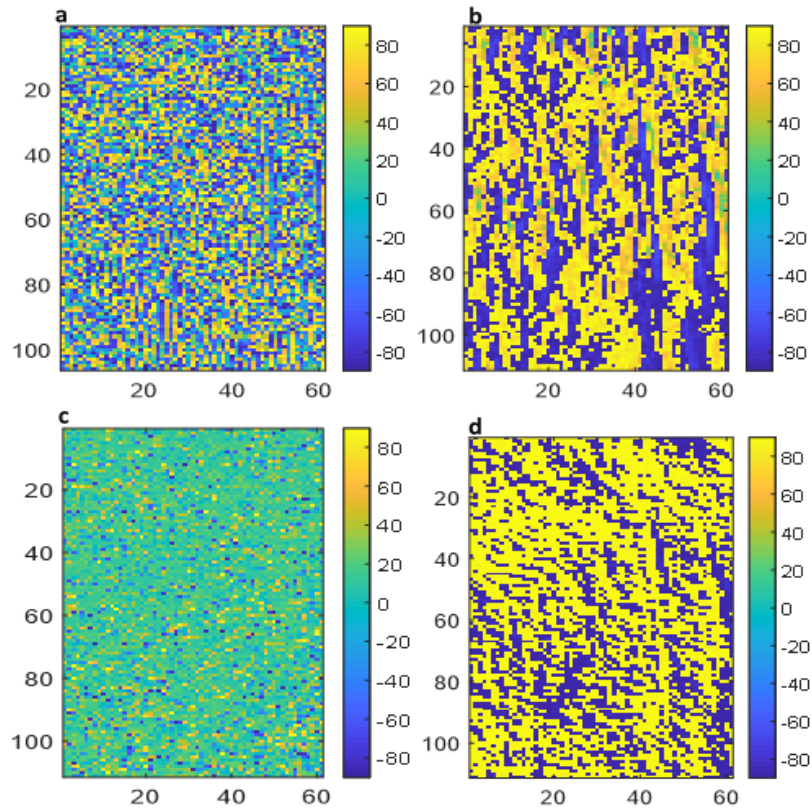


Figure 4.23: Phase images of area around defaced number ‘1’ at modulation frequencies a) 1 Hz, b) 0.125 Hz, c) 0.05 Hz, and d) 0.03125 Hz.

Figures 4.24a to 4.24d show a filtered phase image for each of the tested modulation frequencies. These images were filtered using the moving average filter to enhance contrast within them. However, it is still impossible to visually recognize the number that was removed.

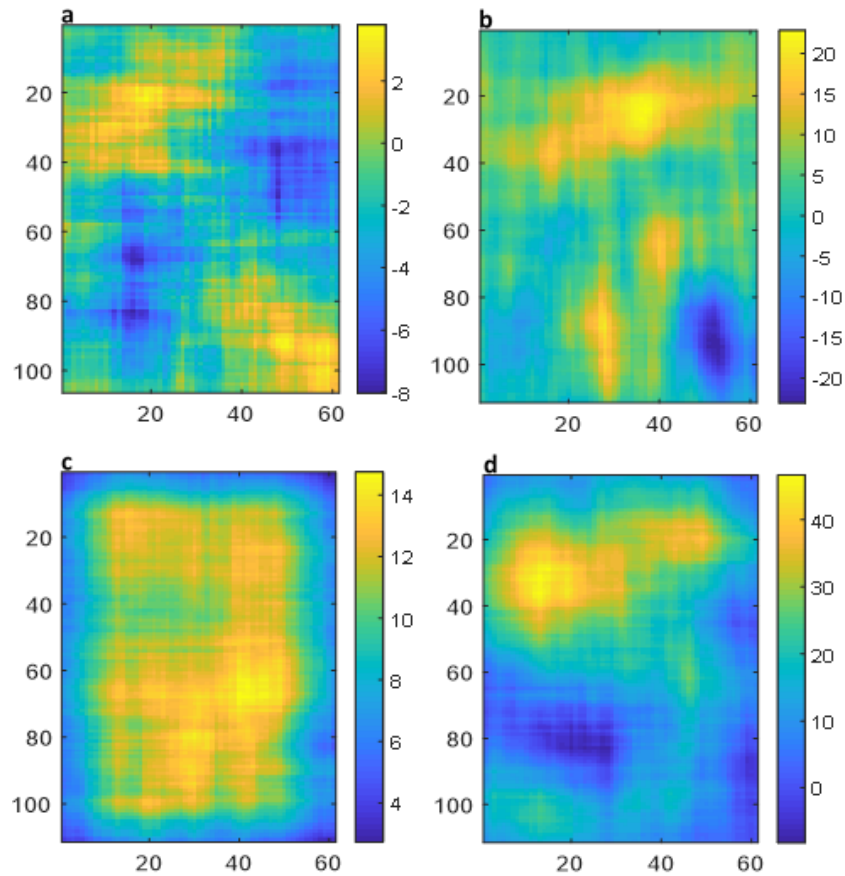


Figure 4.24: Filtered phase images of area around defaced number ‘1’ at modulation frequencies a) 1 Hz, b) 0.125 Hz, c) 0.05 Hz, and d) 0.03125 Hz.

PCA is carried out independently on the matrix of the phase images and that of the amplitude images. Respective score images are visually inspected to determine if phase or amplitude score images best reproduces the defaced number at a modulation frequency. This proved to be the phase images for all four frequencies. Table 4.3 shows the percent variance retained in each PC for each of the four pulsing frequencies tested. The first PC for each dataset as usual explain the most variance with each subsequent PC retaining some of the remaining variance in decreasing order. The shaded cells indicate the PCs where the defaced number could best be visually identified.

Table 4.3: Percentage of Variance in each PC at each modulation frequency tested for defaced number ‘1’ on gun barrel sample (shaded boxes represent the PC where the respective numbers where best reproduced).

PC	Modulation Frequency			
	1	0.125Hz	0.05Hz	0.03125Hz
1	91.1791	54.0024	99.5289	41.0241
2	2.3665	28.2394	0.14496	31.3691
3	1.8969	7.7359	0.090099	14.217
4	0.94709	5.6832	0.080056	9.5675
5	0.72211	1.8421	3.52E-02	9.65E-01
6	0.58137	0.72489	3.34E-02	6.92E-01
7	0.43798	0.4023	2.13E-02	5.85E-01
8	0.39169	0.37679	1.49E-02	3.97E-01
9	0.34045	0.25051	1.23E-02	2.81E-01
10	0.27965	0.18537	9.59E-03	2.31E-01
11	0.19549	0.13789	7.72E-03	1.82E-01
12	0.165	0.12902	6.71E-03	1.35E-01
13	0.14684	0.10858	4.64E-03	1.30E-01
14	0.13233	7.64E-02	4.39E-03	1.02E-01
15	0.11021	6.82E-02	3.84E-03	7.79E-02
16	0.10733	0.037066	2.07E-03	4.37E-02

Figures 4.25a to 4.25e show the PCA score images for the defaced number both before and after defacing. This number shows up in the first PC as expected before defacing. However after defacing, just like with the stainless steel sample, the score image with the recovered numbers were at higher PCs explaining a small percentage of the variance for each of the different modulation frequencies tested (PC7, PC6, PC6 and PC7 respectively) with the best recreation using thermal images collected at pulsing frequency of 0.03125Hz.

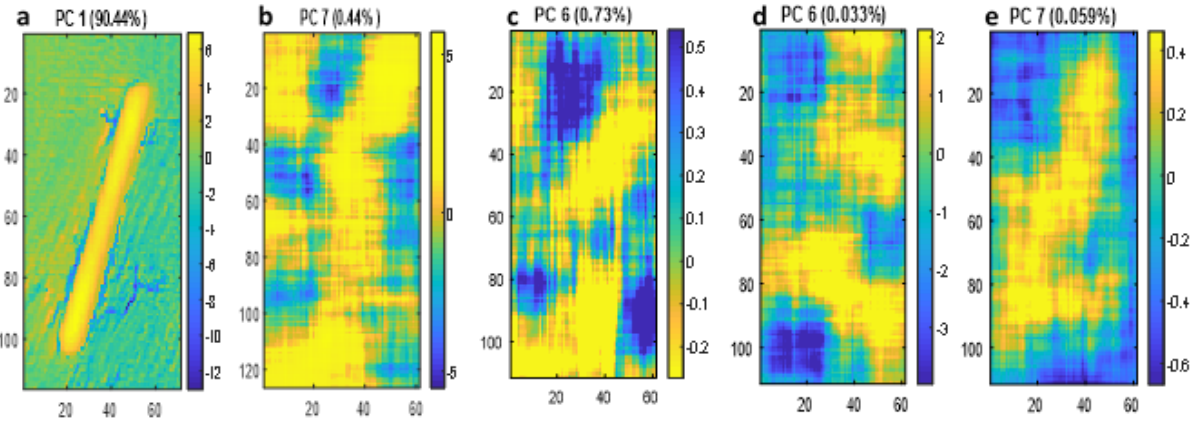


Figure 4.25: Score Images of a) Clean 1 before defacing, and after defacing at b) 1Hz, c) 0.125Hz, d) 0.05Hz, and e) 0.03125Hz.

From these images, it can be inferred that all four modulation frequencies could possibly induce adequate thermal gradients that will reproduce the number in the zone of thermal strain to varying degrees.

Similarly, for the second defaced number, the mean raw thermal images over a single cycle at each of the four pulsing frequencies for the defaced area is shown in Figures 4.26a to 4.26d. The number within the area was also completely removed and as such cannot be seen in the thermal images at any of the pulsing frequencies.

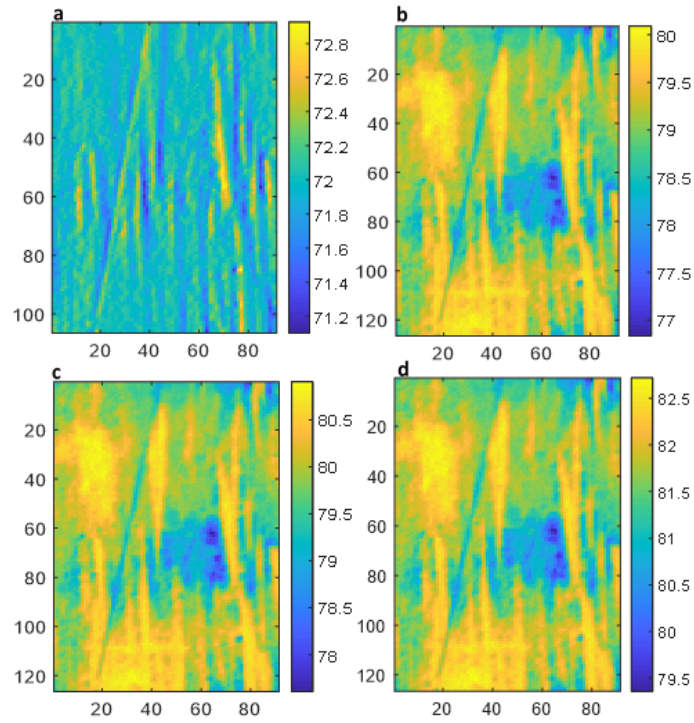


Figure 4.26: Raw thermal images of area around defaced number ‘2’ at modulation frequencies a) 1 Hz, b) 0.125 Hz, c) 0.05 Hz, and d) 0.03125 Hz.

Phase images developed for the thermal images at each modulation frequency are shown in Figures 4.27a to 4.27d. From these images, it is still impossible to identify the removed numbers as the local change thermal gradient within the zone of plastic strain is not sufficiently large.

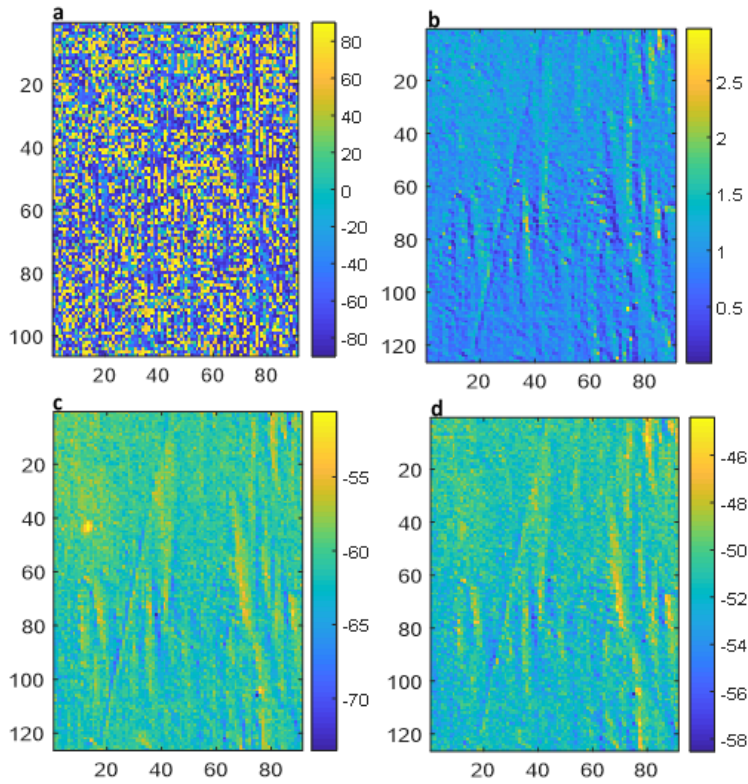


Figure 4. 27: Phase images of area around defaced number ‘2’ at modulation frequencies a) 1 Hz, b) 0.125, Hz c) 0.05 Hz, and d) 0.03125 Hz.

The filtered phase images for each modulation frequency are shown in Figures 4.28a to 4.28d. From these images, the filtering process like in the previous results did not improve the contrast enough to identify the thermal gradient in the zone of plastic strain.

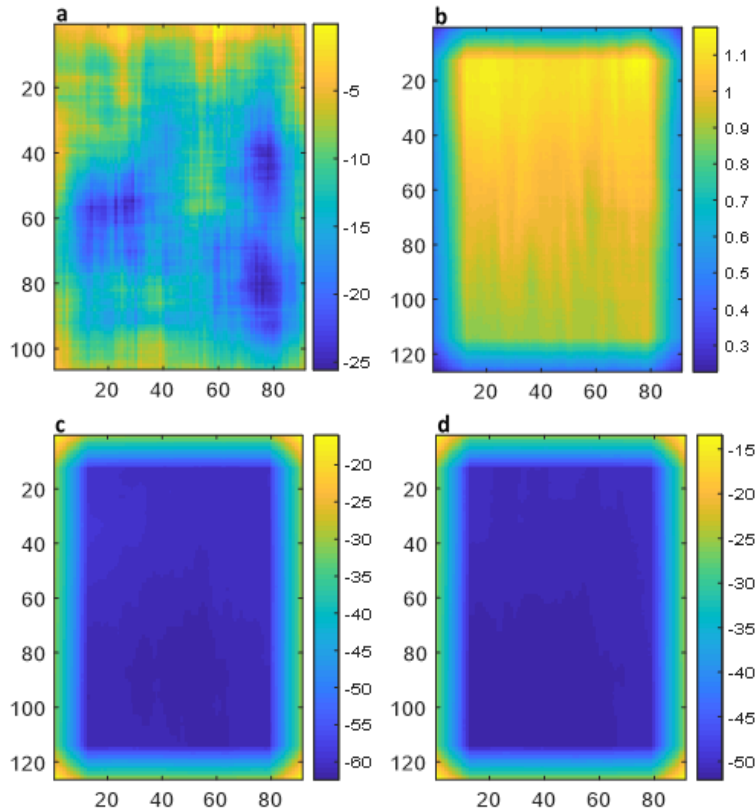


Figure 4.28: Filtered phase images of area around defaced number ‘2’ at modulation frequencies a) 1 Hz, b) 0.125 Hz, c) 0.05 Hz, and d) 0.03125 Hz.

Similar to the previous datasets, PCA is carried out independently on the matrices of the phase images and the amplitude images, and their respective score images visually inspected to determine which set best reproduces the defaced number at a modulation frequency. This proved to be the phase images for frequencies 1 Hz, 0.05 Hz, and 0.03125 Hz. and the amplitude images for 0.125 Hz. Table 4.4 shows the percent variance captured in each PC for the datasets from every pulsing frequency tested. As with the other results, the shaded cells indicate the PC where the variation from the local change in thermal gradient within the zone of plastic strain was best captured, leading to a reproduction of the number. This proved to generally be among the higher PCs that capture a small percentage of the total variance within the dataset at each modulation frequency.

Table 4. 4: Percentage of Variance in each PC at each modulation frequency tested for defaced number ‘2’ on gun barrel sample (shaded boxes represent the PC where the respective numbers where best reproduced).

PC	Modulation Frequency			
	1	0.125Hz	0.05Hz	0.03125Hz
1	45.5419	99.9333	99.9979	99.9936
2	17.0889	0.031937	0.00169	0.005316
3	9.6149	0.012101	0.000182	0.000706
4	6.4484	0.009955	0.000116	0.000223
5	4.8389	0.007851	4.55E-05	9.26E-05
6	4.2432	0.002353	2.14E-05	2.82E-05
7	3.5128	0.000876	8.66E-06	1.58E-05
8	2.1015	0.000429	6.36E-06	1.20E-05
9	1.7242	0.000295	4.54E-06	4.83E-06
10	1.5316	0.00026	4.00E-06	3.17E-06
11	0.8271	0.000164	3.60E-06	2.82E-06
12	0.66094	0.000141	2.71E-06	2.44E-06
13	0.58609	0.000129	2.33E-06	1.86E-06
14	0.47045	9.54E-05	1.93E-06	1.72E-06
15	0.43398	8.52E-05	1.70E-06	1.45E-06
16	0.37518	5.75E-05	1.34E-06	8.78E-07

Figures 4.29a to 4.29e show the PC score images for the number before and after defacing. The number showed up in the first PC when PCA was carried out on a thermal image dataset of the area before defacing. After defacing, the number was partially recovered in a single PC score image for the different modulation frequencies used (PC 11 for 1Hz, PC13 for 0.125Hz, PC7 for 0.05 Hz and PC8 for 0.03125Hz).

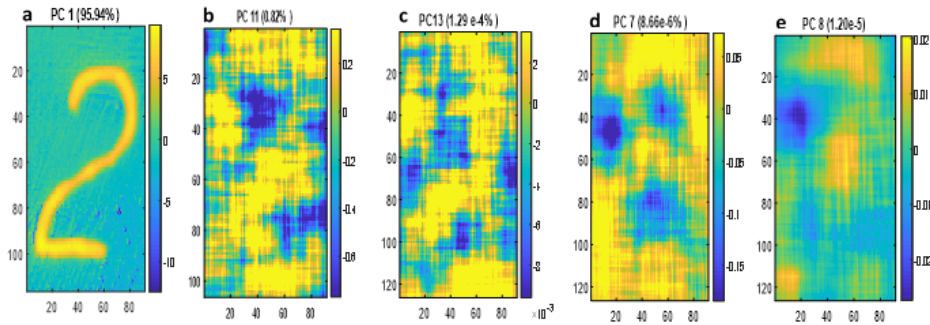


Figure 4.29: Score Images of a) Clean 2 before defacing, and after defacing at b) 1Hz, c) 0.125Hz, d) 0.05Hz, and e) 0.03125Hz.

From the score images best showing enough character from the thermal images, it can be deduced that the four modulation frequencies used in the experiments are adequate for use in collecting thermal images that capture the distinctive thermal gradient in the zone of plastic strain allowing for a recreation of the defaced number. There could however be some slight differences in the quality of the recovery which could be due to changes in the depth of defacing and also the force used in the stamping.

4.5. LASER ENGRAVED NEEDLE HOLDER

The same process was repeated for the laser engraved needle holder with the defaced area pulsed with input energy at four modulation frequencies, and PCA carried out on the amplitude and phase images of each of the four cycles independently. This sample was laser engraved and as such, there is no zone of plastic strain but a heat affected zone extending to depths below the visual mark created. Figure 4.30 shows pictures of the needle holder before and after defacing.

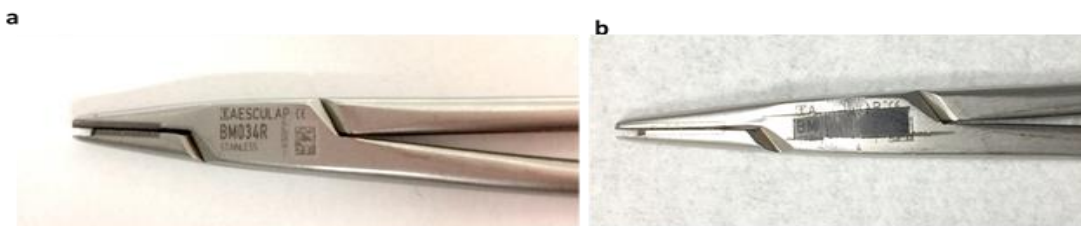


Figure 4.30: Aesculap needle holder with a) Laser engraved numbers and b) numbers defaced and painted with India ink.

Figures 4.31a to 4.31d show the raw thermal images for each modulation cycle for the area over one of the defaced numbers. These images, the average of a single cycle for each of the modulation frequencies, do not show sufficient contrast of the local change in thermal gradient to allow for a visualization of the defaced number.

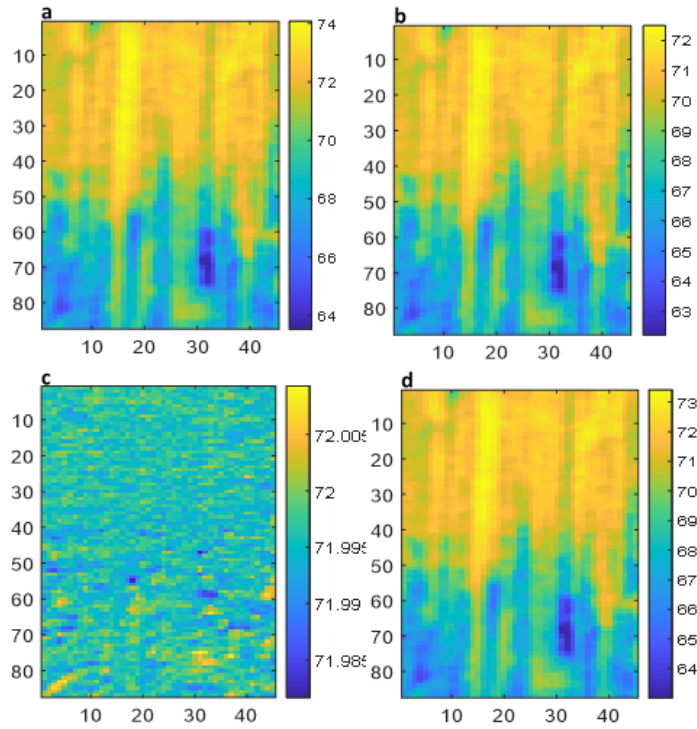


Figure 4.31: Raw thermal images of area around defaced number ‘0’ at modulation frequencies a) 1 Hz, b) 0.125 Hz, c) 0.05 Hz, and d) 0.03125 Hz.

Figures 4.32a to 4.32d show the phase images for one cycle at each modulation frequency for the defaced area. Similar to the other tested samples, none of the developed phase images show adequate change in the phase shift within the heat affected zone to allow for the defaced number to be observed.

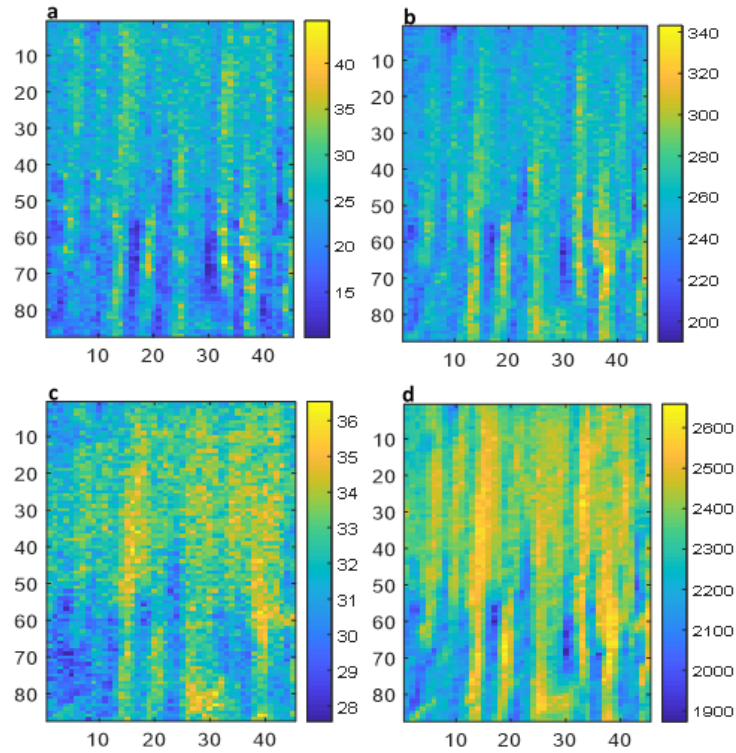


Figure 4.32: Phase images of area around defaced number ‘0’ at modulation frequencies a) 1 Hz, b) 0.125 Hz, c) 0.05 Hz, and d) 0.03125 Hz.

Figures 4.33a to 4.33d show the filtered phase images for each frequency tested. As with the other datasets, the filtering did not improve contrast within the images enough to observe the thermal gradient changes that will indicate the defaced number.

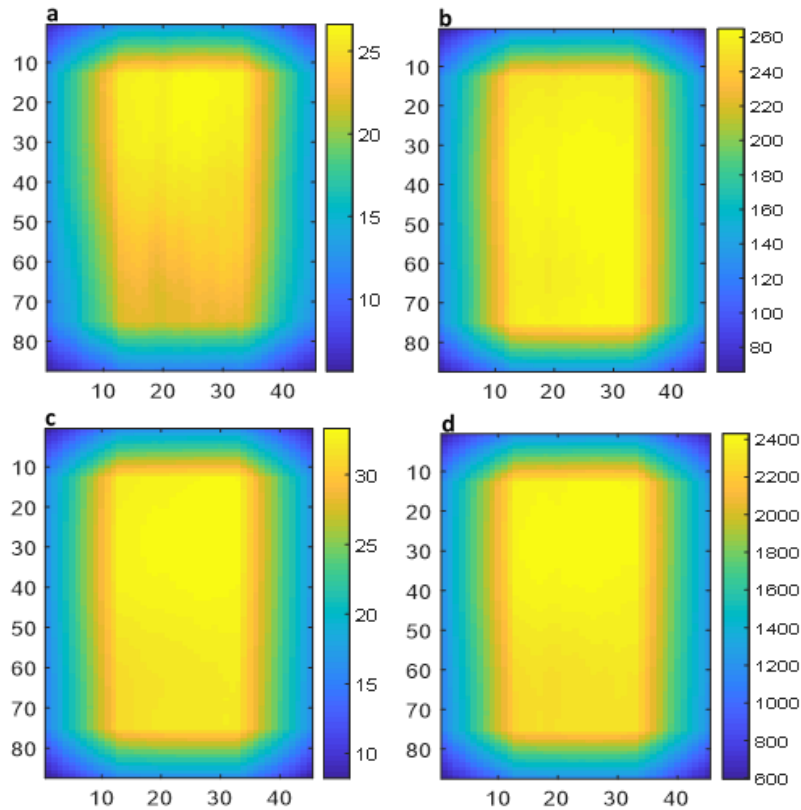


Figure 4.33: Filtered phase images of area around defaced number ‘0’ at modulation frequencies a) 1 Hz, b) 0.125 Hz, c) 0.05 Hz, and d) 0.03125 Hz.

Score images from PCA on the phase images and amplitude images are visually inspected to determine which set best captured the thermal gradient in the heat affected zone to characterize the defaced number. This proved to be the amplitude score images at all four modulation frequencies. Table 4.5 shows the percent variance retained in each PC after PCA was carried out on the dataset of filtered images. The shaded cells indicate the PC where it was deemed the defaced number was best reproduced at each of the modulation frequencies tested. As with the previous samples, the score images with the recovered digits are the higher PCs explaining small amounts of variance with the number 0 in PCs 15, 13, 12 and 10 for each frequency respectively.

Table 4.5: Percentage of Variance in each PC at each modulation frequency tested for defaced number ‘0’ on gun barrel sample (shaded boxes represent the PC where the respective numbers where best reproduced).

PC	Modulation Frequency			
	1	0.125Hz	0.05Hz	0.03125Hz
1	99.9114	99.9963	99.9946	99.9978
2	0.072341	0.002178	0.004677	0.001806
3	0.012618	0.000739	0.00042	0.000299
4	0.001618	0.000538	0.000211	6.54E-05
5	0.001128	0.000147	2.13E-05	1.29E-05
6	0.00027	2.15E-05	1.39E-05	1.86E-06
7	0.000169	1.22E-05	6.97E-06	9.90E-07
8	0.000108	7.55E-06	5.60E-06	9.00E-07
9	9.22E-05	4.49E-06	4.55E-06	6.49E-07
10	6.51E-05	3.59E-06	3.34E-06	5.16E-07
11	4.81E-05	3.18E-06	2.33E-06	4.51E-07
12	3.77E-05	2.41E-06	1.70E-06	3.39E-07
13	3.65E-05	2.24E-06	1.48E-06	3.14E-07
14	2.79E-05	1.85E-06	1.19E-06	2.79E-07
15	2.43E-05	1.43E-06	9.18E-07	1.99E-07
16	1.82E-05	1.04E-06	7.17E-07	1.55E-07

Figure 4.34 shows the score images with the defaced number 0 recovered after PCA. Each of the images in the figure represents a score image from one of the modulation frequencies tested. These score images were selected as those with the best visual representation of the number removed from the area. From the images, it can be seen that at each of the frequencies, some local change in thermal gradient was captured that allowed for a reproduction of the number.

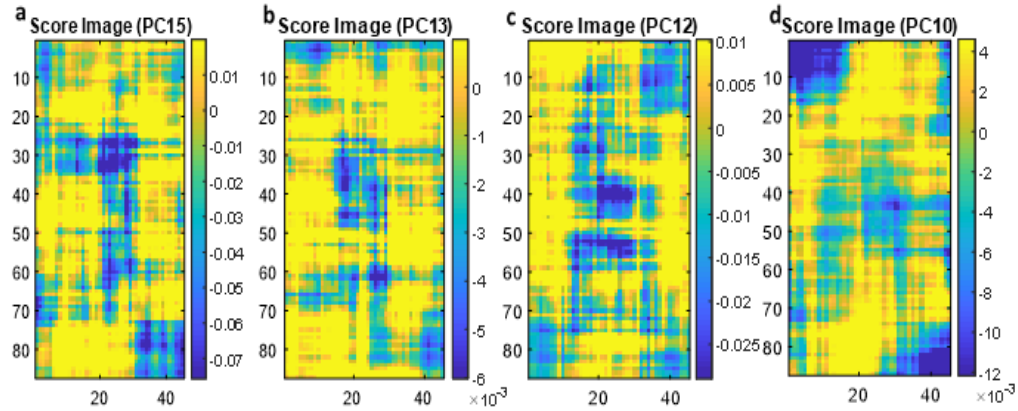


Figure 4.34: Score Images of defaced area around 0 at a) 1Hz, b) 0.125Hz, c) 0.05Hz, and d) 0.03125Hz.

Figures 4.35a to 4.35d show the raw thermal images of the area around the removed number ‘3’. As with the other samples, the number was completely removed and the raw thermal images do not show enough contrast to allow for a visualization of the removed number.

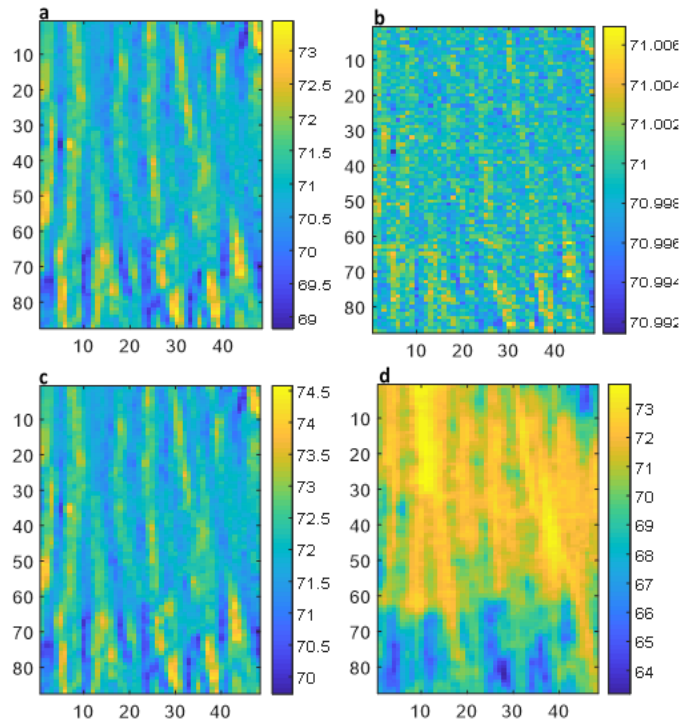


Figure 4.35: Raw thermal images of area around defaced number ‘3’ at modulation frequencies a) 1 Hz, b) 0.125 Hz, c) 0.05 Hz, and d) 0.03125 Hz.

Figures 4.36a to 4.36d show the phase images of the defaced area for each of the tested modulation frequencies. From these images, there isn't sufficient change in the degree of phase shift in the heat affected zone to visually observe the removed number.

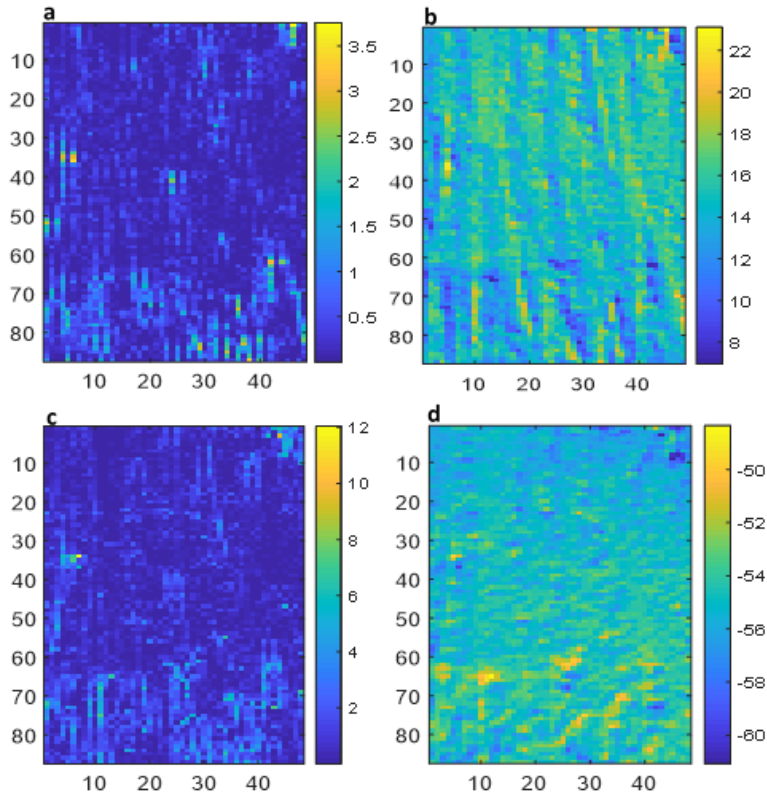


Figure 4.36: Phase images of area around defaced number '3' at modulation frequencies a) 1 Hz, b) 0.125 Hz, c) 0.05 Hz, and d) 0.03125 Hz.

Figures 4.37a to 4.37d show the filtered phase images at each of the modulation frequencies tested. This process as with the other datasets did not improve contrast enough to allow for an immediate visualization of the removed number.

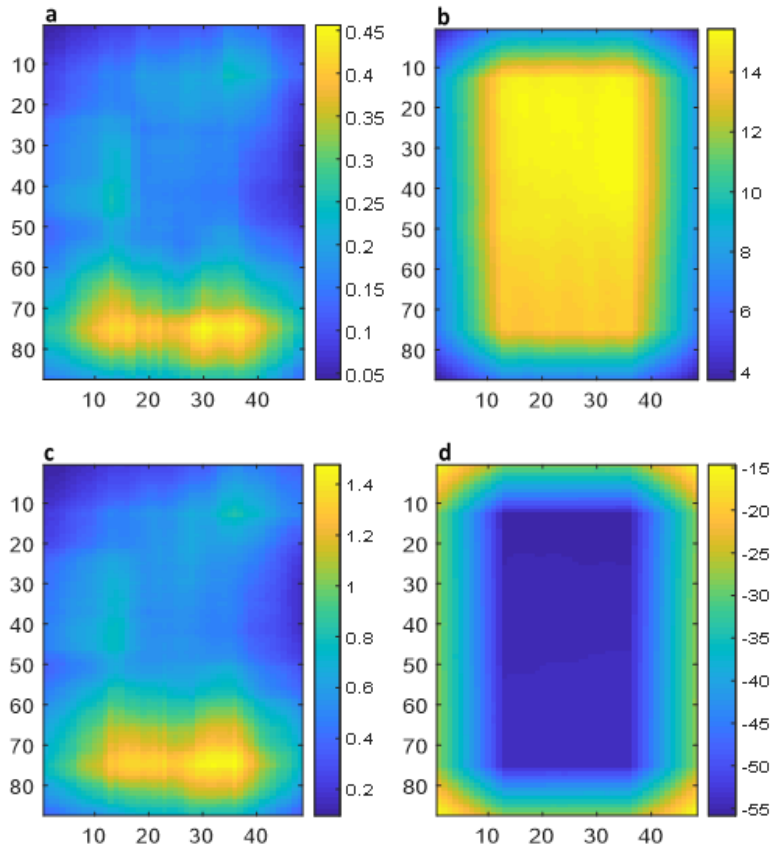


Figure 4.37: Filtered phase images of area around defaced number ‘3’ at modulation frequencies a) 1 Hz, b) 0.125 Hz, c) 0.05 Hz, and d) 0.03125 Hz.

As with the prior datasets, PCA is carried out independently on the matrix of the phase images and that of the amplitude images and the respective score images are visually inspected to determine which best reproduces the defaced number at a modulation frequency. This proved to be the amplitude score images for frequencies 1 Hz, 0.125 Hz, and 0.05 Hz, and the phase score images for 0.03125 Hz. Table 4.6 shows the percent variance retained in each PC after PCA was carried out on the individual datasets developed from the filtered phase at each of the tested modulation frequencies. The shaded cells indicate the PC where the defaced number was best visually reproduced. As with the previous samples, the score images with the recovered digits are the higher PCs explaining small amounts of variance.

Table 4.6: Percentage of Variance in each PC at each modulation frequency tested for defaced number '3' on laser engraved needle holder sample (shaded boxes represent the PC where the respective numbers where best reproduced).

PC	Modulation Frequency			
	1	0.125Hz	0.05Hz	0.03125Hz
1	97.3945	99.9711	96.2789	99.9819
2	1.1318	0.023977	2.1908	0.01715
3	1.0441	0.003399	0.88534	0.000634
4	0.20682	0.000937	0.29655	0.00021
5	0.13502	0.000371	1.53E-01	4.25E-05
6	0.028582	0.000105	9.65E-02	1.88E-05
7	0.018714	4.43E-05	4.34E-02	9.25E-06
8	0.01319	2.27E-05	1.44E-02	4.92E-06
9	0.00731	2.16E-05	1.35E-02	2.83E-06
10	0.005439	1.34E-05	7.81E-03	2.27E-06
11	0.004182	9.92E-06	5.52E-03	2.17E-06
12	0.003805	8.32E-06	4.93E-03	1.72E-06
13	0.00262	7.42E-06	3.78E-03	1.53E-06
14	0.001838	4.58E-06	2.86E-03	1.23E-06
15	0.001254	3.94E-06	1.66E-03	9.44E-07
16	0.00091	3.23E-06	9.29E-04	7.06E-07

Figure 4.38 shows the score images from different modulation frequencies for the results of the process for the defaced number 3. From the images, it can be seen that all four modulation frequencies created some thermal gradient within the hart affected zone to allow for a recreation of the defaced number, although with slight variations in the quality of the recreation.

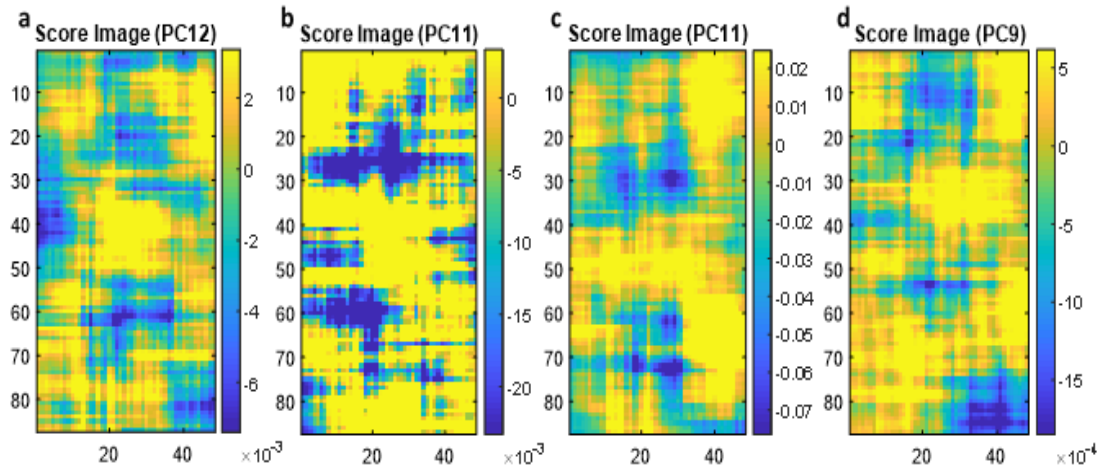


Figure 4.38: Score Images of defaced area around number 3 at a) 1Hz, b) 0.125Hz, c) 0.05Hz, and d) 0.03125Hz.

From both sets of results, it can be inferred that all four modulation frequencies adequately captured the thermal gradient changes within the heat affected zone, leading to the characterization of the defaced numbers in a score image.

These results show that all four modulation frequencies tested could possibly induce adequate thermal gradients and reproduce an estimated representation of the number. However, as a result of variations in depth of defacing and also depth of zone of plastic strain from the stamping or laser engraving process, there might be slight changes in the quality of the recreated number in a score image at different frequencies. Thus, it can be considered good investigative practice to collect thermal images over several modulation frequencies for a sample to analyze and recover a defaced number.

4.6. MOTORCYCLE VIN

From the still intact numbers on the engine block, it was determined that some of the VIN numbers were 5-2-5-1-[-]-0-[-]-4-1 with the square brackets indicating the completely removed numbers. An initial challenge was to narrow down the locations of the stamped numbers in the

fork. To do this, the entire defaced area was divided into three sections as shown in Figure 4.39, and each independently analyzed using the LIT and image analysis process. This was done to investigate the possibility of locating the zone of plastic strain around some of the defaced numbers and use that to locate the possible positions of other numbers in the area.

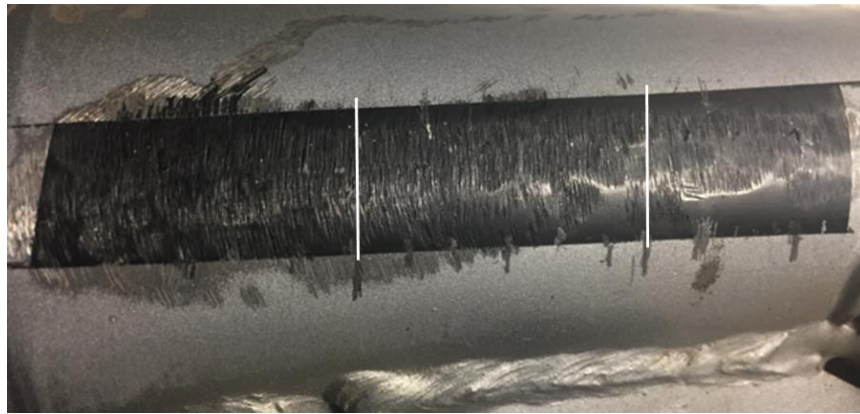


Figure 4.39: Defaced motorcycle fork painted with India ink (white lines show the sections of the area individually imaged and analyzed).

The initial assessment of the middle section in Figure 4.39 showed what appeared to be parts of numbers that were not fully defaced, allowing for the identification of the local areas where the numbers were stamped. Figure 4.40 shows the score image of this area and the center to center distance between each of the possible areas was determined for use as a guide to the possible positions of the other numbers that were totally removed. This distance from the score image was determined to be approximately 125 pixels wide. The bounded regions (white boxes in Figure 4.40) were extracted from the dataset and independently reanalyzed by PCA to enhance the thermal signature of the zone of plastic strain to aid the recovery of the defaced numbers.

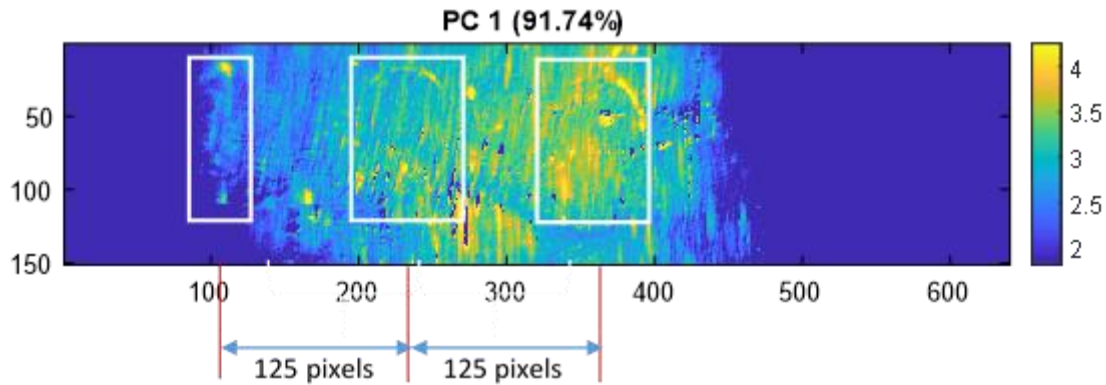


Figure 4.40: Score Image of a section of defaced area showing some partially defaced numbers. A similar assessment of the first section produced an area in a PC score image that could conceivably be identified as the zone of plastic strain beneath a defaced number. This area was extracted as a region of interest within the bounds of the white box shown on the image in Figure 4.41 and reanalyzed independently. The center to center distance previously determined from the assessment of the middle section was used to determine the center of the next two numbers in the image to form the regions of interest (red boxes in Figure 4.41) to be reanalyzed independently.

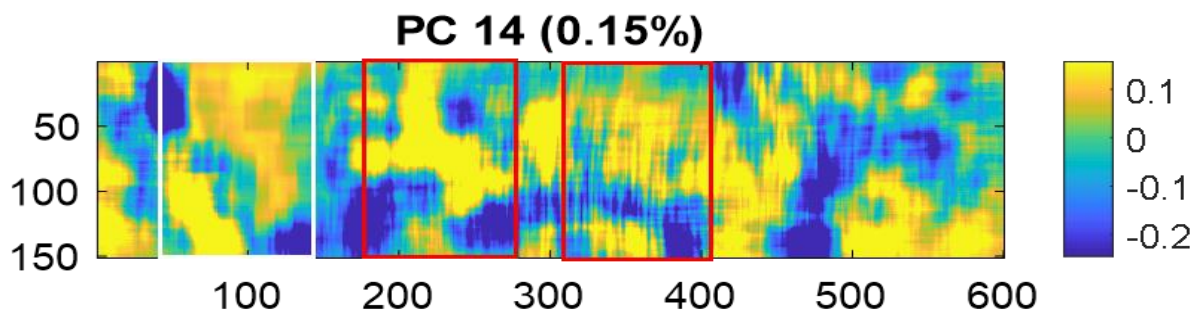


Figure 4.41: Score Image of a section of defaced area showing a possible number (in white box) and other localized areas (in red boxes).

The initial assessment of the third section from Figure 4.39 can be seen in Figure 4.42. From the score image, a characteristic shape that could be conceived as representative of the local zone of plastic strain was identified and the region of interest localized (white box in Figure 4.42). This

localized area was used to determine the possible locations of other numbers in this section (red boxes in Figure 4.42) via the center to center distance determined from the partially defaced numbers in Figure 4.40.

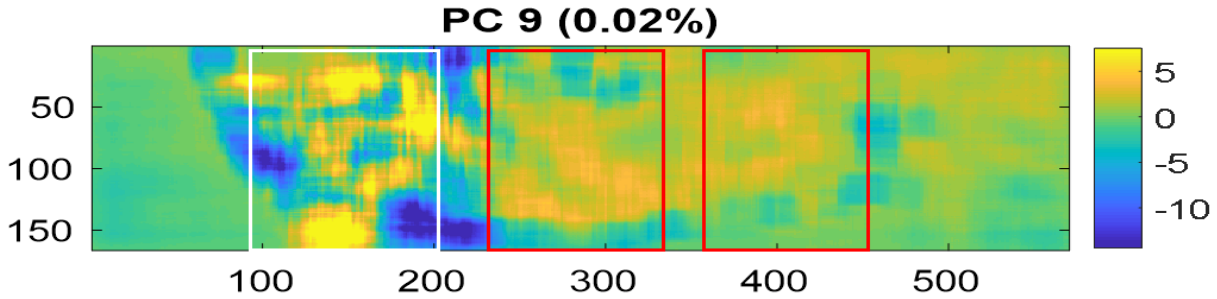


Figure 4.42: Score Image of a section of defaced area showing a possible number (in white box) and other localized areas (in red boxes).

Each of these localized regions of interest was independently analyzed using PCA to recover the defaced numbers. Figures 4.43a to 4.43i show mean thermal images of a single cycle for each of the localized regions. These thermal images were each from a single modulation cycle, and do not show enough detail to visually identify the numbers removed.

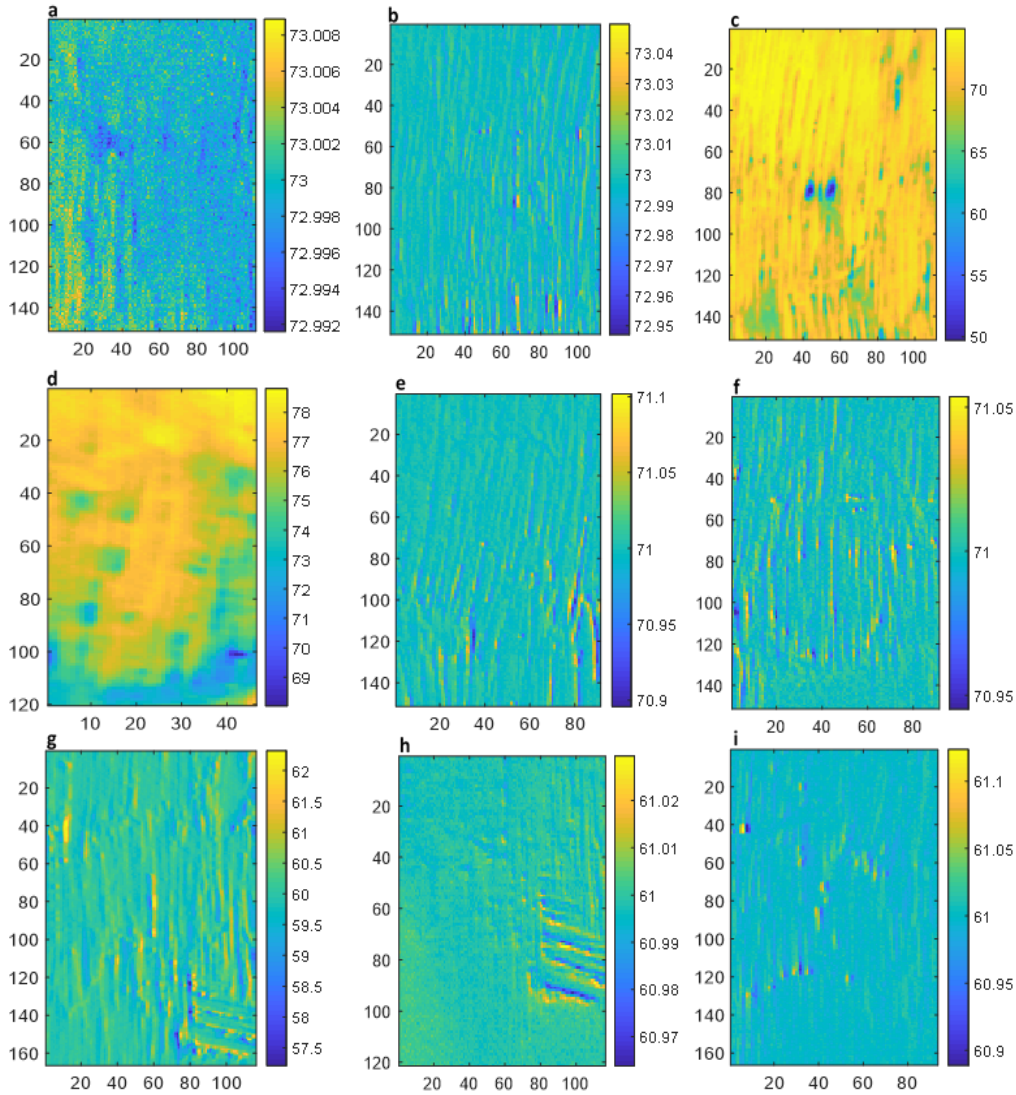


Figure 4.43: Raw thermal images of area around defaced numbers a) five, b) two, c) five, d) one, e) unknown, f) zero, g) unknown h) four i) one.

Figures 4.44a to 4.44i show phase images for each of the localized areas at the cycle time where it was deemed the number was best reproduced. Similar to the other samples, these images do not show enough contrast to reveal the number that existed there before defacing.

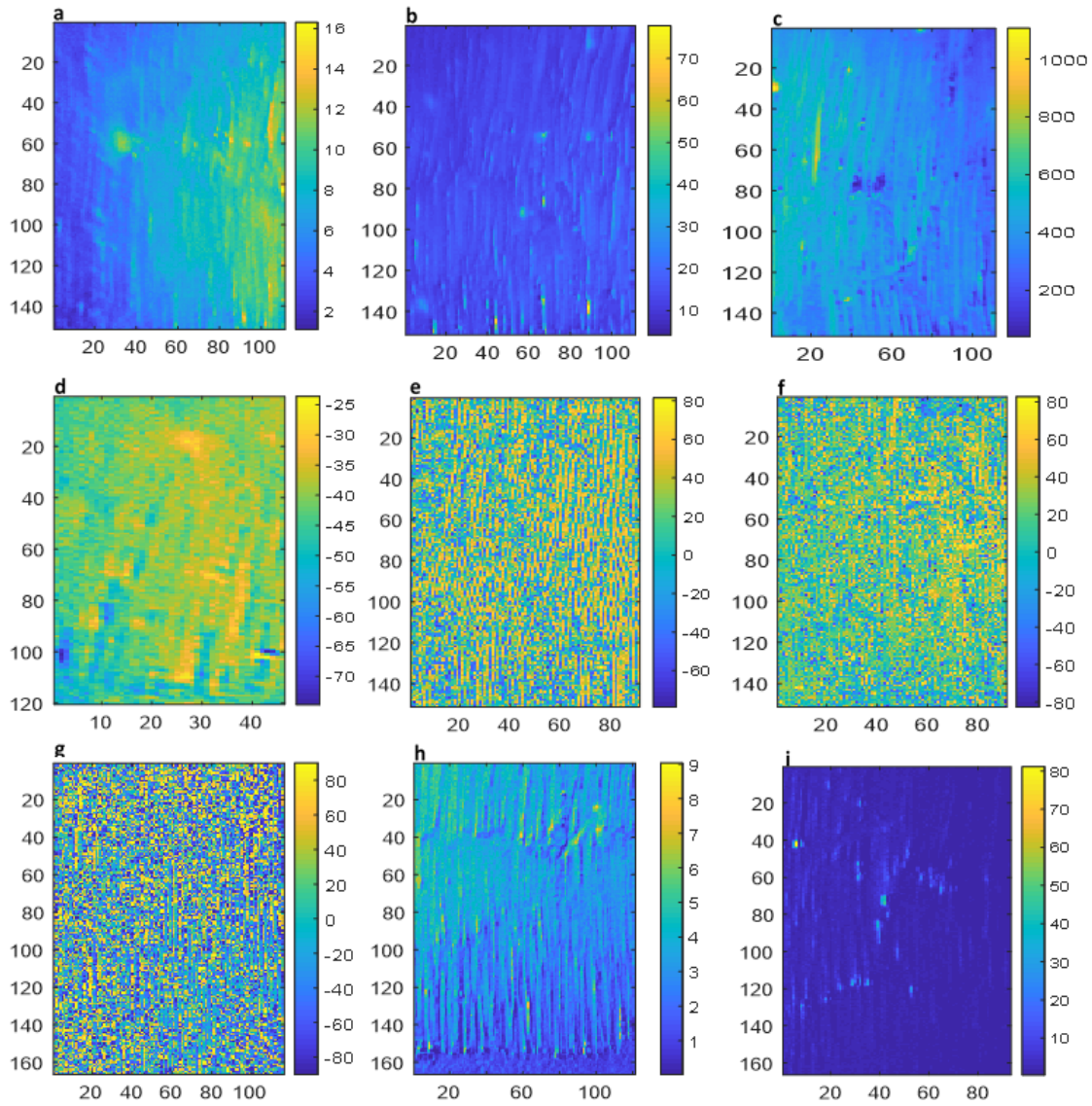


Figure 4.44: Phase images of area around defaced numbers a) five, b) two, c) five, d) one, e) unknown f) zero g) unknown h) four, and i) one.

Figures 4.45a to 4.45i show the filtered phase images which were used as input for PCA. These filtered images also do not show enough contrast to allow for a visual identification of the defaced numbers.

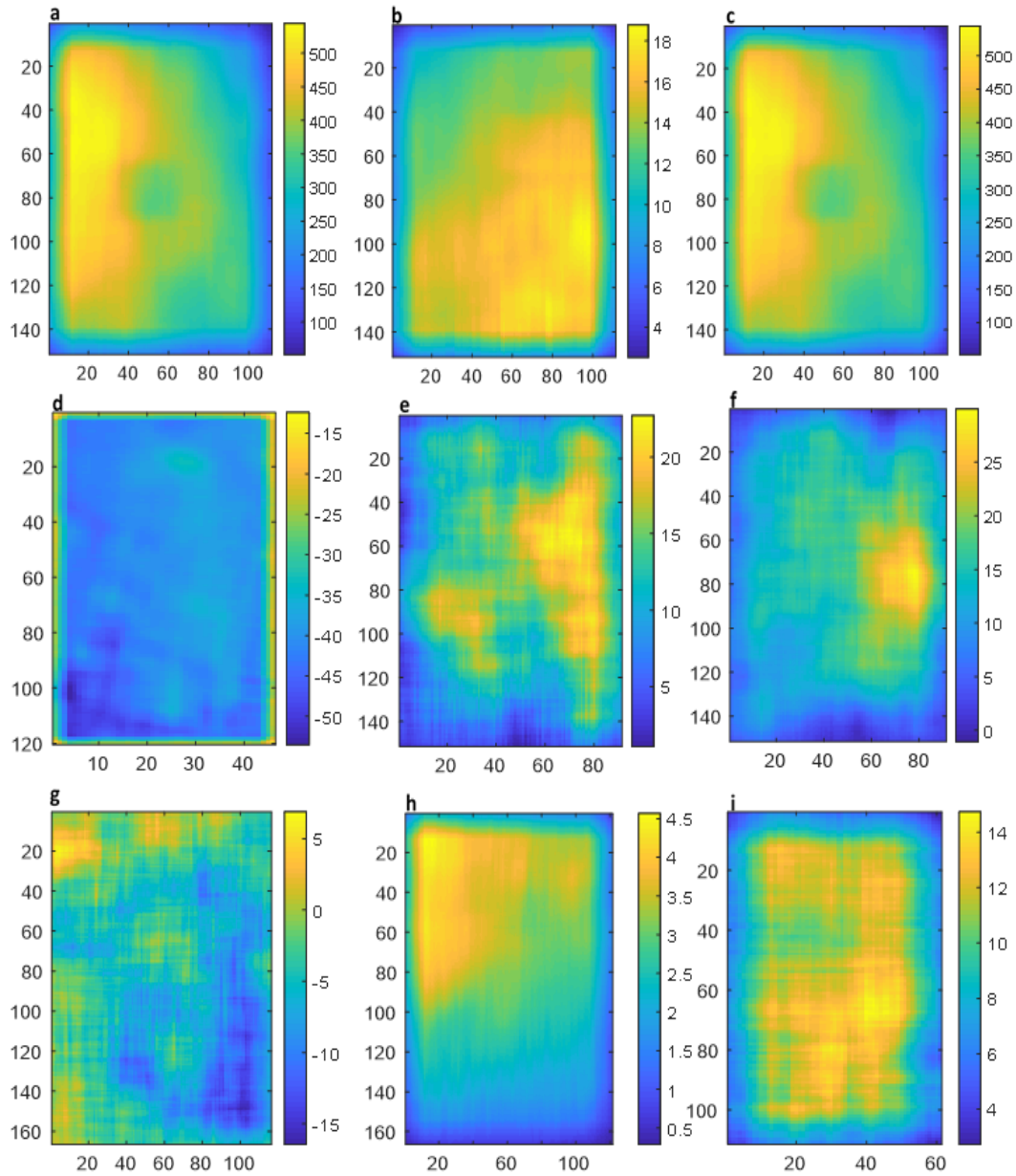


Figure 4.45: Filtered phase images of area around defaced numbers a) five, b) two, c) five, d) one, e) unknown f) zero, g) unknown, h) four and i) one.

Table 4.7 shows the percent variance retained in each PC for one of the modulation frequencies tested. The values shown are from a modulation frequency selected for each number as one in which there was adequate characterization of the zone of plastic strain to allow for a visualization of the defaced number in a score image. The shaded cells indicate the PC score

image where the defaced number was best reproduced. From these results, the trend observed in previous samples where this reproduction was predominantly among the higher PCs continues with the exception of one of the numbers (the number ‘1’) which was only partially defaced and so created significant thermal gradient, enough to be reproduced in the first PC.

Table 4.7: Percentage of Variance in each PC for defaced numbers on motorcycle (shaded boxes represent the PC where the respective numbers where best reproduced).

PC	Defaced Number								
	5 (0.03125Hz)	2 (0.03125Hz)	5 (0.03125Hz)	1 (0.05Hz)	0 (0.05Hz)	0 (0.05Hz)	7 (0.05Hz)	4 (0.05Hz)	1 (0.05Hz)
1	99.9601	99.9643	99.9708	99.9460	80.0614	34.3174	42.8527	99.8909	98.2104
2	0.0212	0.0190	0.0169	0.0271	12.2010	23.2606	15.0687	0.0713	1.0260
3	0.0108	0.0103	0.0081	0.0109	3.4953	18.6236	11.1686	0.0163	0.3554
4	0.0054	0.0042	0.0017	0.0086	1.3843	11.2150	6.1006	0.0104	0.1796
5	0.0011	0.0011	0.0014	0.0015	0.8598	3.7907	4.4020	0.0044	0.0868
6	0.0005	0.0004	0.0006	0.0014	0.5473	2.5753	3.9273	0.0027	0.0522
7	0.0004	0.0003	0.0002	0.0008	0.3095	1.7994	3.1376	0.0011	0.0293
8	0.0001	0.0003	0.0001	0.0007	0.2826	1.3608	2.5688	0.0010	0.0140
9	0.0001	0.0001	0.0001	0.0007	0.1877	0.9476	2.1240	0.0007	0.0118
10	0.0001	0.0001	0.0001	0.0005	0.1588	0.6630	1.8626	0.0005	0.0104
11	0.0000	0.0000	0.0000	0.0004	0.1408	0.4477	1.5737	0.0003	0.0073
12	0.0000	0.0000	0.0000	0.0003	0.1211	0.3785	1.4131	0.0002	0.0054
13	0.0000	0.0000	0.0000	0.0003	0.0967	0.2653	1.3227	0.0001	0.0043
14	0.0000	0.0000	0.0000	0.0003	0.0573	0.1463	1.0354	0.0001	0.0032
15	0.0000	0.0000	0.0000	0.0003	0.0516	0.1112	0.8931	0.0001	0.0020
16	0.0000	0.0000	0.0000	0.0002	0.0449	0.0976	0.5492	0.0001	0.0018

Figure 4.46 shows the score images for the different areas with the numbers partially recovered. These images were selected by visual inspection of the score images at all four modulation frequencies as reasonably capturing the local variation in the zone of thermal strain around the defaced numbers. As with the other samples, only one score image shows enough detail to mark out the zone of plastic strain peculiar to areas where numbers were defaced off, with the other score images characterizing other physical elements within the region of interest. These are

usually among the higher PC score images, detailing how infinitesimally small the changes due to thermal conductivity differences are within these regions and as such the percentage of the variation explaining these thermal gradient changes in the score images.

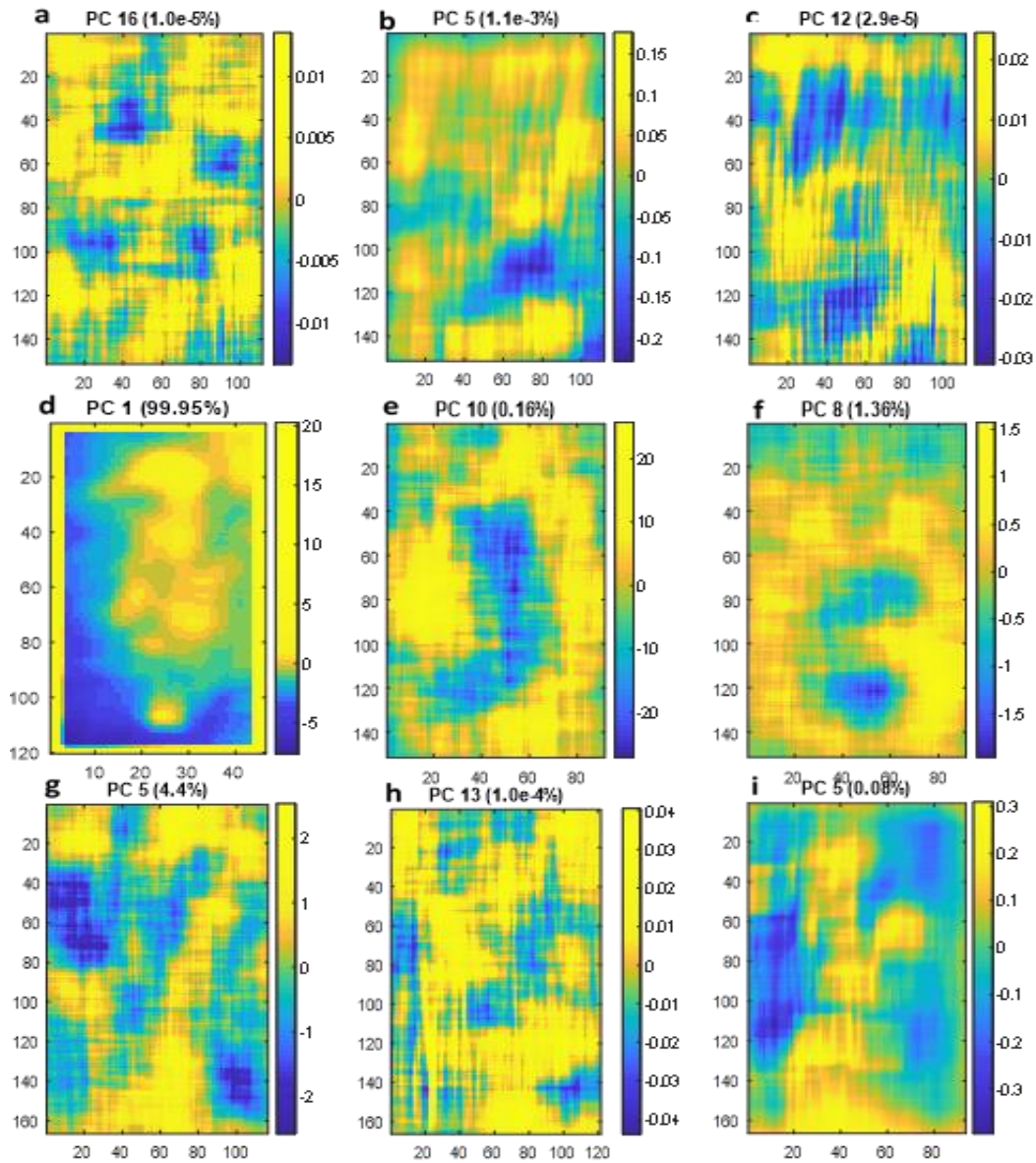


Figure 4.46: Score images showing the recovered VIN numbers a) 5 (0.03125Hz), b) 2 (0.03125Hz), c) 5 (0.03125Hz), d) 1 (0.05Hz), e) unknown (0.05Hz), f) 0 (0.05Hz), g) unknown (0.05Hz), h) 4 (0.05Hz), and i) 1 (0.05Hz).

Similar to the other tested samples, thermal images collected at all four modulation frequencies capture enough of the thermal gradient to characterize the zone of plastic strain and recover the defaced numbers. However, due to the differing depths of defacing, there were slight differences in the quality of the recreated number. Such discrepancies in conditions and the ensuing effects on the quality of recreated numbers lends credence to the idea that it is advantageous to investigate several modulation frequencies, avoiding a need to determine a best modulation frequency for use.

From the figures in Figure 4.46, although the characterization of the zone of plastic strain allowed for partial recognition of the defaced number, the numbers are not easily discernable. This is partly due to difficulty in evenly raising the base temperature of the sample as is necessary to reduce lateral thermal gradients and partly due to the uncontrolled nature of the defacing. These difficulties, further highlight the necessity of identifying the numbers independent of human bias underscoring the importance of the identification protocol.

CHAPTER 5

5.0. NUMBER IDENTIFICATION

As outlined in Chapter 3, the number identification stage involves a number of steps, a fundamental one being the extraction of features from the score images as well as the reference library images. This is a key feature in making the overall number identification automated, with minimal human judgement as the extracted moments allow both the library images and the score images to be converted to a form that can easily be compared. The comparison involves the use of similarity measures to determine the similarity or otherwise of the score images to the library images, and fusion to determine a consensus of identification from the similarity measures. Two closely related feature extraction methods were tested to determine which would be ideal to use in classifying the score images appropriately. The results for these methods (Zernike moments and pseudo Zernike moments) are presented in this chapter.

After identification, conformal prediction was used to assign confidence indices to the identification results, as a measure of the accuracy of the identification results. The results of the conformal prediction process are also presented in this chapter.

5.1. ZERNIKE MOMENTS

Extracting features using Zernike moments require the determination of a suitable polynomial order at which pertinent features representative of the image are captured. To determine a suitable range of orders, the mean square error of reconstruction at increasing orders is calculated and the cumulative sum of these differences is used to estimate the orders that fully capture the image features as explained in Chapter 3.

Figure 5.1 shows the reconstruction errors for a couple of the reference library images, juxtaposed with the cumulative reconstruction error plot for the score image of the defaced number 2. These plots indicate a similar range of orders adequately explain both the score

images for the recovered numbers and the reference library images, allowing for a selection of a range that adequately describe the images to be compared using similarity measures. Similar plots are obtained for other library and score images.

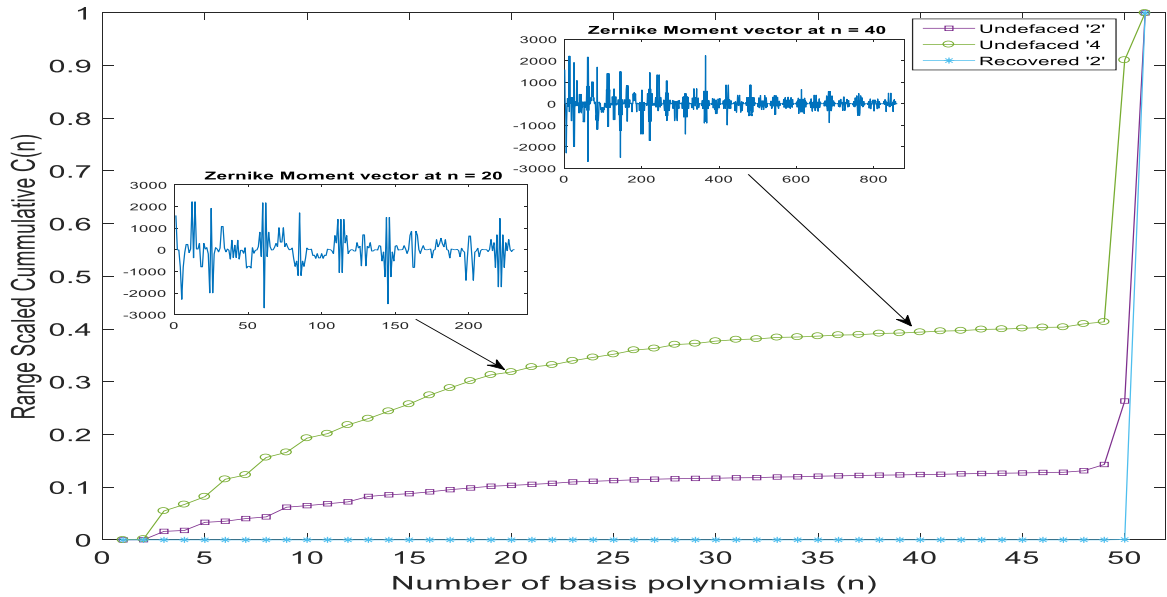


Figure 5.1: Cumulative mean square error difference for an increasing order of Zernike polynomials shown for two reference library numbers and a recovered number as examples. See text for description of insets.

The insets in Figure 2 show the plots for the Zernike moment vectors at basis polynomial orders of 20 and 40 respectively for a reference library number 2. Vectors such as these from each image are used in reconstructing the image and subsequently computing the mean square errors. They are also used for comparing the score images to the reference library using similarity measures.

Figure 5.2 shows the cumulative mean square error plots for the numbers defaced off the stainless steel bar. From this plot it can be observed that the range of polynomial orders at which

the reconstruction error is minimized is similar and a consistent range can be used to capture the features from the score images of all the numbers.

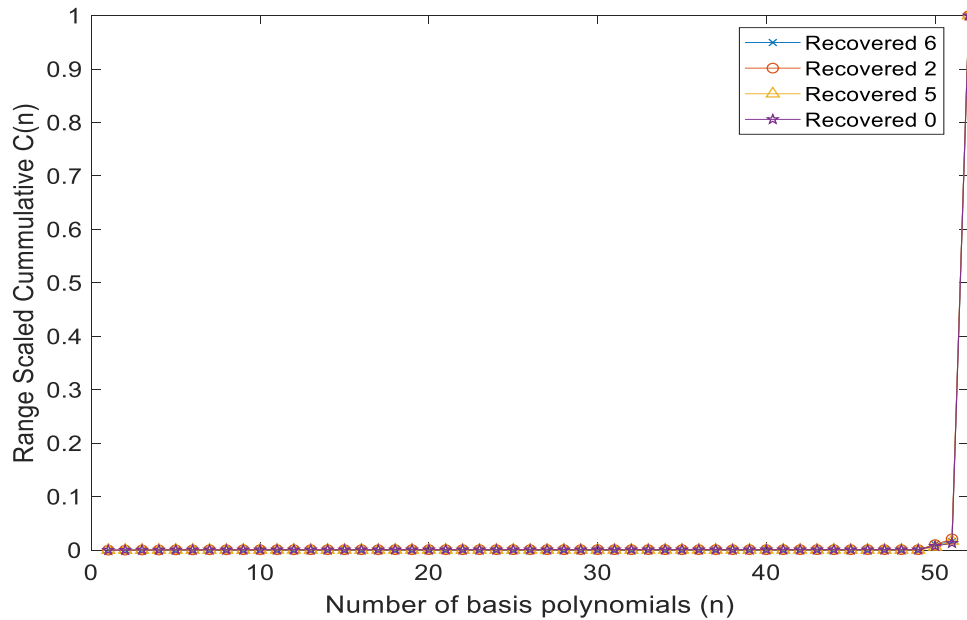


Figure 5.2: Cumulative mean square error difference for an increasing order of Zernike polynomials shown for four recovered numbers.

From both figures, it can be observed that the cumulative sum increases steadily until all major features have been captured and then it slowly increases indicating little change in the mean square errors for consecutive orders and subtle features are now being included. Ultimately, there is a sudden increase at higher orders indicating all image features have been captured and higher order polynomials are adding non-feature related elements and distorting the reconstructed image. From the plot, this increase occurs at order 51 and thus, it can be deduced that beyond order 50, the Zernike moment vectors will contain non-feature related elements that may impair the classification. This led to a selection of a range of orders between 15 and 50 in steps of 5 as polynomial orders for use in the classification of the recovered numbers.

Figure 5.3 shows the reconstruction of the recovered number ‘2’ from the stainless steel sample at some Zernike moment orders. From the images, it can be discerned that Zernike moments at the defined orders capture enough features to adequately reproduce the number, until at order 50 where although there is still enough detail captured to discern the number, the details begin to get obscured and higher orders further obscure details and no longer reproduce an identifiable number.

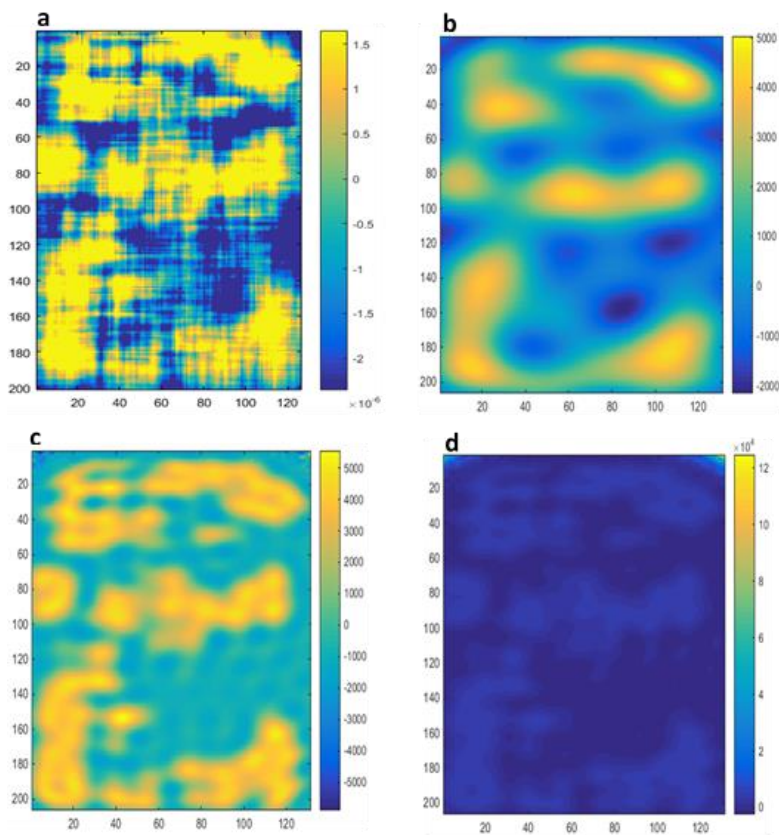


Figure 5.3: Images of a) original score image, and reconstructed images at Zernike moment orders b) 20, c) 45, d) 50.

As previously discussed in Chapter 3, all the score images developed for the area around a defaced number are used in the identification process irrespective of whether or not a number can be visually recognized in it. This is done to avoid the necessity of visually selecting a score image to use in identifying the defaced number, and also to utilize score images that might have

partial reproductions of the number to better identify the defaced number. Each score image is binarized to black and white as described in Chapter 3, ensuring similarity of type to the reference library image. All images (both score images and reference library images), are then preprocessed to make them scale and translation invariant before the Zernike moment vectors of each are extracted to be compared. The comparison is done using 15 similarity measures to compare each score image to each reference library image across 10 different font types, and a consensus of identification is obtained using fusion rules across all the resulting merit values.

Figure 5.4 shows the similarity merit values obtained from comparing each score image to all the reference library images across the 10 digits for the recovered numbers on the stainless steel sample. The lowest value in a row indicates the digit a particular similarity measure classifies a particular score image to. These results, obtained by comparing the images at the 8 different orders of Zernike moments for a total of 18000 merits show that there although some similarity merits accurately identify the recovered numbers, others do not. Several reasons could be attributed to this including some of the score images not capturing the thermal gradient to reproduce the defaced number, as well as some polynomial orders not capturing enough pertinent detail to match the recovered number images to some of the reference library images. This exemplifies the importance of using multiple similarity measures as a single similarity measure will give a limited perspective to identifying a dataset, and thus possibly inhibit the accuracy of the process.

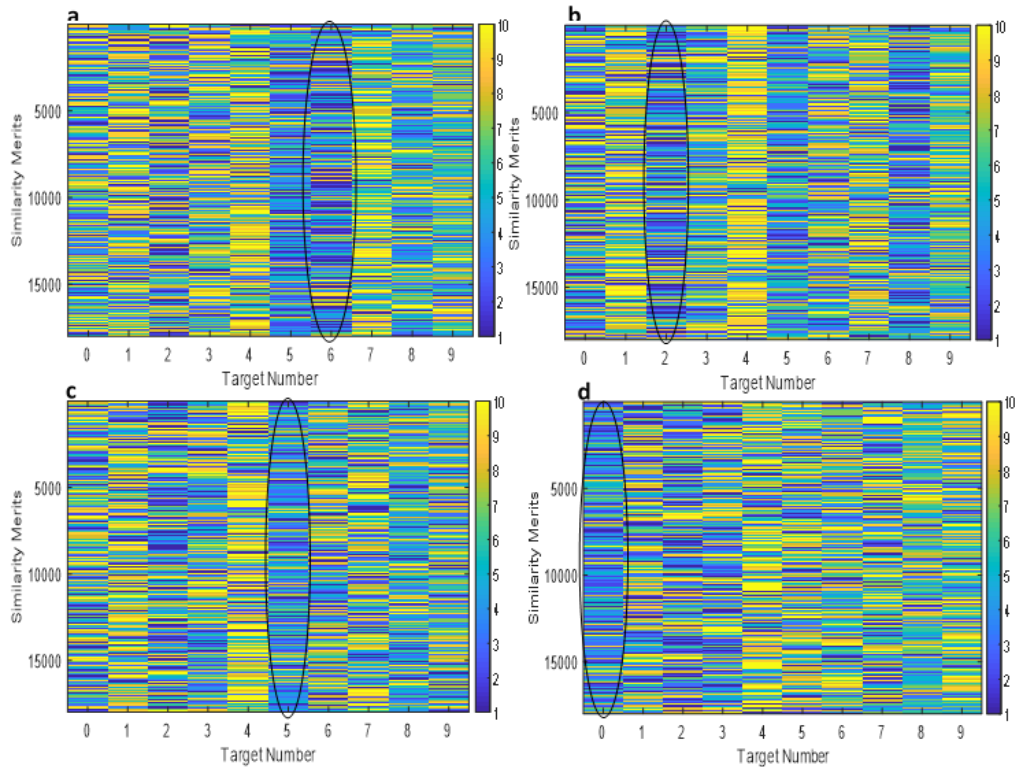


Figure 5.4: Similarity merits for all score images of recovered numbers a) six, b) two, c) five, and d) zero.

Figure 5.5 shows the results from the fusion of the similarity measures for each reference library font compared. The lowest value in a row indicate the digit the similarity measure classifies the dataset of score images to. The red lines section off the fusion results for each of the ten fonts in the order they are listed in Table 5.1.

From these results, it can be observed that some reference library fonts accurately classify some of the numbers and others do not. However, from the results for the four defaced numbers, it seems there is no singular consensus as to fonts that rightly classify all the score images. This further projects the importance of using several different fonts to avoid trying to determine a single ideal font that will accurately classify all recovered numbers.

Table 5.1: Fonts used in the reference library images.

Rows	Reference Library Font
1-14	Times New Roman
15-28	Times New Roman italics
29-42	Tempus Sans
43-56	Segoe Print
57-70	Gung Suh
71-84	Gung Suh italics
85-98	Arial Rounded MT
99-112	Arial Rounded MT italics
113-126	Arial Black
127-140	Arial Black italics

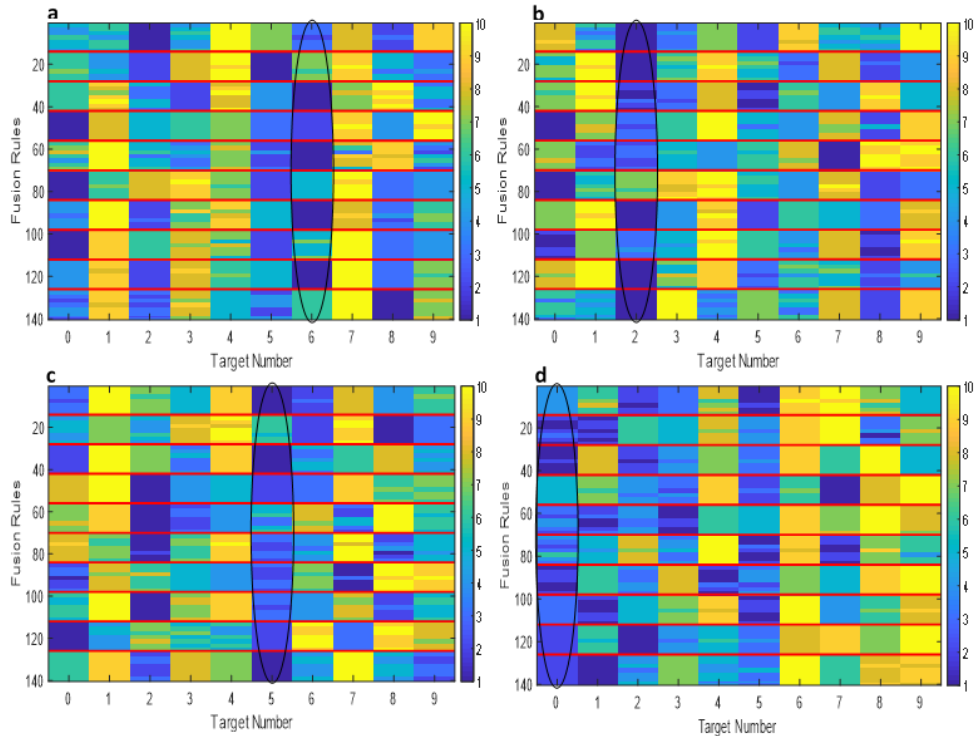


Figure 5.5: Results of fusion ranking for recovered numbers a) six, b) two, c) five, and d) zero.

Figures 5.6a to 5.6d images the results of each fusion rule applied across the merits from comparing the recovered numbers to each digit. These image gives a visual representation of the

results used to verify the identities of the recovered numbers. From the figures, it is seen that the process works efficiently in matching the recovered numbers, with most consistently having the lowest rank across all the fusion rules except for the recovered number ‘5’ where some of the fusion rules failed to accurately classify the number, possibly due to some score images being misidentified.

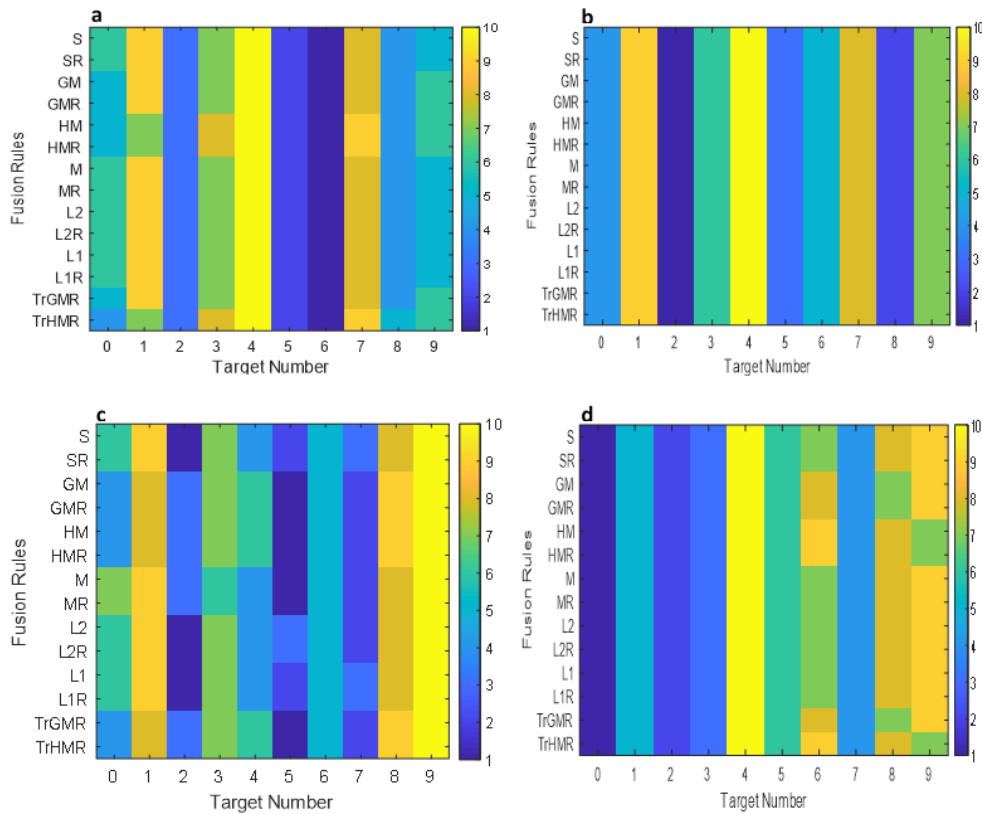


Figure 5.6: Image of fused merits from all fusion rules for the recovered numbers a) six, b) two, c) five, d) zero.

Tables 5.2 to 5.5 show the final results with using both majority vote and sum across the fusion rules. In order to correctly match a defaced number to a target number, the defaced number has to be ranked lowest by a majority vote of the fusion rules (8 of the 14 fusion rules) and have the lowest sum of the ranked fusion rule values. Otherwise, the defaced number is non-identifiable.

These tables reiterate the information in Figure 5.6 in showing that there is an overall consensus across all the fusion rules matching the recovered numbers ‘6’, ‘2’ and ‘0’. However, as seen in Table 5.04, for the identification of the defaced “5”, there is an increase in the sum across the fusion rule ranks due to some fusion rules not accurately classifying the number leading to a drop in the accuracy of the identification although it was still correctly identified. This highlights the necessity of utilizing a consensus among the fusion rules. Both the consensus methods applied correctly matched the recovered number to the right digit despite the contrasting results from some fusion rules.

Table 5.2: Fusion of similarity measure values for area around defaced number six.

Target Number	0	1	2	3	4	5	6	7	8	9
Majority Vote	6	9	3	7	10	2	1	8	4	5
Sum	77	120	42	101	140	28	14	115	57	76

Table 5.3: Fusion of similarity measure values for area around defaced number two.

Target Number	0	1	2	3	4	5	6	7	8	9
Majority Vote	5	0	1	8	10	2	4	0	0	7
Sum	72	115	14	112	138	36	52	87	38	106

Table 5.4: Fusion of similarity measure values for area around defaced number five.

Target Number	0	1	2	3	4	5	6	7	8	9
Majority Vote	0	9	3	7	4	1	5	2	8	10
Sum	74	120	30	96	68	22	70	32	118	140

Table 5.5: Fusion of similarity measure values for area around defaced number zero.

Target Number	0	1	2	3	4	5	6	7	8	9
Majority Vote	1	7	2	10	3	5	6	4	9	8
Sum	14	104	28	138	48	70	84	50	128	106

The results from using the Zernike moments to classify the recovered score images showed it to be a useful method in capturing features that describe an image well enough to allow for its identification. However, there was still a few inaccuracies in the identification which could be put down to using all the score images developed irrespective of whether they captured information that allowed for a visual identification of the number or not.

5.2. PSEUDO ZERNIKE MOMENTS

Similar to Zernike moments, pseudo Zernike moments also require the determination of a polynomial order or range of orders where all pertinent features of the images are captured and can be used to accurately reconstruct the image. The reconstruction errors are also used and the cumulative sum of differences plotted to determine the range of orders at which the image features are best captured. Figure 5.7 shows a plot of the cumulative sum of difference of errors for two of the images from the reference library alongside that of the defaced number 2. From these plots, it can be surmised that an identical range of orders adequately capture the features to allow for a recreation of both the score images and reference library images.

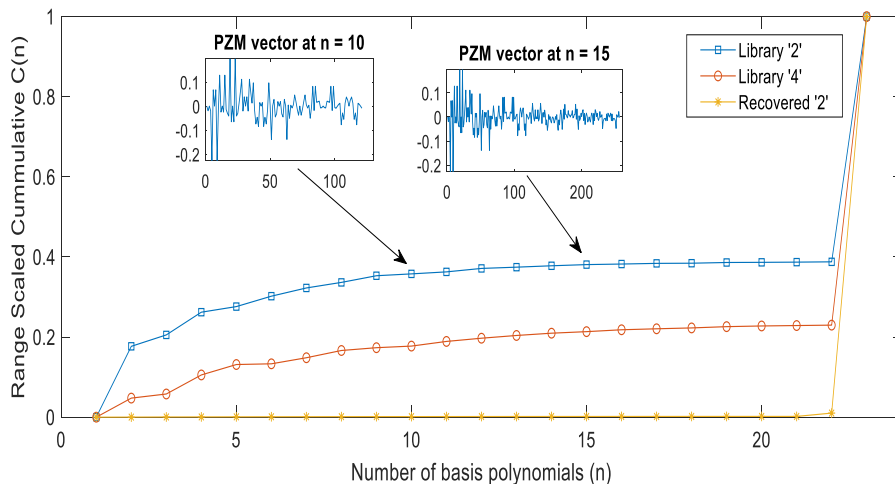


Figure 5.7: Cumulative mean square error difference for an increasing order of pseudo Zernike polynomials shown for two reference library images and recovered number '2'.

Figure 5.8 shows examples of the plots for score images of the defaced numbers on the stainless steel sample. From these plots, it can be deduced that a similar range of orders capture the features necessary to adequately reconstruct the images for all of the four numbers defaced from the stainless steel sample.

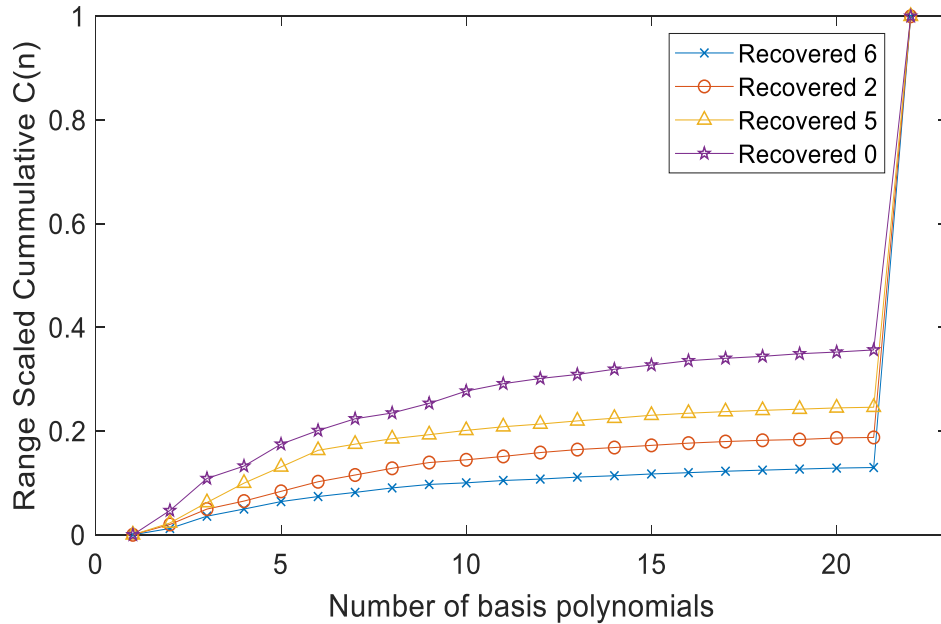


Figure 5.8: Cumulative mean square error difference for an increasing order of pseudo Zernike polynomials shown for four recovered numbers.

From the plots, it can be inferred that orders 4 through 20 adequately capture the features from the images, allowing for a reasonably accurate reproduction, leading to a low reconstruction error. As such, these orders were selected for use in generating the pseudo Zernike moments to be used in identifying the numbers. A similar process was used to the one used for Zernike moment except in one respect. In obtaining a consensus using the fusion rules, a thresholding operation was included as described in Chapter 3 to select only rows having the ratio of the two lowest similarity values equal to a defined threshold and each fusion rule is applied to the columns of the resulting matrix. This process is repeated for successively increasing values of the threshold (between 0.1 and 1 in steps of 0.05 for this study). The resulting fusion values for

all the thresholds set are then concatenated into a single 10 column matrix and the fusion rules applied again and a final consensus determined using majority vote and sum rules.

Figures 5.9a to 5.9d show the similarity merits obtained from comparing the pseudo Zernike moments at polynomial orders 4 through 20 in steps of 2 of the score images for the recovered numbers to those of the reference library images. A total of 20250 merits are obtained for each dataset (15 score images at 9 polynomial orders compared to 10 libraries using 15 similarity measures).

From these images, it can be observed that similar to the results from Zernike moments, some of the similarity merits correctly classify the defaced numbers but others do not. This can also be attributed to using all the score images irrespective of if the defaced number shows up in it or not and also the use of several polynomial orders, some of which may not capture pertinent features to adequately classify the score images. As such, using the fusion rules to accurately determine a consensus from the similarity merit values is necessary to properly identifying the defaced number.

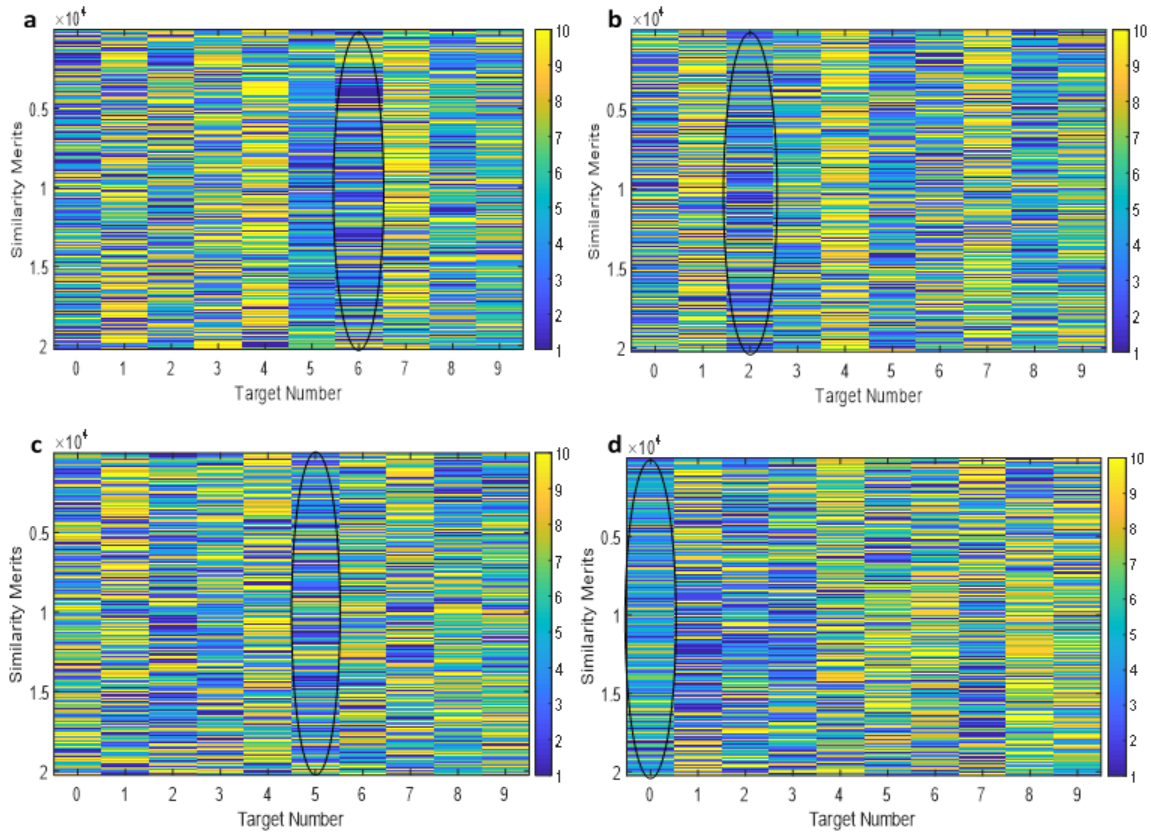


Figure 5.9: Similarity merits for all score images of recovered numbers a) six, b) two, c) five, and d) zero.

Figures 5.10a to 5.10d shows images of the results from using the fusion rules to obtain consensus among the similarity merits obtained for each reference library font. The red lines section off the fusion results for each of the fonts used. From the results, it can be observed that similar to the results from using Zernike moment vectors, some of the reference library font types correctly classified the defaced numbers while others misclassified them. As such, it is advantageous to use all the different font types in the reference library as it would be difficult to select particular font types that will work in all scenarios.

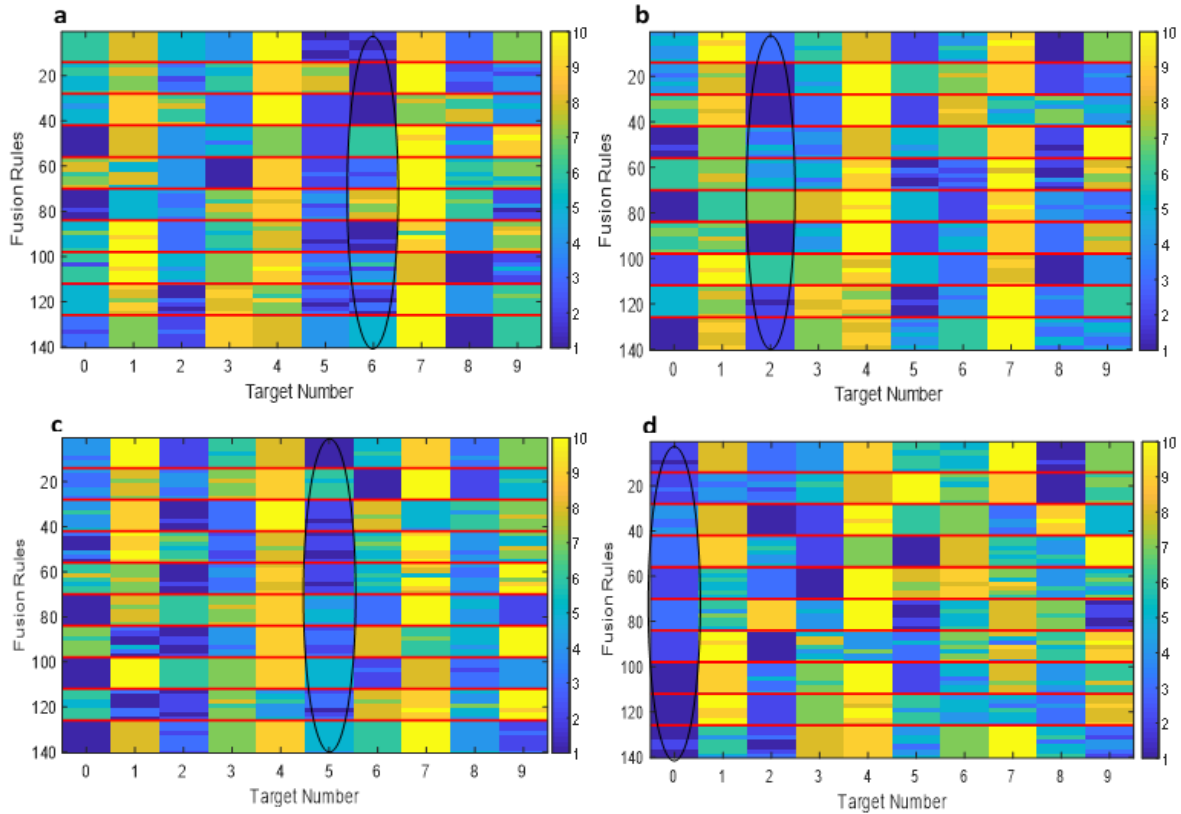


Figure 5.10: Results of fusion ranking for recovered numbers a) six, b) two, c) five, and d) zero.

Tables 5.6 to 5.9 show the results of applying each fusion rule across all the merits obtained from using the similarity measures to compare the recovered numbers from the stainless steel plate to the reference library. These results, obtained using feature vectors from pseudo Zernike moments compare favorably to those obtained using regular Zernike moments presented in Tables 5.2 to 5.5. The results for the number ‘5’ show an improvement in the identification with all the fusion rules accurately identifying the number. This indicates that the feature vectors from pseudo Zernike moments better characterized features in the images leading to an improved consensus across the fusion rules as to the identity of the number and thus reducing the uncertainty of the identification.

Table 5.6: Fusion of similarity measure values for area around defaced number six.

Target Number	0	1	2	3	4	5	6	7	8	9
Majority vote	3	8	4	6	9	2	1	10	5	7
Sum	48	112	50	84	126	28	14	140	70	98

Table 5.7: Fusion of similarity measure values for area around defaced number two.

Target Number	0	1	2	3	4	5	6	7	8	9
Majority vote	4	8	1	6	10	2	5	9	3	7
Sum	56	112	14	82	140	30	72	126	40	98

Table 5.8: Fusion of similarity measure values for area around defaced number five.

Target Number	0	1	2	3	4	5	6	7	8	9
Majority vote	3	8	2	6	10	1	5	9	4	7
Sum	42	112	28	84	138	14	70	128	56	98

Table 5.9: Fusion of similarity measure values for area around defaced number zero.

Target Number	0	1	2	3	4	5	6	7	8	9
Majority vote	1	9	2	3	10	5	7	6	4	8
Sum	14	122	28	43	140	71	98	81	57	116

Figures 5.11a to 5.11d show the images for the fusion rules used to extract consensus from the similarity merits for each of the recovered numbers. These images, consistent with the results shown in Tables 5.6 to 5.9, indicate that all the fusion rules accurately identified the defaced numbers.

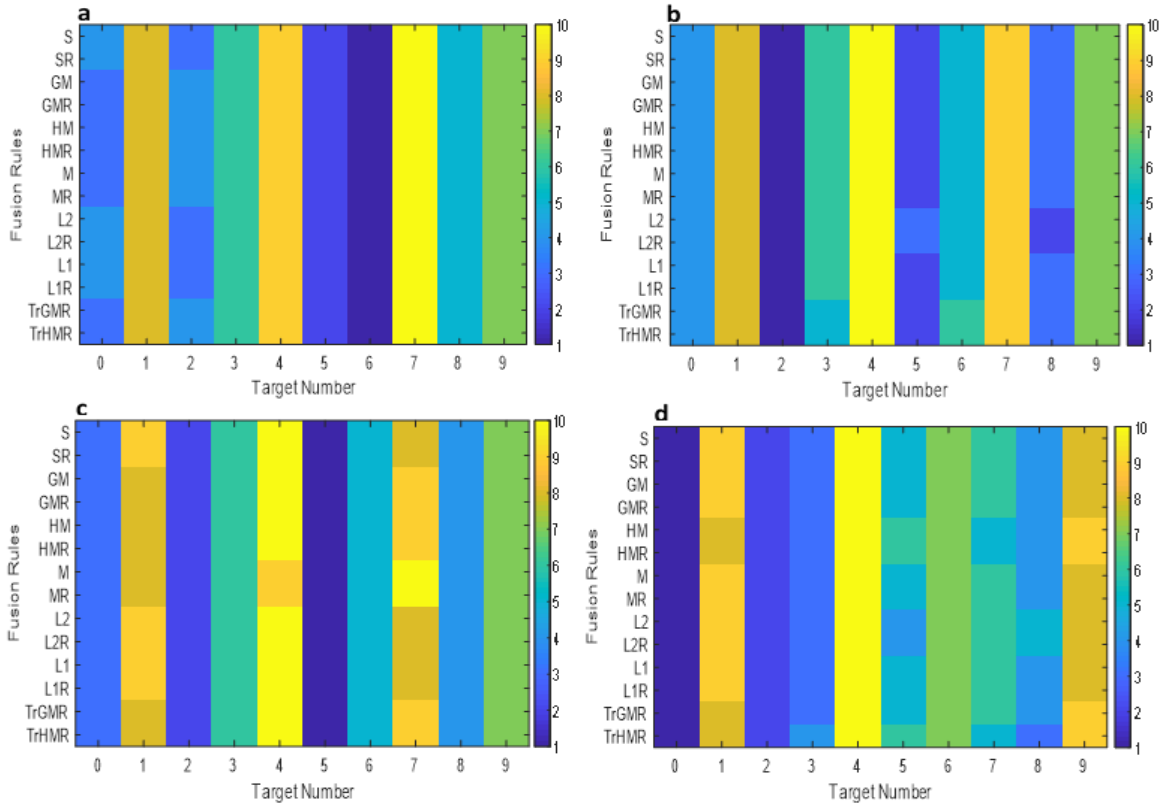


Figure 5.11: Image of fused merits from all fusion rules for the recovered numbers a) six, b) two, c) five, d) zero.

These results from using pseudo Zernike moments to identify the defaced numbers showed that this technique did improve the identification, indicating it to be a more robust technique for this type of data. As such, this method was used with the datasets for the other samples tested to attempt to identify the defaced numbers.

The similarity merits for the score images for the defaced serial numbers on the gun barrel at the different modulation frequencies tested are shown in Figures 5.12 and 5.13, for the defaced number '1' and number '2' respectively. The same computational protocol used with the stainless steel sample was used for these samples. However, with the increase in number of score images for these samples due to an additional pulsing cycle included at each modulation frequency, there is a concurrent increase in the number of similarity merits to 21600 merits.

From the images of all the similarity merits, some of the merits accurately identify the recovered numbers while others do not. As such, the fusion rules need to be applied to obtain a consensus from among these similarity merits.

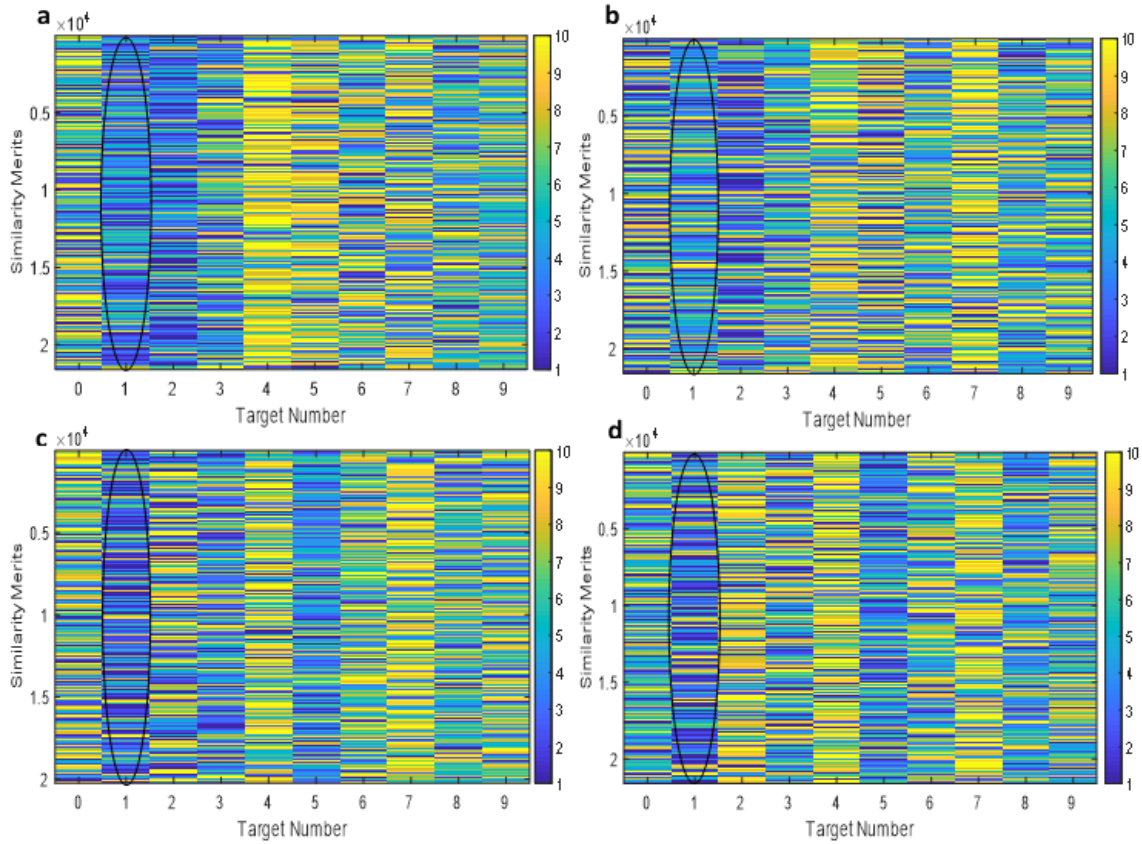


Figure 5.12: Similarity merits for all score images of defaced number '1' using modulation frequency a) 1 Hz, b) 0.125 Hz, c) 0.05 Hz, and d) 0.03125 Hz.

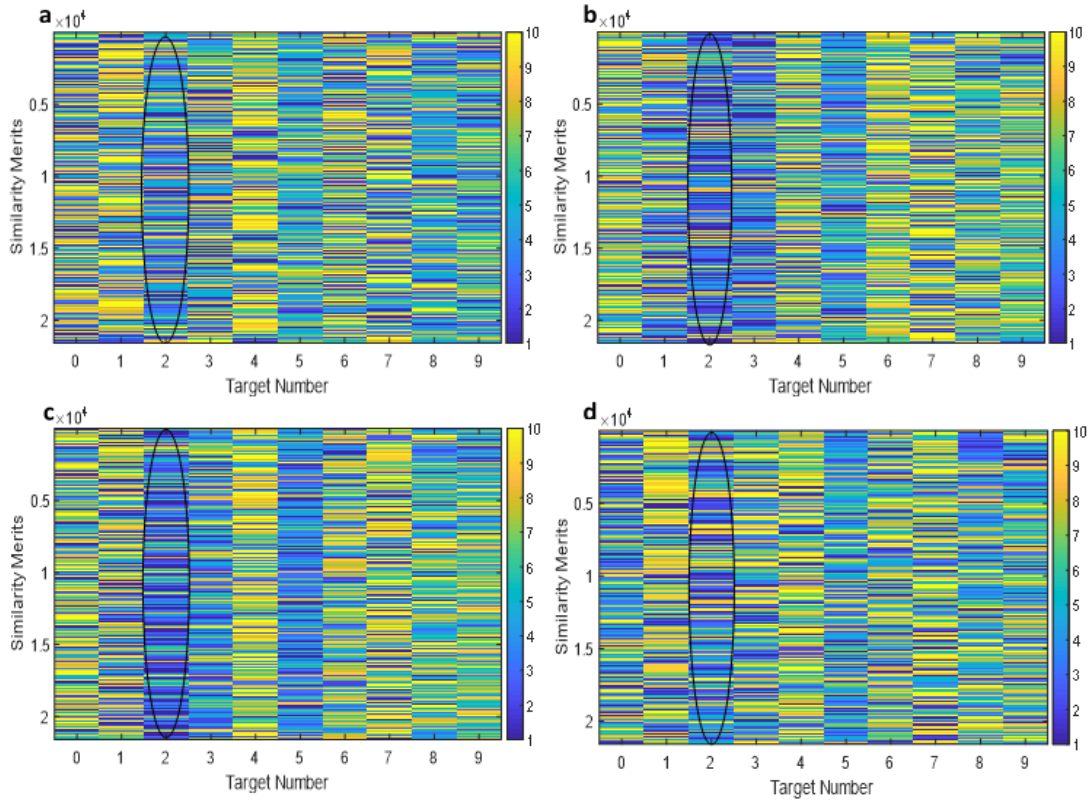


Figure 5.13: Similarity merits for all score images of defaced number ‘2’ using modulation frequency a) 1 Hz, b) 0.125 Hz, c) 0.05 Hz, and d) 0.03125 Hz.

Figures 5.14a and 5.14b show the results of applying fusion rules to the similarity merits obtained at each of the datasets from the different modulation frequencies used. The red lines on the figures delineate the results from the similarity merits at each frequency tested. These results show that although thermal images captured at all four modulation frequencies did capture the thermal gradient in the zone of plastic strain around the number, the score images at some are incorrectly classified probably due to variations in the quality of the score images. As such, using all four modulation frequencies together to determine a consensus match will avoid the need to attempt selecting an optimal frequency to use.

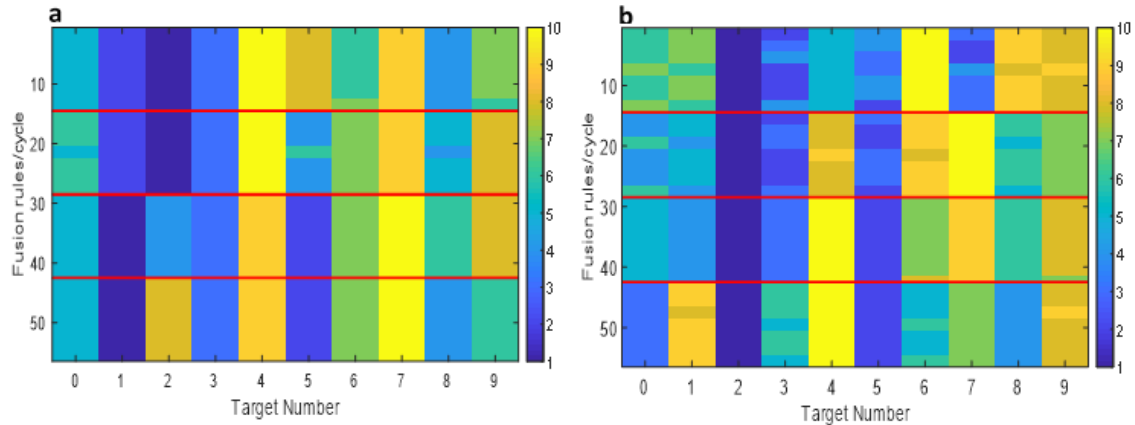


Figure 5.14: Image of fused merits from all fusion rules for the defaced numbers a) one, and b) two.

Tables 5.10 and 5.11 show the consensus results for the identification of the defaced numbers on the gun barrel. These were obtained by utilizing the fusion rules across the similarity merits from datasets at all modulation frequencies together. From these tables, the consensus results positively match the defaced numbers to their contemporaries in the reference library. This demonstrates the importance of such an identification protocol. Although the score images of the defaced numbers do not enhance the thermal gradients enough to visually identify the numbers, any uncertainties as to their identities can be eliminated by such independent verification.

Table 5.10: Fusion of similarity measure values for area around defaced number one.

Target Number	0	1	2	3	4	5	6	7	8	9
Majority vote	5	1	8	3	9	2	7	10	4	6
Sum	70	20	112	42	126	28	98	140	56	84

Table 5.11: Fusion of similarity measure values for area around defaced number two.

Target Number	0	1	2	3	4	5	6	7	8	9
Majority vote	3	9	1	6	10	2	5	7	4	8
Sum	42	124	14	80	140	28	74	98	56	114

Figures 5.15 and 5.16 show the similarity merits obtained by comparing the score images of the datasets from the needle holder at the different modulation frequencies tested, with the minimum value for each merit (each row in the images) representing the highest degree of matching. As with the previous results, some of the merits correctly classify the recovered numbers while others fail to do so, requiring the fusion rules to determine a consensus identification.

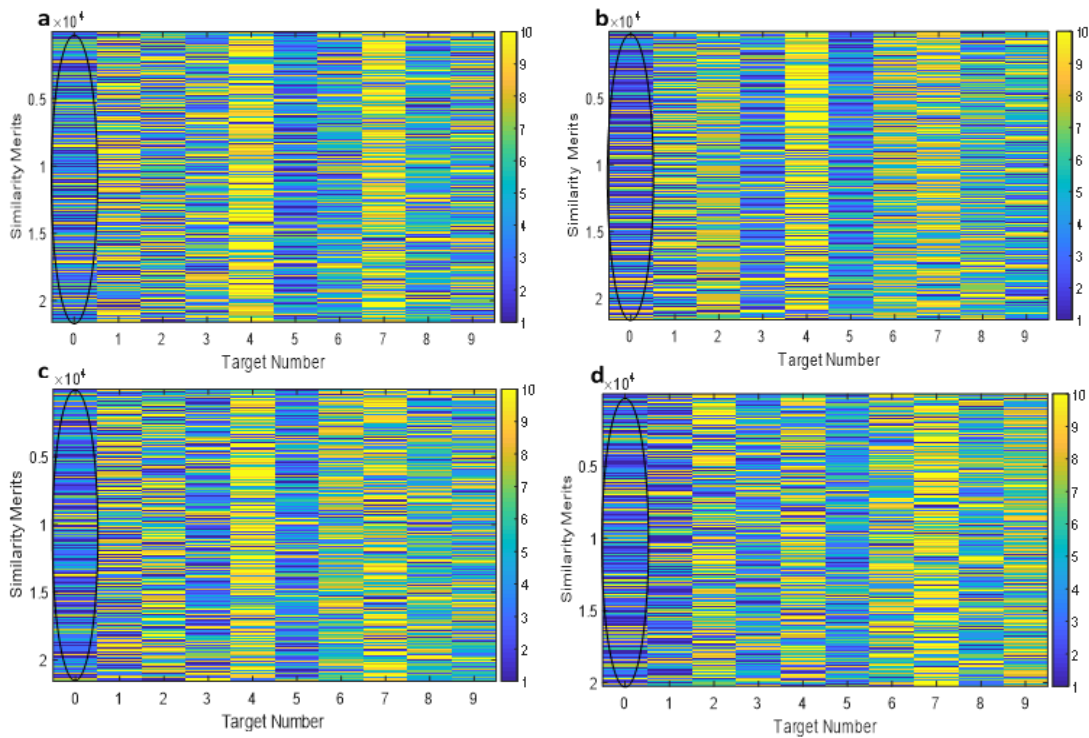


Figure 5.15: Similarity merits for all score images of defaced number ‘0’ using modulation frequency a) 1 Hz, b) 0.125 Hz, c) 0.05 Hz, and d) 0.03125 Hz.

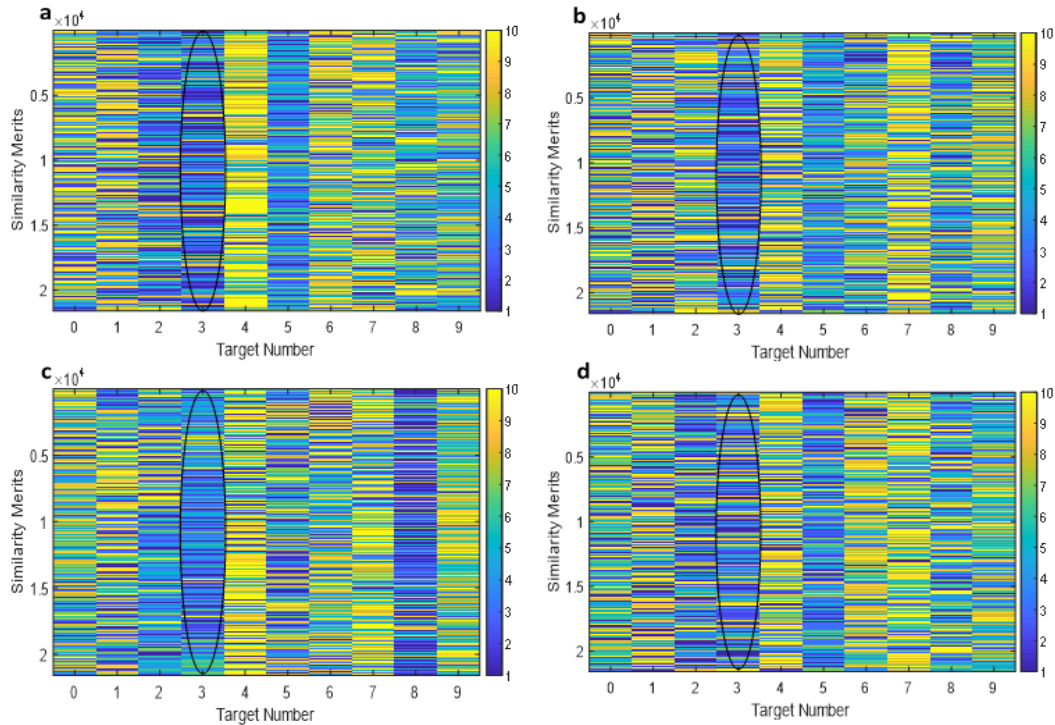


Figure 5.16: Similarity merits for all score images of defaced number '3' using modulation frequency a) 1 Hz, b) 0.125 Hz, c) 0.05 Hz, and d) 0.03125 Hz.

Figures 5.17a and 5.17b show the results from applying the fusion rules to the similarity merits at each of the modulation frequencies. These results show that although a visual interpretation of the score images indicates that all four modulation frequencies performed adequately well to capture the thermal gradient characteristic of areas beneath the defaced numbers, the score images at some of the frequencies were incorrectly classified. This further indicates the advantage of using score images from several modulation frequencies to make the identification, and avoid any need to select an ideal one.

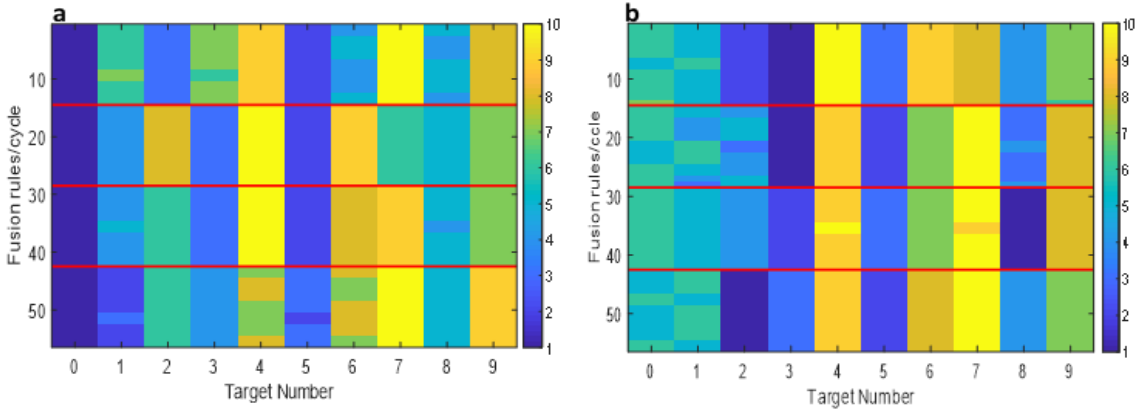


Figure 5.17: Image of fused merits from all fusion rules for the defaced numbers a) zero, and b) three.

Tables 5.12 and 5.13 show the final consensus results from the fusion rules applied across the similarity merits at all the modulation frequencies combined. From these results, it can be observed that although there was some misclassification of the score images at some of the frequencies in identifying the defaced number '3', the consensus still accurately identified the number, upholding the advantage of the fusion rules to accurately identify the defaced numbers.

Table 5.12: Fusion of similarity measure values for area around defaced number zero.

Target Number	0	1	2	3	4	5	6	7	8	9
Majority vote	1	2	6	4	7	3	8	10	5	9
Sum	14	30	84	56	104	40	106	140	70	126

Table 5.13: Fusion of similarity measure values for area around defaced number three.

Target Number	0	1	2	3	4	5	6	7	8	9
Majority vote	5	6	2	1	9	3	8	10	4	7
Sum	74	80	30	18	126	42	112	140	50	98

Figures 5.18a to 5.18i show the similarity merits obtained from applying the process to the score images of the defaced VIN numbers from the motorcycle fork. Consistent with the other samples tested, the minimum value across a similarity merit indicates the closest match between the image and the reference library image. Similar to the other samples, the similarity merits do not

consistently identify the defaced numbers precisely, with some accurately identifying the numbers and others failing to do so, necessitating the use of fusion rules to achieve a consensus identification as to the match.

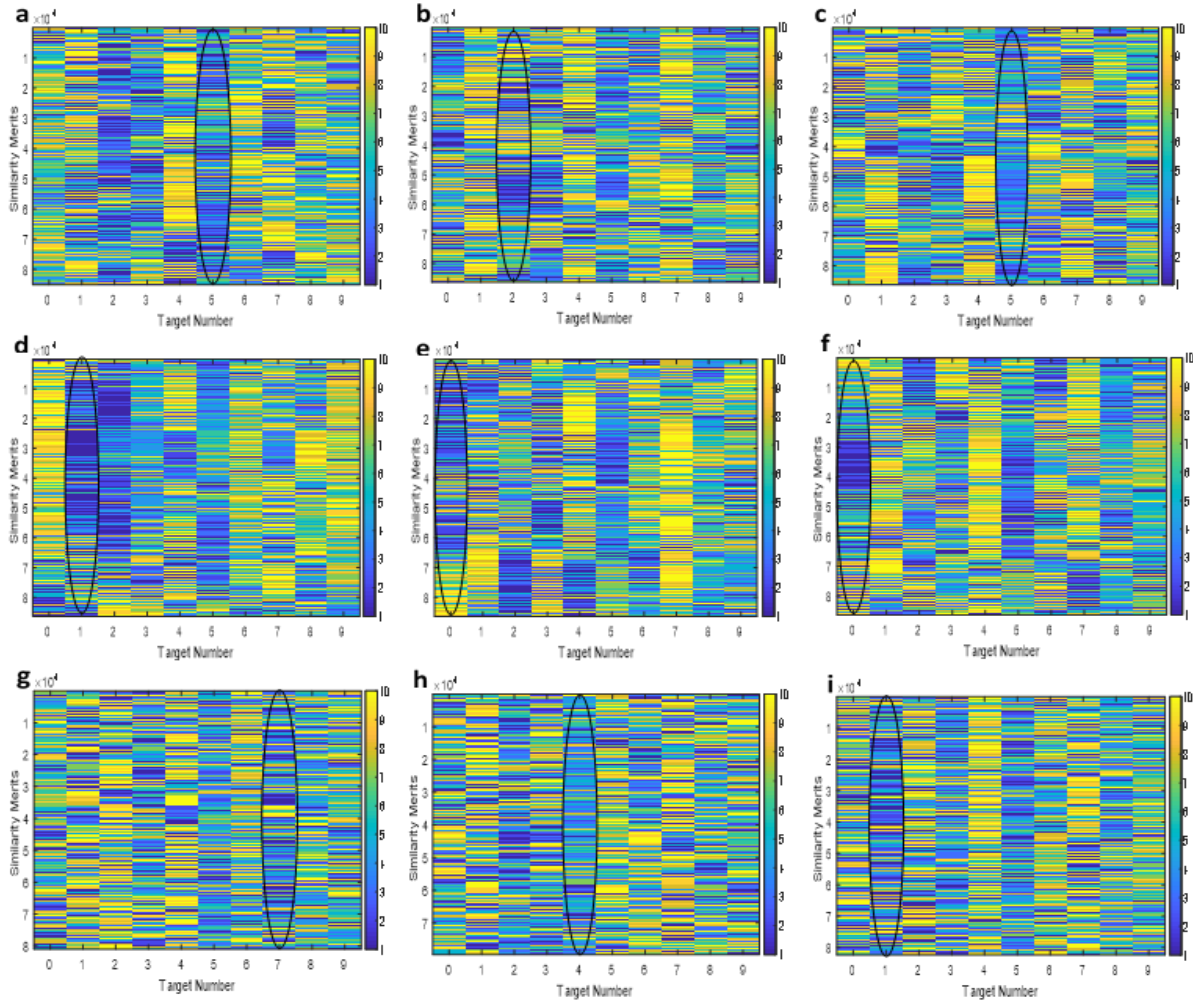


Figure 5.18: Similarity merits for all score images of recovered number a) five, b) two, c) five, d) one, e) unknown (presumed to be a 0), f) zero, g) unknown (presumed to be a 7), h) four, and i) one.

Table 5.14 shows the results of the consensus of identification for the motorcycle VIN. From these results, it is seen that using the methodology developed, the defaced serial numbers known from the non-defaced versions on the engine block were all accurately identified and the identities of unknown numbers confirmed.

Table 5.14: Fusion of similarity measure values for recovered numbers on motorcycle.

Target Number	5	2	5	1	0	0	7	4	1
Majority vote	1	1	1	1	1	1	1	1	1
Sum	16	16	14	14	14	16	22	20	18

From the results, it can be deduced that the recovered numbers can be identified when including the score images developed from all four modulation frequencies. This negates the need to select score images at a particular modulation frequency to use in the identification process.

5.3. CONFORMAL PREDICTION

As outlined in Chapter 3, the conformal prediction process used to assign confidence indices to the identification results, requires the use of nonconformity measures to assign these indices. Two nonconformity measures are tested in this study to determine which would be best suited for the data type generated from the fusion of similarity merits.

The results from the fusion of the similarity merits are used in this process to determine confidence indices for the identification of each of the recovered numbers. Although, there are a total of 14 fusion rules used, only those which utilize the actual merit values from similarity measures are used for conformal prediction. Those that require a ranking of the merits before use are left out. As such, 8 fusion rules are used culminating in obtaining 8 p-values. A consensus value is obtained among them by taking the average of all 8 values and the confidence level is determined from these average p-values.

5.3.1. Identification by Zernike Moments

Confidence and credibility indices are determined for the identification of the recovered numbers using the fusion results obtained by comparing Zernike moment feature vectors. The nearest neighbor algorithm is used as the nonconformity measure to develop p-values for these fusion data. The confidence index is obtained by subtracting the second highest average p-value from 1

and the credibility value is taken as the highest p-value. Tables 5.15 to 5.18 show the p-values for each fusion rule as well as the confidence and credibility indices determined from the average of the p-values for identification of the recovered numbers from the stainless steel sample.

Table 5.15: Conformal prediction results using nearest neighbor algorithm for defaced number 6 on stainless steel sample.

Fusion Rule	p_y									
	0	1	2	3	4	5	6	7	8	9
SR	0.01	0.01	0.01	0.01	0.01	0.01	1.00	0.03	0.03	0.03
GR	0.08	0.06	0.08	0.08	0.08	0.08	1.00	0.10	0.10	0.10
HR	0.01	0.03	0.01	0.01	0.01	0.01	1.00	0.03	0.03	0.03
MR	0.08	0.10	0.07	0.07	0.08	0.10	1.00	0.10	0.13	0.11
L2R	0.08	0.08	0.13	0.10	0.13	0.14	1.00	0.11	0.13	0.14
L1R	0.01	0.01	0.01	0.01	0.01	0.01	1.00	0.03	0.03	0.03
TrGM	0.08	0.10	0.10	0.10	0.11	0.11	1.00	0.13	0.13	0.11
TrHM	0.08	0.04	0.08	0.08	0.08	0.08	1.00	0.08	0.08	0.08
Average	0.06	0.05	0.06	0.06	0.07	0.07	1.00	0.07	0.08	0.08
Confidence Level (%)							92.01			
Credibility (%)							100.00			

Table 5.16: Conformal prediction results using nearest neighbor algorithm for defaced number 2 on stainless steel sample.

Fusion Rule	p_y									
	0	1	2	3	4	5	6	7	8	9
SR	0.03	0.03	1.00	0.01	0.01	0.01	0.03	0.03	0.01	0.03
GR	0.19	0.03	1.00	0.01	0.03	0.17	0.04	0.04	0.03	0.04
HR	0.19	0.03	1.00	0.01	0.03	0.15	0.06	0.06	0.04	0.04
MR	0.13	0.03	1.00	0.03	0.01	0.11	0.04	0.06	0.03	0.03
L2R	0.28	0.03	1.00	0.01	0.03	0.36	0.06	0.06	0.03	0.04
L1R	0.03	0.03	1.00	0.01	0.01	0.01	0.03	0.03	0.01	0.03
TrGM	0.03	0.03	1.00	0.01	0.01	0.01	0.03	0.03	0.01	0.03
TrHM	0.04	0.03	1.00	0.01	0.01	0.03	0.04	0.04	0.01	0.03
Average	0.11	0.03	1.00	0.02	0.02	0.11	0.04	0.04	0.02	0.03
Confidence Level (%)			88.54							
Credibility (%)			100.00							

Table 5.17: Conformal prediction results using nearest neighbor algorithm for defaced number 5 on stainless steel sample.

Fusion Rule	p_y									
	0	1	2	3	4	5	6	7	8	9
SR	0.01	0.03	0.01	0.03	0.01	1.00	0.03	0.03	0.03	0.01
GR	0.56	0.07	0.18	0.07	0.08	1.00	0.10	0.42	0.06	0.06
HR	0.08	0.04	0.10	0.06	0.04	1.00	0.06	0.40	0.04	0.01
MR	0.07	0.01	0.08	0.03	0.03	1.00	0.03	1.00	0.01	0.01
L2R	0.43	0.11	0.39	0.10	0.11	1.00	0.13	0.58	0.07	0.08
L1R	0.01	0.03	0.01	0.03	0.01	1.00	0.03	0.03	0.03	0.01
TrGM	0.11	0.03	0.13	0.04	0.03	1.00	0.04	0.60	0.03	0.01
TrHM	0.10	0.07	0.08	0.06	0.04	1.00	0.06	0.35	0.04	0.04
Average	0.17	0.05	0.12	0.05	0.05	1.00	0.06	0.43	0.04	0.03
Confidence Level (%)						57.47				
Credibility (%)						100.00				

Table 5.18: Conformal prediction results using nearest neighbor algorithm for defaced number 0 on stainless steel sample.

Fusion Rule	p_y									
	0	1	2	3	4	5	6	7	8	9
SR	1.00	0.03	0.03	0.03	0.03	0.03	0.01	0.03	0.03	0.03
GR	1.00	0.03	0.24	0.03	0.03	0.04	0.01	0.25	0.03	0.03
HR	1.00	0.04	0.22	0.04	0.07	0.11	0.03	0.19	0.04	0.04
MR	1.00	0.06	0.18	0.03	0.10	0.13	0.06	0.18	0.03	0.04
L2R	1.00	0.03	0.03	0.03	0.06	0.15	0.01	0.28	0.03	0.03
L1R	1.00	0.03	0.03	0.03	0.03	0.03	0.01	0.03	0.03	0.03
TrGM	1.00	0.04	0.14	0.04	0.03	0.06	0.03	0.13	0.04	0.04
TrHM	1.00	0.04	0.11	0.04	0.03	0.04	0.03	0.11	0.04	0.04
Average	1.00	0.04	0.12	0.03	0.05	0.07	0.02	0.15	0.03	0.03
Confidence Level (%)	85.07									
Credibility (%)	100.00									

From the data in Table 5.15, using the nearest neighbor algorithm, the confidence level of classification of the defaced number as a 6 is 92%. The process also gives a credibility value which is an indicator of the suitability of the nonconformity measure for the type of data in use, and thus its value illustrates the validity of the confidence index. As such, the high credibility

value (in this case 100%) shows that the nearest neighbor algorithm is a good nonconformity measure to use in determining a confidence index for the fusion values identifying the number. This credibility value is determined as the p-value of the class to which the defaced number is matched to by the fusion rules.

Tables 5.16 to 5.18 show the confidence levels obtained for the fusion of merits for the other recovered numbers on the stainless steel sample. The confidence indices for the defaced numbers 2 and 0 were quite good (88% and 85% respectively). However, the confidence index for the defaced 5 was just over 50%, which can be attributed to the misclassification of the number by some of the fusion rules. This shows that conformal prediction does give a reasonably accurate depiction of the results obtained from the fusion of the merits as any uncertainty in the identification process is captured in the final confidence level assigned to the identification made.

Tables 5.19 to 5.22 show the results of using the second nonconformity measure (distance to average) to determine confidence indices for the identification of the recovered numbers from the stainless steel sample.

Table 5.19: Conformal prediction results using distance to average algorithm for defaced number 6 on stainless steel sample.

Fusion Rule	P_y									
	0	1	2	3	4	5	6	7	8	9
SR	0.01	0.01	0.01	0.01	0.01	0.01	0.96	0.01	0.01	0.01
GR	0.01	0.01	0.01	0.01	0.01	0.01	0.96	0.01	0.01	0.01
HR	0.01	0.01	0.01	0.01	0.01	0.01	0.88	0.01	0.01	0.01
MR	0.01	0.01	0.01	0.01	0.01	0.01	0.68	0.01	0.01	0.01
L2R	0.01	0.01	0.01	0.01	0.01	0.01	0.78	0.01	0.01	0.01
L1R	0.01	0.01	0.01	0.01	0.01	0.01	0.96	0.01	0.01	0.01
TrGM	0.01	0.01	0.01	0.01	0.01	0.01	0.93	0.01	0.01	0.01
TrHM	0.01	0.01	0.01	0.01	0.01	0.01	1.00	0.01	0.01	0.01
Average	0.01	0.01	0.01	0.01	0.01	0.01	0.89	0.01	0.01	0.01
Confidence Level (%)							98.61			
Credibility (%)							89.24			

Table 5.20: Conformal prediction results using distance to average algorithm for defaced number 2 on stainless steel sample.

Fusion Rule	P_y									
	0	1	2	3	4	5	6	7	8	9
SR	0.04	0.01	0.57	0.01	0.01	0.07	0.01	0.01	0.01	0.01
GR	0.03	0.01	0.96	0.01	0.01	0.06	0.01	0.01	0.01	0.01
HR	0.03	0.01	0.90	0.01	0.01	0.04	0.01	0.01	0.01	0.01
MR	0.01	0.01	0.31	0.01	0.01	0.03	0.01	0.01	0.01	0.01
L2R	0.07	0.01	0.31	0.01	0.01	0.14	0.01	0.01	0.01	0.01
L1R	0.04	0.01	0.57	0.01	0.01	0.07	0.01	0.01	0.01	0.01
TrGM	0.03	0.01	0.60	0.01	0.01	0.04	0.01	0.01	0.01	0.01
TrHM	0.03	0.01	0.61	0.01	0.01	0.03	0.01	0.01	0.01	0.01
Average	0.03	0.01	0.60	0.01	0.01	0.06	0.01	0.01	0.01	0.01
Confidence Level (%)			94.10							
Credibility (%)			60.24							

Table 5.21: Conformal prediction results using distance to average algorithm for defaced number 5 on stainless steel sample.

Fusion Rule	P _y									
	0	1	2	3	4	5	6	7	8	9
SR	0.07	0.01	0.93	0.01	0.04	0.49	0.03	0.50	0.01	0.01
GR	0.03	0.01	0.39	0.01	0.03	0.99	0.03	0.88	0.01	0.01
HR	0.03	0.01	0.17	0.01	0.01	0.54	0.01	0.44	0.01	0.01
MR	0.03	0.01	0.14	0.01	0.01	0.40	0.01	0.39	0.01	0.01
L2R	0.07	0.03	0.35	0.03	0.04	0.15	0.04	0.14	0.01	0.01
L1R	0.07	0.01	0.93	0.01	0.04	0.49	0.03	0.50	0.01	0.01
TrGM	0.03	0.01	0.14	0.01	0.01	0.39	0.01	0.28	0.01	0.01
TrHM	0.03	0.01	0.10	0.01	0.01	0.25	0.01	0.19	0.01	0.01
Average	0.04	0.02	0.39	0.02	0.03	0.46	0.02	0.41	0.01	0.01
Confidence Level (%)							58.51			
Credibility (%)							46.18			

Table 5.22: Conformal prediction results using distance to average algorithm for defaced number 0 on stainless steel sample.

Fusion Rule	P _y									
	0	1	2	3	4	5	6	7	8	9
SR	0.19	0.01	0.25	0.01	0.04	0.04	0.01	0.61	0.01	0.01
GR	0.92	0.01	0.58	0.01	0.01	0.01	0.01	0.08	0.01	0.01
HR	0.31	0.01	0.22	0.01	0.01	0.01	0.01	0.04	0.01	0.01
MR	0.07	0.01	0.04	0.01	0.01	0.01	0.01	0.01	0.01	0.01
L2R	0.03	0.01	0.01	0.01	0.14	0.18	0.01	0.17	0.01	0.01
L1R	0.19	0.01	0.25	0.01	0.04	0.04	0.01	0.61	0.01	0.01
TrGM	0.24	0.01	0.11	0.01	0.01	0.01	0.01	0.04	0.01	0.01
TrHM	0.15	0.01	0.07	0.01	0.01	0.01	0.01	0.04	0.01	0.01
Average	0.26	0.01	0.19	0.01	0.04	0.04	0.01	0.20	0.01	0.01
Confidence Level (%)	79.86									
Credibility (%)	26.22									

From the above tables, using the distance to average algorithm gives confidence indices quite similar those obtained from the nearest neighbor algorithm. However, there is a steep drop in the

credibility indices for some of the recovered numbers (2, 5 and 0). This discrepancy in the credibility values for the nonconformity measures can be attributed to the method of calculating p-values for each nonconformity measure. While the nearest neighbor algorithm determines the smallest distance of the data point under consideration to the data points in a class, the distance to average determines its distance from the mean of the data points within a class. As such, the distance to average algorithm is generally more sensitive to outlying data points irrespective of whether they belong to a certain class or not and this is reflected in the credibility values.

5.3.2. Identification by Pseudo Zernike Moments

The same process was employed to determine confidence indices for the datasets when identified using feature vectors extracted via pseudo Zernike moments. Table 5.23 gives a summary of the results with the confidence indices for each of the classified numbers on the stainless steel sample.

Table 5.23: Conformal Prediction Results for stainless steel sample.

Number	Nearest Neighbor		Dist. To Average	
	Confidence (%)	Credibility (%)	Confidence (%)	Credibility (%)
6	84.90	100.00	28.13	76.22
2	86.11	100.00	24.13	81.77
5	86.63	100.00	25.35	81.77
0	84.20	100.00	23.96	76.56

From the results, it can be observed that there is an increase in the confidence index using the nearest neighbor algorithm for the recovered number 5 compared to the results from the classification using Zernike moments. This can be traced back to the improved classification results obtained when using pseudo Zernike moments to classify the recovered 5.

However, there is a general drop in the results for the distance to average algorithm with both the confidence indices and credibility percentages reduced. This can be attributed to this method's

sensitivity to outliers, and as such its sensitivity to data determined using very different computational techniques as is the case with the fusion rules. As such, the distance to average algorithm may not be a good nonconformity measure to use in determining confidence indices from the results of the identification process. Tables 5.24 to 5.26 present the results of using both nonconformity measures to determine confidence indices for the recovered numbers on the other samples tested.

Table 5.24: Conformal Prediction Results for the gun barrel sample.

Number	Nearest Neighbor		Distance to average	
	Confidence (%)	Credibility (%)	Confidence (%)	Credibility (%)
1	96.53	100.00	13.72	89.41
2	95.83	100.00	15.97	87.85

Table 5.25: Conformal Prediction Results for the laser engraved needle holder.

Number	Nearest Neighbor		Distance to average	
	Confidence (%)	Credibility (%)	Confidence (%)	Credibility (%)
0	96.53	91.67	13.89	89.41
3	93.92	100.00	27.08	77.26

Table 5.26: Conformal Prediction Results for the motorcycle VIN.

Number	Nearest Neighbor		Distance to average	
	Confidence (%)	Credibility (%)	Confidence (%)	Credibility (%)
5	72.05	100.00	17.36	82.99
2	96.18	95.83	16.15	87.85
5	77.08	100.00	23.96	76.91
1	79.17	100.00	28.99	77.60
0	75.52	95.83	19.97	83.51
0	83.85	100.00	28.82	75.00
7	96.01	100.00	19.79	86.98
4	88.89	100.00	28.99	77.60
1	72.92	100.00	28.47	75.00

From the results, it would seem that there is a general trend of high confidence indices for the classified numbers when using the nearest neighbor algorithm and much lower indices when using the distance to average algorithm. This further reinforces the inference that the distance to average algorithm is not a good nonconformity measure to use for the datasets particularly because each fusion rule utilizes a different method to determine a consensus value from among the similarity merits. As such, they could theoretically result in widely varying values, and the distance to average algorithm being sensitive to such data spreads is inadequate for determining the fit of the data.

CHAPTER 6

6.0. CONCLUSION

A major challenge leading up to this study was the destructive nature of current serial number restoration techniques. This study proposed and developed a nondestructive alternative for use in the restoration process. The process, involving recovering the defaced numbers via infrared thermography and identifying the recovered numbers by comparing the developed score images to images of digits in a reference library is tested on several specimens. These included simulated mechanically stamped samples and a laser engraved sample as well as a real case scenario involving a stolen and recovered motorcycle with its VIN removed. The developed process successfully recovered the serial numbers utilizing LIT to capture thermal gradient differences in the zone of plastic strain and PCA to identify this local change in thermal gradient as a unique feature in the amplitude and phase images, and thus reproduce the number in a score image. Invariant features were extracted from the score images as well as the reference library images using two methods (Zernike moments and pseudo Zernike moments) and used to classify the images, leading to an identification of the recovered numbers. This process ensures both nondestructive and as such repeatable recovery of defaced serial numbers and identification of the numbers independent of possible human bias. A method to assign confidence indices to the identification results, and as such accord a measure of accuracy for the results is also presented. This method, conformal prediction is particularly useful for determining confidence intervals as it requires no prior knowledge of the distribution of the data.

With the success of the process in the samples tested, this nondestructive process shows potential for use as an alternative to or as a precursor to the established methods. The tests carried out using the process indicate it to a valid process that could be used for varying scenarios including mechanically stamped pieces or laser engraved pieces. The process is also quite flexible with

several independent parts, allowing for further testing and possible optimization of each part. Also in using multiple reference library fonts and testing with several similarity measures, the identification section is made quite flexible allowing for use with a wide variety of recovered stamp marks.

This dissertation in overcoming several challenges associated with developing a non-destructive method for the recovery of defaced serial numbers has helped advance the field in a few ways as itemized below.

- A novel approach combining lock-in infrared thermography (LIT) and image processing (PCA) was developed to address the challenge of detecting very small thermal gradients expected to occur due to deformation of the crystalline structure within the zone of plastic strain and HAZ.
- Another novel process of combining several similarity measures to identify the defaced number and then appending a confidence index to the identification using conformal prediction, was developed to overcome possible bias in the identification process and quantify the accuracy of the identification process.

6.1. FUTURE WORK

This study provides the basis for a nondestructive method of recovering defaced serial number. However, the process is dependent on a number of variables and work continues to optimize these and eliminate some of the uncertainties. Future work on optimizing this process could include:

- Fine tuning the data collection process, and possibly the testing of other thermography methods to determine the most efficient method of collecting thermal images to recover the defaced number.

- Testing other feature extraction techniques and similarity measures to determine the best for use in classifying the recovered numbers.
- Testing other nonconformity measures to determine the best method of applying confidence indices to the classification.

REFERENCE

- [1] L. Nickolls, *The scientific investigation of crime*, Butterworth, London, 1956.
- [2] T. and F. (ATF) Bureau of Alcohol, ATF quarterly bulletin 2001 volume 3 treasury decision, (n.d.). <https://www.atf.gov/resource-center/docs/report/atf-quarterly-bulletin-2001-volume-3---subpart-c---firearms/download> (accessed October 1, 2018).
- [3] E. Stauffer, M.S. Bonfanti, *Forensic investigation of stolen-recovered and other crime-related vehicles*, Elsevier/Academic Press, 2006.
- [4] D.E. Polk, B. Giessen, Metallurgical aspects of serial number recovery, *AFTE J.* 21 (1989) 174–181.
- [5] A.G. Guy, *Elements of physical metallurgy*, Oxford And Ibh Publishing Co.; Calcutta, 1960.
- [6] G. Peeler, S. Gutowski, S. Wrobel, The Restoration of Impressed Characters on Aluminum Alloy Motorcycle Frames, *J. Forensic Identif.* 58 (2008) 27–32.
- [7] P.B. Wilson, The Restoration of Erased Serial Identification Marks, *Police J. Theory, Pract. Princ.* 52 (1979) 233–242. doi:10.1177/0032258X7905200304.
- [8] M. Okayasu, K. Sato, M. Mizuno, A new etching technique for revealing the plastic deformation zone in an Al–Cu–Mg alloy, *J. Mater. Sci.* 43 (2008) 2792–2798.
- [9] M.A.M. Zaili, R. Kuppaswamy, H. Harun, Restoration of engraved marks on steel surfaces by etching technique, *Forensic Sci. Int.* 171 (2007) 27–32.
- [10] J.I. Thornton, P.J. Cashman, The mechanism of the restoration of obliterated serial numbers by acid etching, *J. Forensic Sci. Soc.* 16 (1976) 69–71.
- [11] G. Wightman, J. Matthew, Restoration of stamp marks on steel components, *Forensic Sci. Int.* 180 (2008) 32–36. doi:10.1016/J.FORSCIINT.2008.06.017.
- [12] R.S. Treptow, C.S. University, D. of P. Sciences, U.S. of America, *Methods for the Restoration of Obliterated Serial Numbers*, National Institute of Justice, 1977.
- [13] P.J. Shull, *Nondestructive evaluation: theory, techniques, and applications*, CRC press, 2016.
- [14] A. Killey, J.P. Sargent, Analysis of thermal nondestructive testing, *J. Phys. D. Appl. Phys.* 22 (1989) 216–224. doi:10.1088/0022-3727/22/1/032.
- [15] A.J. Çengel, Yunus A.; Ghajar, *Heat and Mass Transfer: Fundamentals & Applications*, McGraw-Hill Higher Education, 2015.
- [16] M. Choi, K. Kang, J. Park, W. Kim, K. Kim, Quantitative determination of a subsurface defect of reference specimen by lock-in infrared thermography, *NDT E Int.* 41 (2008) 119–124. doi:10.1016/J.NDTEINT.2007.08.006.
- [17] K. Cramer, P. Howell, H. Syed, Quantitative thermal imaging of aircraft structures, in: *Thermosense XVII An Int. Conf. Therm. Sens. Imaging Diagnostic Appl.*, 1995: pp. 226–233.

- [18] C.R. Dalton, B.W. Olson, F.C. Lai, Nondestructive evaluation of surface defects using scanning infrared thermography, *J. Thermophys. Heat Transf.* 23 (2009) 716–724.
- [19] G.S. Klees, The restoration or detection of obliterated laser-etched firearm markings by scanning electron microscopy and x-ray mapping, *AFTE J.* 41 (2009) 184–187.
- [20] C.M. Sayers, Detectability of Defects by Thermal Non-Destructive Testing.(Retroactive Coverage), *Br. J. Non-Destr. Test.* 26 (1984) 28–33.
- [21] O. Breitenstein, W. Warta, M. Langenkamp, *Lock-in Thermography - Basics and Use for Evaluating Electronic Devices and Materials*, Berlin/ Heidelberg: Springer, 2010. doi:10.1007/978-3-642-02417-7.
- [22] A. Gleiter, C. Spießberger, G. Busse, Lockin thermography with optical or ultrasound excitation, *J. Mech. Eng.* (2010) 619–924.
- [23] O. Breitenstein, C. Schmidt, D. Karg, Thermal failure analysis by IR lock-in thermography, *Microelectron. Fail. Anal. Desk Ref. Fifth Ed. EDFAS.* (2004).
- [24] W. Bai, B.S. Wong, Evaluation of defects in composite plates under convective environments using lock-in thermography, *Meas. Sci. Technol.* 12 (2001) 142–150. doi:10.1088/0957-0233/12/2/303.
- [25] H. Liu, Y. Wang, J. Liu, H. Gong, Effect of modulation frequency on detecting defects of metal plates using infrared lock-in thermography, in: 4th Int. Symp. Adv. Opt. Manuf. Test. Technol. Opt. Test Meas. Technol. Equip., International Society for Optics and Photonics, 2009: p. 72833M.
- [26] C. Ibarra-Castanedo, J.-M. Piau, S. Guilbert, N.P. Avdelidis, M. Genest, A. Bendada, X.P. V Maldague, Comparative study of active thermography techniques for the nondestructive evaluation of honeycomb structures, *Res. Nondestruct. Eval.* 20 (2009) 1–31.
- [27] A. Manohar, Quantitative nondestructive testing using infrared thermography, (2012).
- [28] I.T. Jolliffe, *Principal component analysis*, Springer, 2002.
- [29] N. Rajic, Principal component thermography for flaw contrast enhancement and flaw depth characterisation in composite structures, *Compos. Struct.* 58 (2002) 521–528.
- [30] J.M. Prats-Montalbán, A. de Juan, A. Ferrer, Multivariate image analysis: A review with applications, *Chemom. Intell. Lab. Syst.* 107 (2011) 1–23. doi:10.1016/J.CHEMOLAB.2011.03.002.
- [31] M. Kamruzzaman, G. ElMasry, D.-W. Sun, P. Allen, Prediction of some quality attributes of lamb meat using near-infrared hyperspectral imaging and multivariate analysis, *Anal. Chim. Acta.* 714 (2012) 57–67. doi:10.1016/J.ACA.2011.11.037.
- [32] S. Chevallier, D. Bertrand, A. Kohler, P. Courcoux, Application of PLS-DA in multivariate image analysis, *J. Chemom.* 20 (2006) 221–229. doi:10.1002/cem.994.
- [33] E. Marengo, M. Manfredi, O. Zerbinati, E. Robotti, E. Mazzucco, F. Gosetti, G. Bearman, F. France, P. Shor, Technique Based on LED Multispectral Imaging and Multivariate Analysis for Monitoring the Conservation State of the Dead Sea Scrolls, *Anal. Chem.* 83

- (2011) 6609–6618. doi:10.1021/ac201068s.
- [34] M. Vidal, J.M. Amigo, Pre-processing of hyperspectral images. Essential steps before image analysis, *Chemom. Intell. Lab. Syst.* 117 (2012) 138–148. doi:10.1016/J.CHEMOLAB.2012.05.009.
- [35] W.F. de Carvalho Rocha, G.P. Sabin, P.H. Março, R.J. Poppi, Quantitative analysis of piroxicam polymorphs pharmaceutical mixtures by hyperspectral imaging and chemometrics, *Chemom. Intell. Lab. Syst.* 106 (2011) 198–204.
- [36] C. Suh, A. Rajagopalan, X. Li, K. Rajan, The application of Principal Component Analysis to materials science data, *Data Sci. J.* 1 (2002) 19–26. doi:10.2481/dsj.1.19.
- [37] H. Kargupta, W. Huang, K. Sivakumar, B.-H. Park, S. Wang, Collective Principal Component Analysis from Distributed, Heterogeneous Data, in: Springer, Berlin, Heidelberg, 2000: pp. 452–457. doi:10.1007/3-540-45372-5_50.
- [38] P. Geladi, H. Grahn, *Multivariate image analysis*, Wiley, 1996.
- [39] D.S. Crosby, L.C. Breaker, W.H. Gemmill, A Proposed Definition for Vector Correlation in Geophysics: Theory and Application, *J. Atmos. Ocean. Technol.* 10 (1993) 355–367. doi:10.1175/1520-0426(1993)010<0355:APDFVC>2.0.CO;2.
- [40] C. Cheng, M.-S. Chiu, A new data-based methodology for nonlinear process modeling, *Chem. Eng. Sci.* 59 (2004) 2801–2810. doi:10.1016/J.CES.2004.04.020.
- [41] C.E. Anderson, J.H. Kalivas, Fundamentals of Calibration Transfer through Procrustes Analysis, *Appl. Spectrosc. Vol. 53, Issue 10, Pp. 1268-1276.* 53 (1999) 1268–1276.
- [42] D. Jouan-Rimbaud, D.L. Massart, C.A. Saby, C. Puel, Characterisation of the representativity of selected sets of samples in multivariate calibration and pattern recognition, *Anal. Chim. Acta.* 350 (1997) 149–161.
- [43] D. Jouan-Rimbaud, D.L. Massart, C.A. Saby, C. Puel, Determination of the representativity between two multidimensional data sets by a comparison of their structure, *Chemom. Intell. Lab. Syst.* 40 (1998) 129–144.
- [44] D.L. Hall, J. Llinas, An introduction to multisensor data fusion, *Proc. IEEE.* 85 (1997) 6–23. doi:10.1109/5.554205.
- [45] E. Borràs, J. Ferré, R. Boqué, M. Mestres, L. Aceña, O. Busto, Data fusion methodologies for food and beverage authentication and quality assessment – A review, *Anal. Chim. Acta.* 891 (2015) 1–14. doi:10.1016/J.ACA.2015.04.042.
- [46] A.J. Tencate, J.H. Kalivas, A.J. White, Fusion strategies for selecting multiple tuning parameters for multivariate calibration and other penalty based processes: A model updating application for pharmaceutical analysis, *Anal. Chim. Acta.* 921 (2016) 28–37. doi:10.1016/J.ACA.2016.03.046.
- [47] M.R. Anderberg, *Cluster analysis for applications: probability and mathematical statistics: a series of monographs and textbooks*, Academic press, 2014.
- [48] L. Wald, Some terms of reference in data fusion, *IEEE Trans. Geosci. Remote Sens.* 37

- (1999) 1190–1193.
- [49] H.B. Mitchell, *Data fusion: concepts and ideas*, Springer Science & Business Media, 2012.
- [50] B. V Dasarathy, A representative bibliography of surveys in the information fusion domain, *Inf. Fusion*. 11 (2010) 299–300.
- [51] M. Nixon, A. Aguado, *Feature extraction & image processing for computer vision*, 2012.
- [52] A. Khotanzad, Y.H. Hong, Invariant image recognition by Zernike moments, *IEEE Trans. Pattern Anal. Mach. Intell.* 12 (1990) 489–497. doi:10.1109/34.55109.
- [53] C. Singh, P. Sharma, Performance analysis of various local and global shape descriptors for image retrieval, *Multimed. Syst.* 19 (2013) 339–357. doi:10.1007/s00530-012-0288-7.
- [54] M.R. Teague, Image analysis via the general theory of moments*, *J. Opt. Soc. Am.* 70 (1980) 920. doi:10.1364/JOSA.70.000920.
- [55] C. Singh, E. Walia, R. Upneja, Accurate calculation of Zernike moments, *Inf. Sci. (Ny)*. 233 (2013) 255–275. doi:10.1016/J.INS.2013.01.012.
- [56] C. Wolf, G. Taylor, J. Jolion, B. Verne, A. Einstein, Learning individual human activities from short binary shape sequences, (2011).
- [57] A. Tahmasbi, F. Saki, S.B. Shokouhi, Classification of benign and malignant masses based on Zernike moments, *Comput. Biol. Med.* 41 (2011) 726–735. doi:10.1016/J.COMPBIOMED.2011.06.009.
- [58] C.-H. Teh, R.T. Chin, On image analysis by the methods of moments, *IEEE Trans. Pattern Anal. Mach. Intell.* 10 (1988) 496–513. doi:10.1109/34.3913.
- [59] G. Kumar, P.K. Bhatia, A detailed review of feature extraction in image processing systems, in: *Adv. Comput. Commun. Technol. (ACCT)*, 2014 Fourth Int. Conf., IEEE, 2014: pp. 5–12.
- [60] F. Ghorbel, S. Derrode, R. Mezhoud, T. Bannour, S. Dhahbi, Image reconstruction from a complete set of similarity invariants extracted from complex moments, *Pattern Recognit. Lett.* 27 (2006) 1361–1369.
- [61] A.-W. Deng, C.-H. Wei, C.-Y. Gwo, Stable, fast computation of high-order Zernike moments using a recursive method, *Pattern Recognit.* 56 (2016) 16–25.
- [62] H. Zhang, Z. Dong, H. Shu, Object recognition by a complete set of pseudo-Zernike moment invariants, in: *Acoust. Speech Signal Process. (ICASSP)*, 2010 IEEE Int. Conf., IEEE, 2010: pp. 930–933.
- [63] Y.-H. Pang, A.B.J. Teoh, D.C.L. Ngo, A discriminant pseudo Zernike moments in face recognition, *J. Res. Pract. Inf. Technol.* 38 (2006) 197.
- [64] A.B. Bhatia, E. Wolf, *On the circle polynomials of Zernike and related orthogonal sets*, in: *Math. Proc. Cambridge Philos. Soc.*, Cambridge University Press, 1954: pp. 40–48.

- [65] O. Ryabchykov, A. Ramoji, T. Bocklitz, M. Foerster, S. Hagel, C. Kroegel, M. Bauer, U. Neugebauer, J. Popp, Leukocyte subtypes classification by means of image processing, in: *Comput. Sci. Inf. Syst. (FedCSIS), 2016 Fed. Conf., IEEE, 2016*: pp. 309–316.
- [66] D. Han, H. Du, S. Jassim, *Towards a Confidence-Centric Classification Based on Gaussian Models and Bayesian Principles*, (n.d.).
- [67] V. Vovk, A. Gammernan, G. Shafer, *Algorithmic learning in a random world*, Springer Science & Business Media, 2005.
- [68] C. Eliades, H. Papadopoulos, *Conformal Prediction for Automatic Face Recognition*, in: *Conform. Probabilistic Predict. Appl.*, 2017: pp. 62–81.
- [69] N. Petraco, H. Chan, *Application of machine learning to toolmarks: statistically based methods for impression pattern comparisons*, Bibliographisches Institut AG, 2012.
- [70] M. Capuccini, L. Carlsson, U. Norinder, O. Spjuth, *Conformal prediction in spark: Large-scale machine learning with confidence*, in: *Big Data Comput. (BDC), 2015 IEEE/ACM 2nd Int. Symp.*, IEEE, 2015: pp. 61–67.
- [71] E.D. Jones, *Forensic Investigation of Stamped Markings Using a Large-Chamber Scanning Electron Microscope and Computer Analysis for Depth Determination*, (2013).
- [72] *Metal properties*, (n.d.).
https://depts.washington.edu/matseed/mse_resources/Webpage/Metals/metalproperty.htm
 (accessed November 9, 2018).
- [73] H. Katterwe, *Restoration of serial numbers*, in: *Forensic Investig. Stolen-Recovered Other Crime-Related Veh.*, Elsevier, 2006: pp. 177–205. doi:10.1016/B978-012088486-5/50041-7.
- [74] D.M. Turley, *Restoration of stamp marks on steel components by etching and magnetic techniques*, *J. Forensic Sci.* 32 (1987) 640–649.
- [75] M.R. Derrick, D. Stulik, J.M. Landry, *Infrared spectroscopy in conservation science*, Getty Publications, 2000.
- [76] L. Dobrovolny, *Current Trends in Spectral Reflectance Imaging Techniques: A Qualitative Approach to the Investigation and Documentation of Building Materials*, (2015).
- [77] R. Usamentiaga, P. Venegas, J. Guerediaga, L. Vega, J. Molleda, F. Bulnes, R. Usamentiaga, P. Venegas, J. Guerediaga, L. Vega, J. Molleda, F.G. Bulnes, *Infrared Thermography for Temperature Measurement and Non-Destructive Testing*, *Sensors*. 14 (2014) 12305–12348. doi:10.3390/s140712305.
- [78] J.W.M. Spicer, R. Osiander, *Time-dependent temperature distributions for nondestructive probing of material properties*, *Johns Hopkins APL Tech. Dig.* 16 (1995) 278–287.
- [79] C. Ibarra-Castanedo, M. Genest, S. Guibert, J.-M. Piau, X.P. V Maldague, A. Bendada, *Inspection of aerospace materials by pulsed thermography, lock-in thermography, and vibrothermography: a comparative study*, in: *Thermosense XXIX*, International Society

- for Optics and Photonics, 2007: p. 654116.
- [80] C. Meola, G.M. Carlomagno, L. Giorleo, Geometrical limitations to detection of defects in composites by means of infrared thermography, *J. Nondestruct. Eval.* 23 (2004) 125–132.
- [81] O. Breitenstein, J.P. Rakotoniaina, F. Altmann, T. Riediger, M. Gradhand, New developments in IR lock-in thermography, in: *Proc. 30th ISTFA, 2004*: pp. 595–599.
- [82] R. Montanini, A. Quattrocchi, S.A. Piccolo, Active thermography and post-processing image enhancement for recovering of abraded and paint-covered alphanumeric identification marks, *Infrared Phys. Technol.* 78 (2016) 24–30.
- [83] C. Ibarra-Castanedo, N.P. Avdelidis, M. Grenier, X. Maldague, A. Bendada, Active thermography signal processing techniques for defect detection and characterization on composite materials, in: *Thermosense XXXII, International Society for Optics and Photonics, 2010*: p. 76610O.
- [84] F. López, C. Ibarra-Castanedo, V.P. Nicolau, X. Maldague, Comparative study of Thermographic signal reconstruction and partial least-squares thermography for detection and evaluation of subsurface defects, in: *12th Int. Conf. Quant. Infrared Thermogr. Bordeaux, Fr., 2014*.
- [85] D.L. Balageas, J.-M. Roche, F.-H. Leroy, W.-M. Liu, A.M. Gorbach, The thermographic signal reconstruction method: A powerful tool for the enhancement of transient thermographic images, *Biocybern. Biomed. Eng.* 35 (2015) 1–9.
- [86] I.T. Jolliffe, A note on the use of principal components in regression, *Appl. Stat.* (1982) 300–303.
- [87] A. Sophian, G.Y. Tian, D. Taylor, J. Rudlin, A feature extraction technique based on principal component analysis for pulsed eddy current NDT, *NDT e Int.* 36 (2003) 37–41.
- [88] S. Marinetti, E. Grinzato, P.G. Bison, E. Bozzi, M. Chimenti, G. Pieri, O. Salvetti, Statistical analysis of IR thermographic sequences by PCA, *Infrared Phys. Technol.* 46 (2004) 85–91. doi:10.1016/J.INFRARED.2004.03.012.
- [89] L. Cheng, B. Gao, G.Y. Tian, W.L. Woo, G. Berthiau, Impact damage detection and identification using eddy current pulsed thermography through integration of PCA and ICA, *IEEE Sens. J.* 14 (2014) 1655–1663.
- [90] C. Qing, Evaluation of OCR Algorithms for Images with Different Spatial Resolution and Noise, 2003.
- [91] Precision Forensic Testing, Stamped Serial Number Restoration Metal – Precision Forensic Testing, (n.d.). <https://www.precisionforensictesting.com/collections/crime-laboratory-products/products/stamped-serial-number-restoration-metal> (accessed June 20, 2018).
- [92] O. Raghu, J. Philip, Thermal properties of paint coatings on different backings using a scanning photo acoustic technique, *Meas. Sci. Technol.* 17 (2006) 2945.
- [93] Å. Rinnan, F. van den Berg, S.B. Engelsen, Review of the most common pre-processing

techniques for near-infrared spectra, *TrAC Trends Anal. Chem.* 28 (2009) 1201–1222.

Appendix I: Score Images of Defaced Numbers

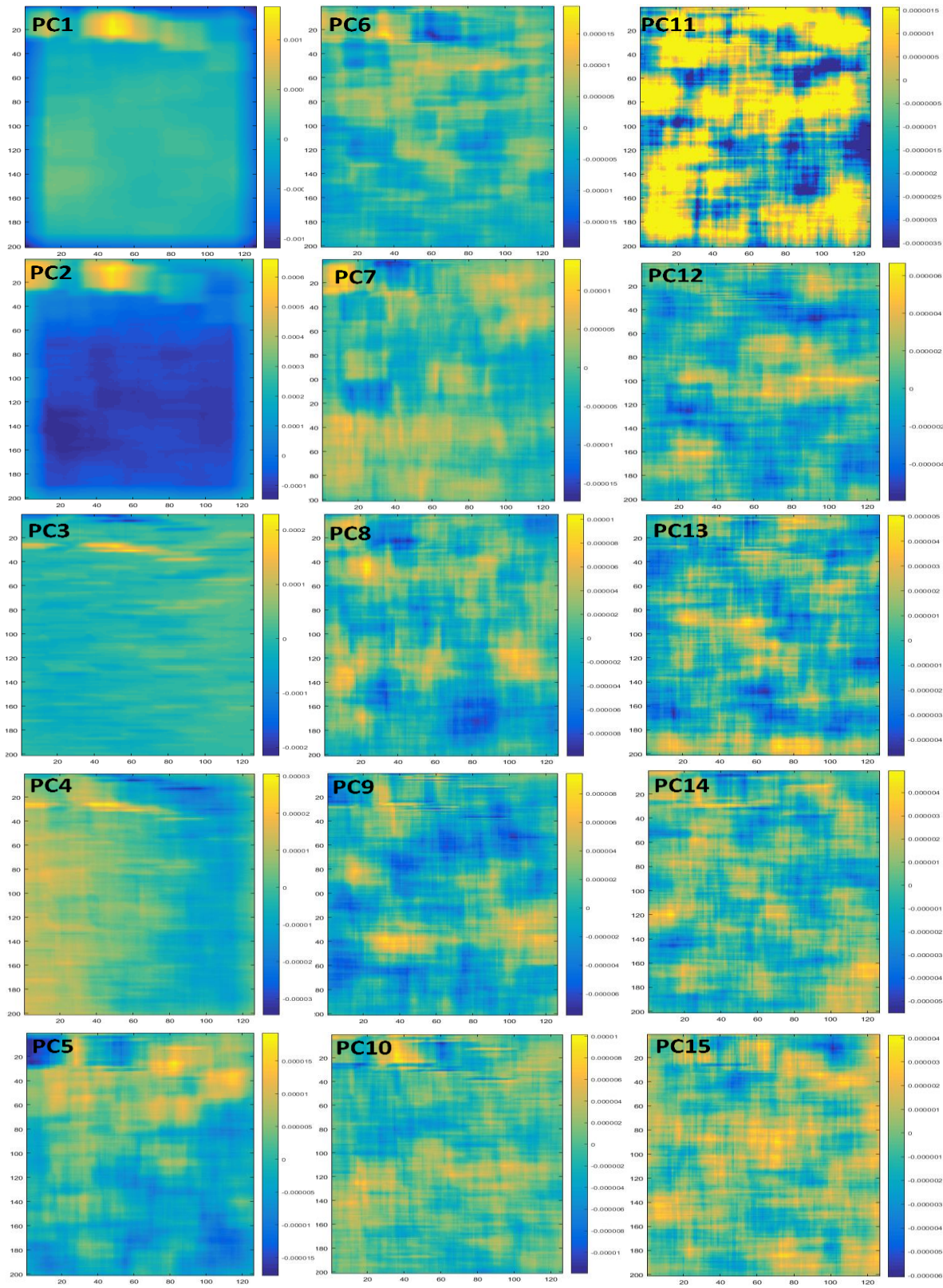


Figure A1: Refolded PC score images of the area around the defaced number 2 with PC 11 showing the best representation of the number

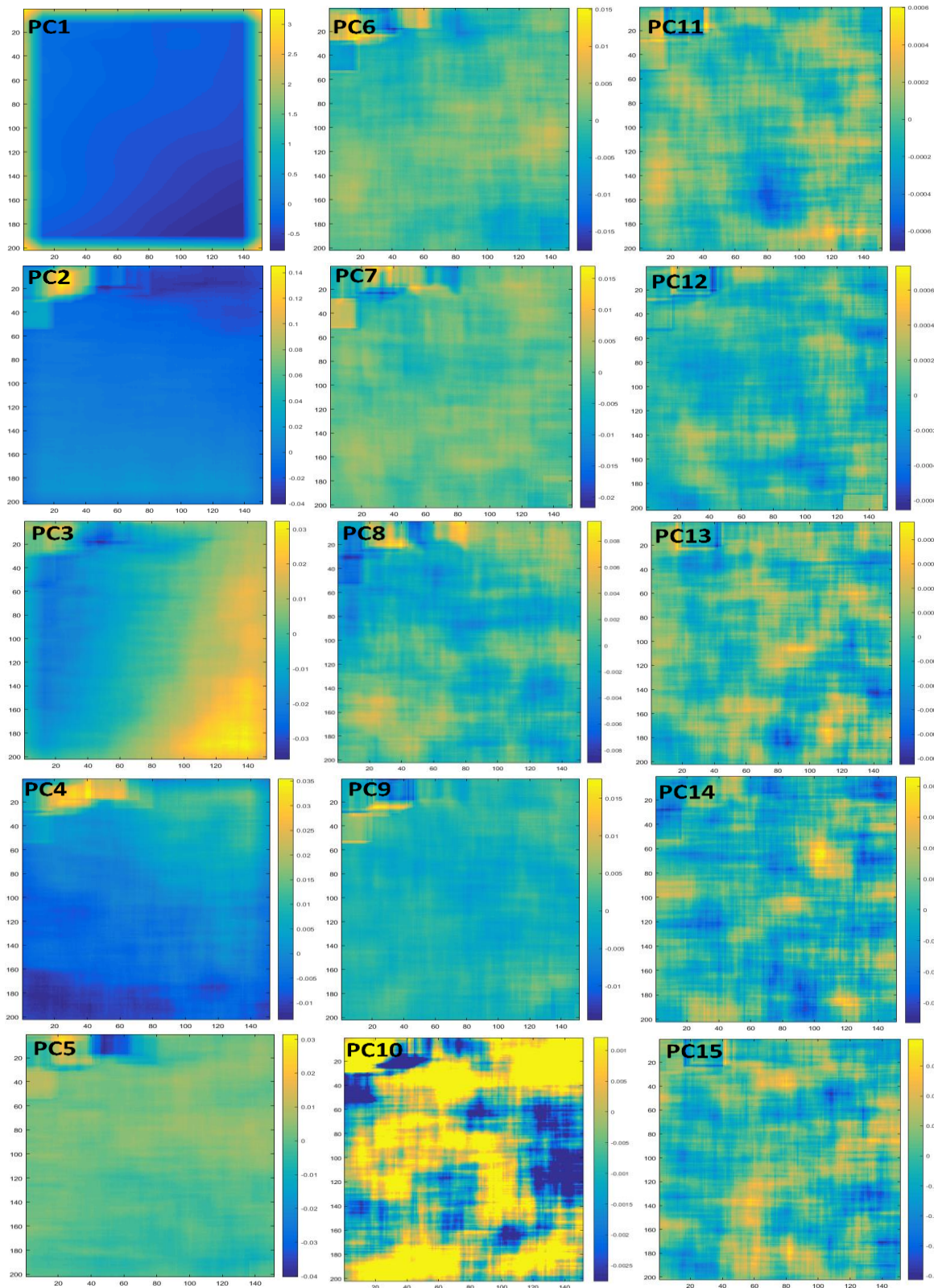


Figure A2: Refolded PC score images of the area around the defaced number 5 with PC 10 showing the best representation of the number

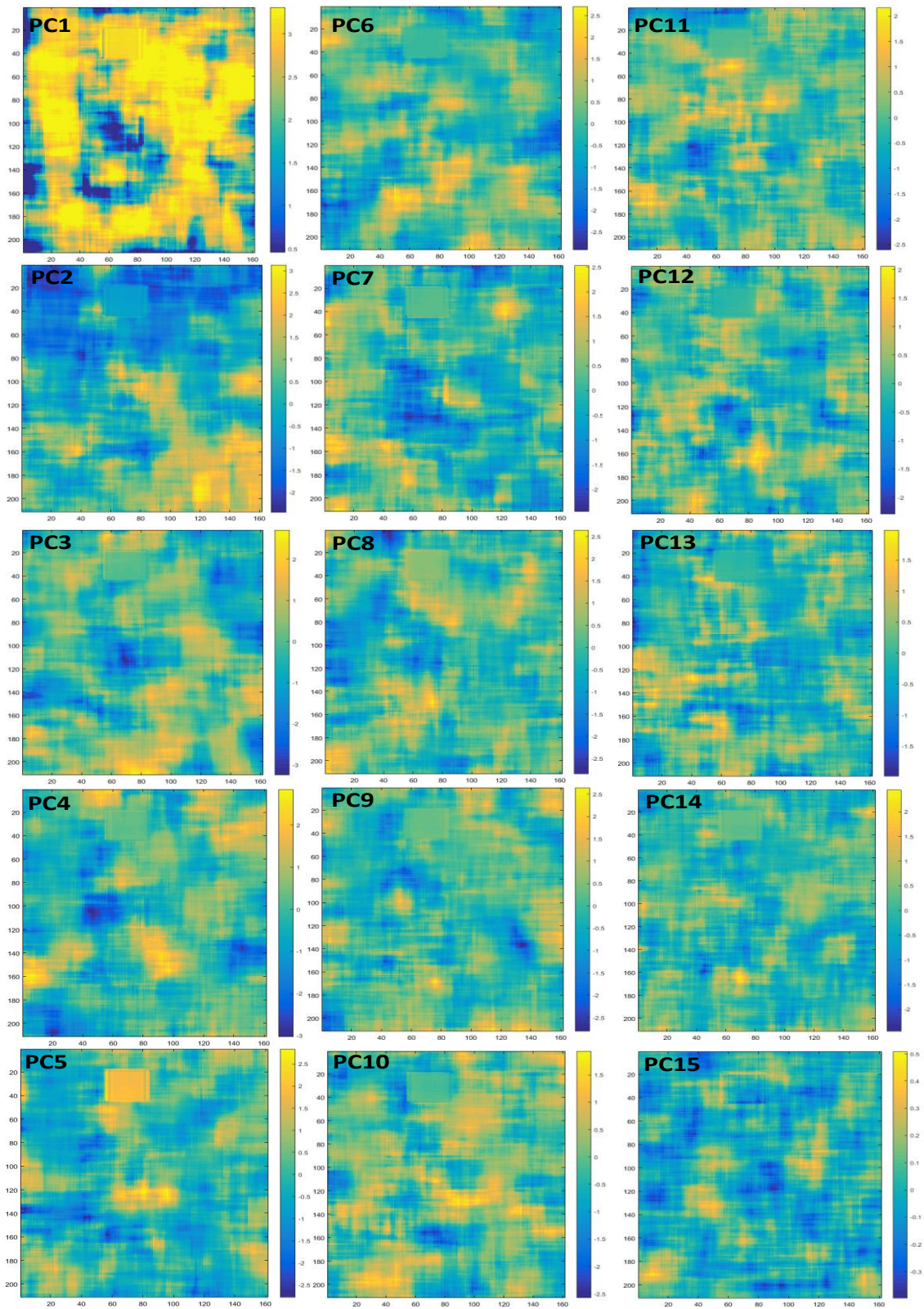


Figure A3: Refolded PC score images of the area around the defaced number 0 with PC 1 showing the best representation of the number.

Appendix II: Equipment Used

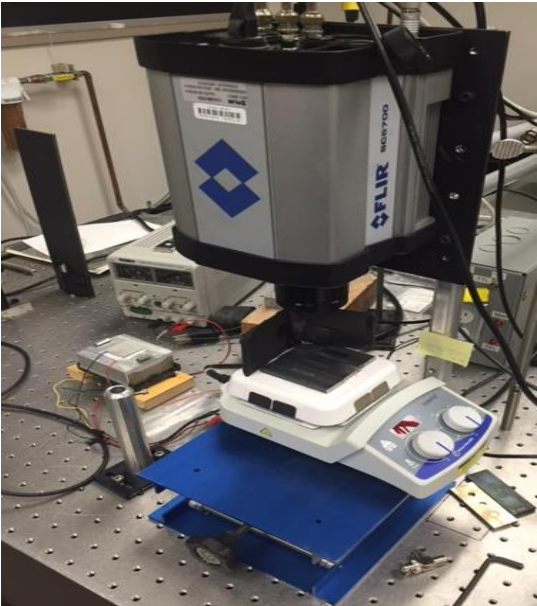


Figure A4: FLIR SC6700 infrared camera with sample on a hot plate under observation.



Figure A5: Oscilloscope.

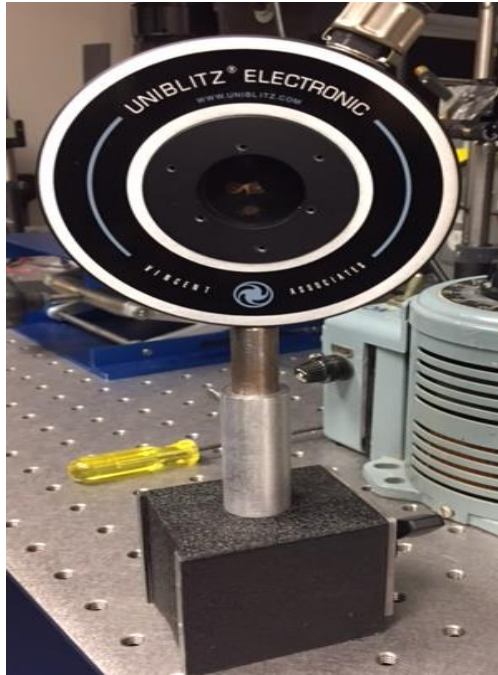
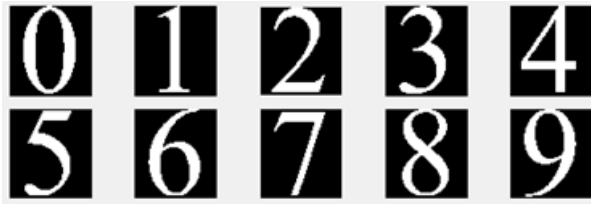


Figure A6: Uniblitz mechanical shutter.

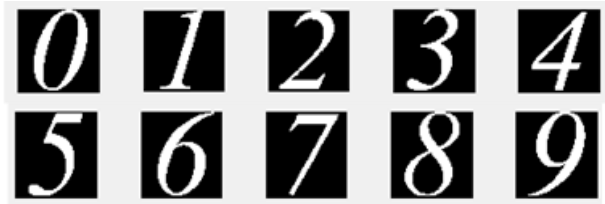


Figure A7: Mechanical shutter control box (top) and Stanford Research Systems function generator (bottom).

Appendix III: Images of Reference Libraries used



Times New Roman



Times New Roman Italics



Tempus Sans



Segoe Print



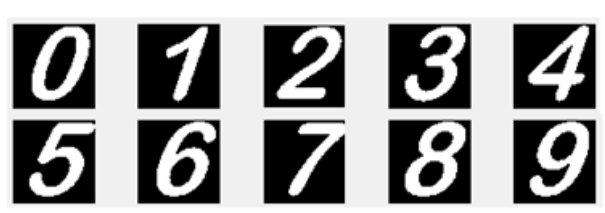
Gung Suh



Gung Suh Italics



Arial Rounded MT



Arial Rounded MT Italics



Arial Black



Arial Black Italics

Figure A8: Images of digits used from different fonts.

Appendix IV: Study of variation in thermal gradient

A study of the variation in degree of phase shift within the zone of plastic compared to the shift in clean non-stamped areas was carried out to try to determine if PCA is leveraging on variations in thermal gradient within the regions of plastic strain to reimage the defaced numbers into a single score image.

The difference in the standard deviation of pixels in the defaced regions for the defaced number 6 and those in clean non stamped regions was computed for each amplitude image and plotted. The difference between these two values was used as representative of the variability of thermal gradient in a single image. Figure A9 shows the pixels used to represent both defaced and clean areas. The plot of this standard deviation difference across all 15 amplitude images is shown in Figure A10. It can be expected that the deformed areas will show larger variability in thermal gradient compared to the background due to a lack of uniformity in the crystalline structure. Background or clean non-stamped areas on the other hand should have a uniform thermal gradient and consequently lower standard deviation. Thus, the magnitude of the difference in the standard deviations of both areas in an image could help determine which cycles better capture the thermal gradient differences, and as such will be important in PCA picking up the variability to reimage the number into a single score image.

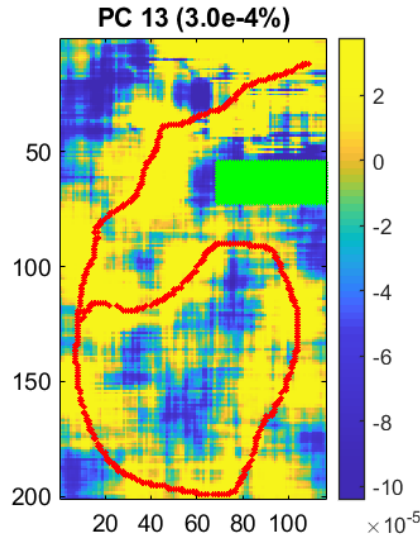


Figure A9: Score image reproducing defaced 6 with selected pixels marked.

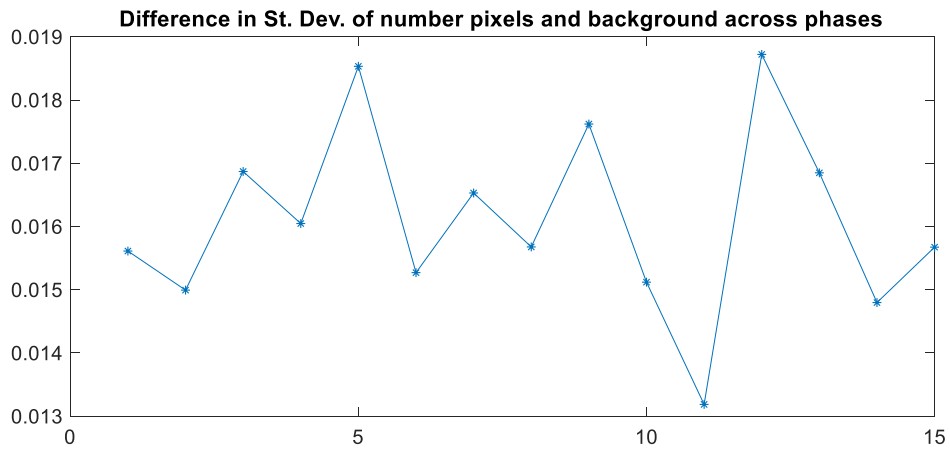


Figure A10: Plot of difference in standard deviation between defaced areas and clean areas across 15 amplitude images.

Figure A11a shows a score image developed using all the amplitude images developed from the 15 testing cycles. Figure A11b shows a score image developed from amplitude images minus the amplitude image with the lowest standard deviation difference i.e. amplitude image 11 and Figure A11c shows a score image after removing the 5 amplitude images with the lowest standard deviation difference from the plot in Figure A10. From these images, it can be determined that there is a continuous drop in the quality of the score image that was visually

selected as most representative of the defaced number. Removing score images with higher standard deviation, the number can no longer be visually recognized in a score image.

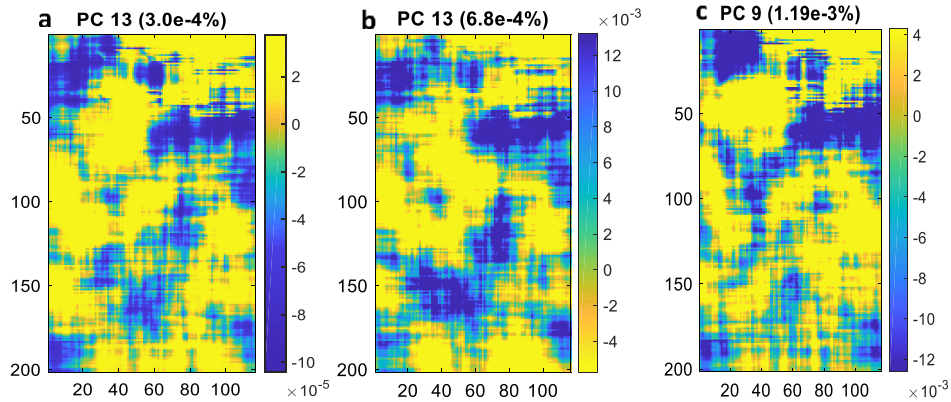


Figure A11: Score images reproducing defaced numbers using a) all amplitude images, b) amplitude image with lowest standard deviation removed and c) amplitude images with 5 lowest standard deviations removed.

A similar analysis was carried out for the other defaced numbers. Figure A12 shows the score image visually determined to best reimagine the defaced number 2. The markers on the image indicate the pixels selected to represent defaced areas and clean areas respectively.

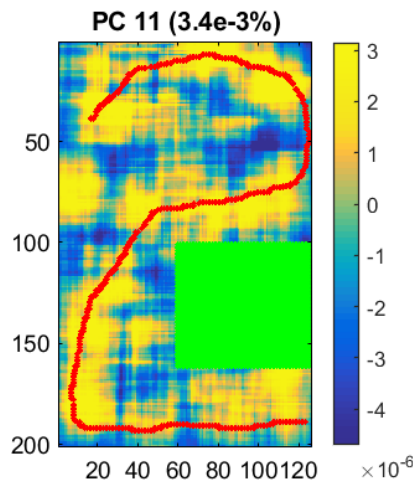


Figure A12: Score image reproducing defaced 2 with selected pixels marked.

Figure A13 shows a plot of the difference in standard deviation between the defaced and clean areas across all 15 amplitude image used in PCA to reproduce the defaced number.

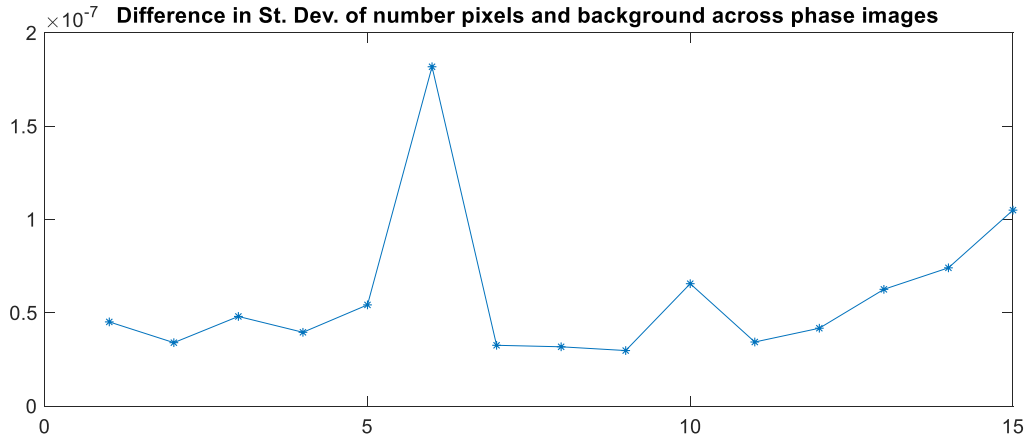


Figure A13: Plot of difference in standard deviation between defaced areas and clean areas across 15 amplitude images.

The amplitude images with the lowest standard deviation differences were progressively removed and PCA carried out to determine the value of those images to the reproduction of the defaced number. Figures A14a to A14c show the results from this analysis. Figure A14a shows the score image resulting from using all the amplitude image. This score image was visually selected as best reproducing the defaced number. Figure A14b shows a score image developed by carrying out PCA on a dataset of the amplitude images without the amplitude image with the lowest standard deviation difference selected from the plot in Figure A13. This score image shows a slight drop in the quality of reproducing the defaced number. Figure A14c shows a score image developed from a dataset of the amplitude images after removing the 3 amplitude images with the lowest standard deviations. This figure shows a considerable drop in quality of the reproduced image. Score images from carrying out PCA on datasets without amplitude images with higher standard deviations failed to reproduce the defaced number to allow for visual recognition.

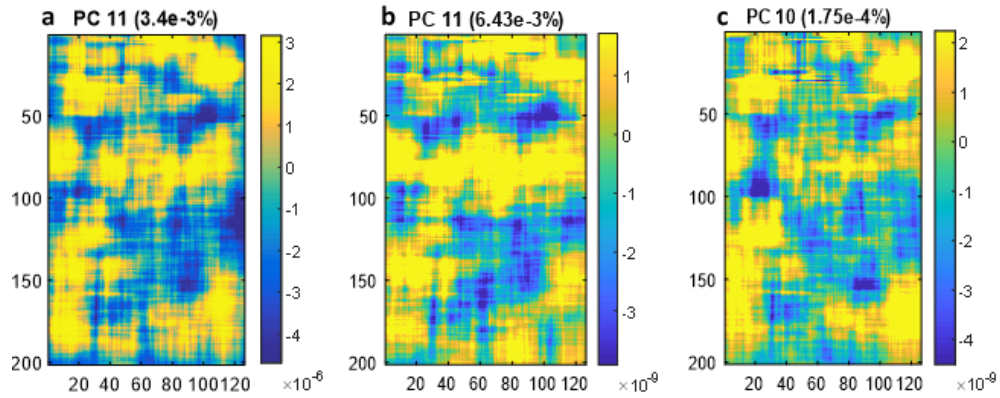


Figure A14: Score images reproducing defaced numbers using a) all amplitude images, b) amplitude image with lowest standard deviation removed and c) amplitude images with 5 lowest standard deviations removed.

Figure A15 shows the score image visually selected as best reproducing the defaced number 5 after carrying out PCA on the dataset of phase images of all 15 testing cycles. The markers on the image indicate the pixels selected to represent defaced region and clean non-stamped regions respectively.

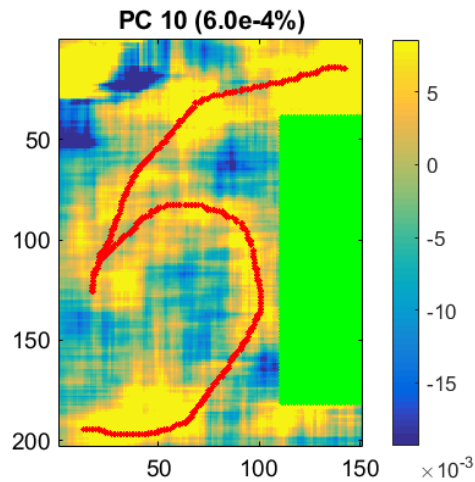


Figure A15: Score image reproducing defaced 5 with selected pixels marked.

Figure A16 shows a plot of the difference in standard deviation between the defaced and clean areas across all 15 amplitude image used in PCA to reproduce the defaced number.

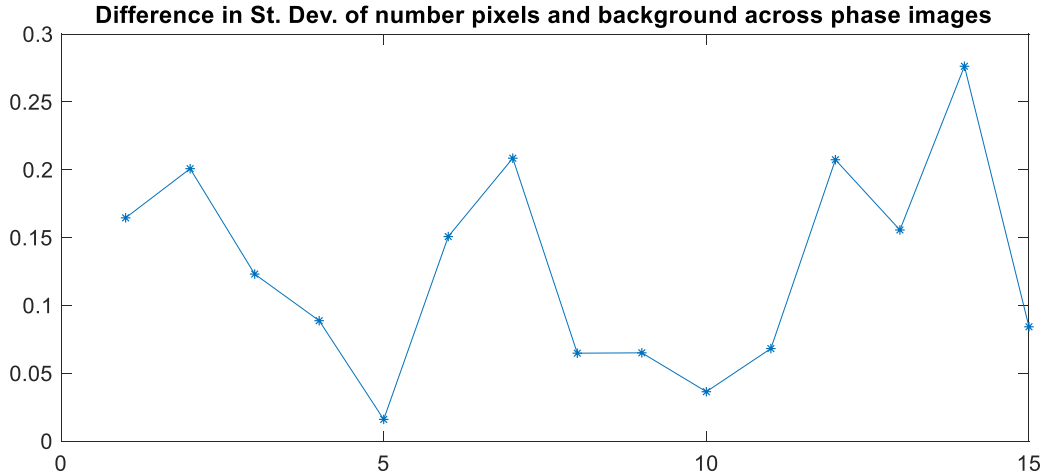


Figure A16: Plot of difference in standard deviation between defaced areas and clean areas across 15 phase images.

Similar to the defaced areas previously analyzed, the phase images with the lowest standard deviation differences were selected from the plot in Figure 8 and progressively removed from the dataset used as the input matrix for PCA. Figure A17 shows the results of this analysis. Figure A17a shows a score image developed using all 15 phase images. This score image was selected visually to have best reproduced the defaced number 5. Figure A17b shows a score image developed from an input matrix of phase images without the phase image with the lowest standard deviation difference (phase image 5 from Figure A16). This image shows a slight drop in quality of the reproduced number and the number could still possibly be visually recognized in the score image. Figure A17c shows a score image developed from an input matrix of phase images after removing the 3 phase images with the lowest standard deviation differences. This score image shows a considerable drop in quality from the previous, reducing the possibility of visually identifying the number. Carrying out PCA on input matrices without phase images with higher standard deviation differences failed to develop any single score image where the number could be visually recognized.

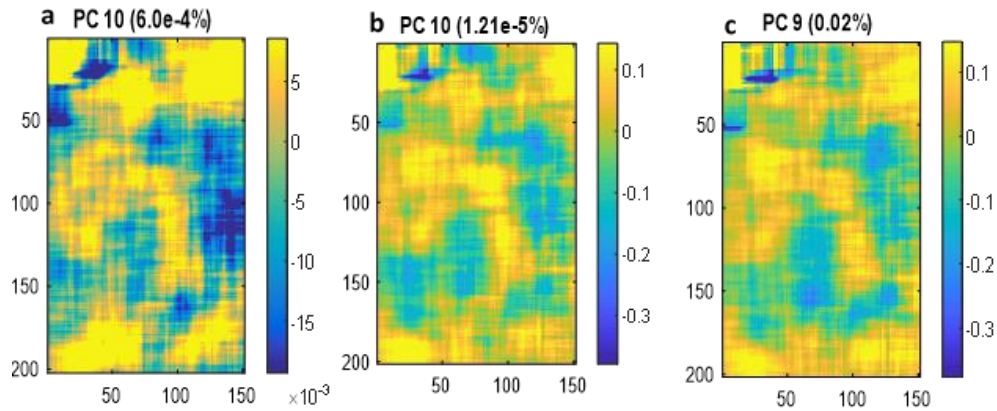


Figure A17: Score images reproducing defaced numbers using a) all phase images, b) phase image with lowest standard deviation removed and c) phase images with 5 lowest standard deviations removed.

Figure A18 shows the score image that best reproduced the defaced number 0 with the pixels selected for analysis marked. As with the previously analyzed defaced areas, the selected pixels were used as representative of the defaced and clean non-stamped areas.

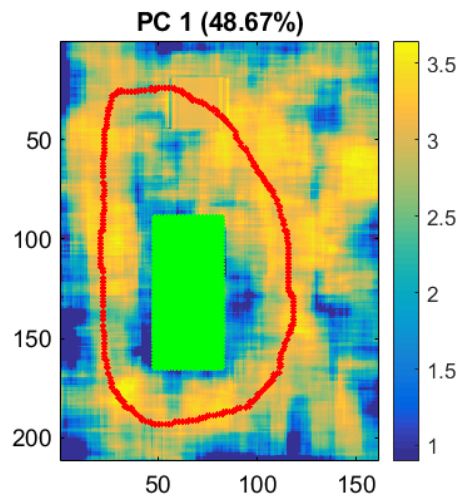


Figure A18: Score image reproducing defaced 0 with selected pixels marked.

Figure A19 shows the difference in standard deviation of defaced areas and clean areas for each of the 15 amplitude images developed from the testing cycles. As with the other analyzed areas, there are fluctuations in the standard deviation differences and these were used to determine

which amplitude images were more important for use in reproducing the defaced number into a single score image in PCA.

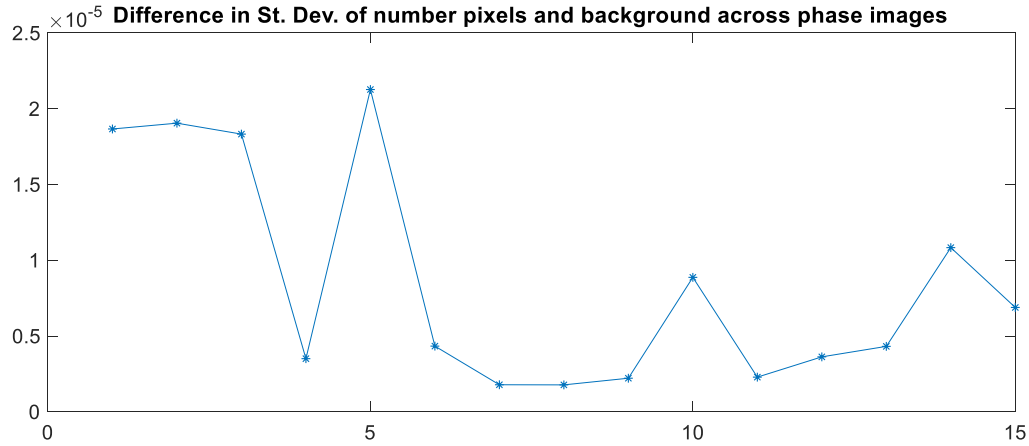


Figure A19: Plot of difference in standard deviation between defaced areas and clean areas across 15 amplitude images.

Similar to the defaced areas previously analyzed, the amplitude images with the lowest standard deviation differences were selected from the plot in Figure A19 and progressively removed from the dataset used as the input matrix for PCA. Figure A20 shows the results of this analysis. Figure A20a shows the score image that best captured the variation in thermal gradient to reproduce the defaced number. This is compared to Figure A20b which shows a score image developed from the amplitude images without the image with the lowest standard deviation. It can be seen that there is little change in the quality of the image reproducing the defaced 0. Figure A20c shows a score image developed using an input matrix without the 11 amplitude images with the lowest standard deviations. This image shows a marked degradation in quality reducing the prospect of visually identifying the defaced number.

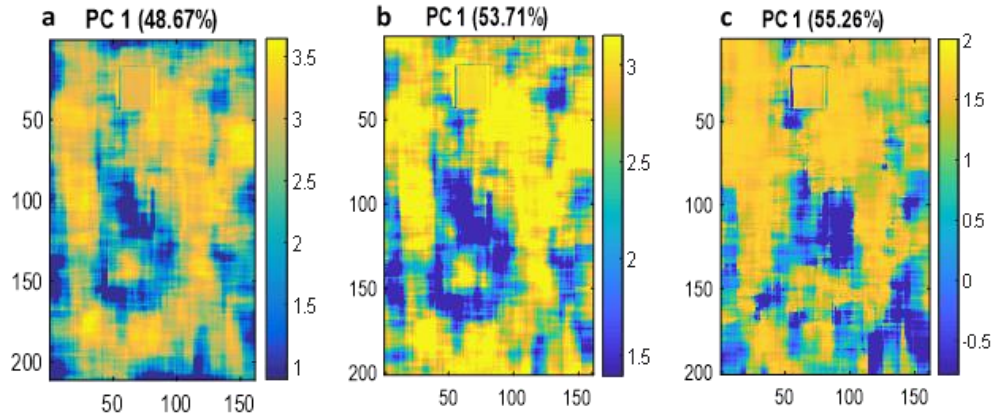


Figure A20: Figure 6: Score images reproducing defaced numbers using a) all amplitude images, b) amplitude image with lowest standard deviation removed and c) amplitude images with 5 lowest standard deviations removed.

From this analysis, it can be determined that PCA is capturing the variability in the thermal gradient within the zone of plastic strain and leveraging on this variation to reimage the defaced number into a single score image. This study also seems to indicate that with more material removed, leading to a smaller zone of plastic strain, more cycles are needed to help PCA localize the variation in the zone of plastic strain and capture the number into a single score image to allow for visually recognizing the number. The number of cycles needed to reproduce the defaced 0 is much smaller the others because the number was initially stamped deeper, and as such has a more extended zone of plastic strain.